KU Leuven
Biomedical Sciences Group
Faculty of Medicine
Department of Imaging & Pathology

GOLD NANOSTARS AS A SPECIFIC THERANOSTIC AGENT AGAINST HER2-EXPRESSING TUMOR CELLS

ANTOINE D'HOLLANDER

Promoter:	Prof. Dr. Uwe Himmelreich
Co-Promoters:	Prof. Dr. Liesbet Lagae
	Prof. Dr. Serge Muyldermans
Chair:	Prof. Dr. Vincent Vandecaveye
Secretary:	Prof. Dr. Pol Van Dorpe
Assessors:	Prof. Dr. Marleen Keyaerts
	Prof Dr. Kristien Bonroy

Dissertation presented in partial fulfillment of the requirements for the degree of Doctor in Biomedical Sciences

November - 2016

ABSTRACT

Annually more than 3.45 million new cases of cancer are registered in Europe which makes cancer one of the most deadly diseases. Current strategies to diagnose, image and treat cancer still lack efficiency, is invasiveness and are provoking uncomfortable side-effects for the patient. While still in an early stage of development, gold nanoparticle-based diagnostics and therapeutics could potentially alleviate these shortcomings. The wide-based interest for these gold nanoparticles originates from their unique optical and thermal properties appearing at a nanometer scale. These properties form basis for their use as an imaging (e.g. photoacoustic imaging) and therapeutic (e.g. photothermal therapy) agent. As a consequence these gold nanoparticles can be used as a theranostic agent combining both their imaging and therapeutic capabilities into one nanoparticle. In this PhD work we used gold nanostars as a theranostic agent for HER2 expressing tumor masses, since they have stronger optical properties compared to other anisotropic gold nanoparticles. To be used in clinical conditions, these nanostars have to meet critical requirements including the absorption of light in the NIR-region, a hydrodynamic diameter below 100 nm and to be highly stable under physiological conditions. Optimizing the existing synthesis and functionalization procedure resulted in the desiring nanostars. *In vitro* and *in vivo* experiments (by intratumoral injection) confirmed their theranostic properties while they end up in vesicular structures in the tumor cells. However the final goal is to target these tumor masses by the nanostars after intravenous injection. Two targeting strategies are explored, either passively where the nanostars diffuse into the tumor interstitium or actively where the nanostars are functionalized with a biological molecule, which recognizes an overexpressed receptor on the tumor cells. While passive targeting showed an effective nanostar uptake in the tumor cells *in vitro*, by changing the end-group of the self-assembled monolayer on the nanostar surface, *in vivo* the nanostars did not accumulate at the tumor masses. Active targeting could increase this uptake where the nanostars were functionalized with a nanobody targeting the HER2 receptors on the tumor cells. Specific uptake of the nanobody functionalized nanostars in the tumor cells was realized *in vitro* and *in vivo* after blocking the protein corona formation by deactivating the chemically active groups on the nanostar's surface.

Developing gold nanostars as a theranostic agent for cancer is a multidisciplinary research task where chemistry, biology and nanotechnology encounters. This study contributed to important improvements on both studying the theranostic properties of the nanostars as well as on optimizing the targeting strategies of the nanostars to tumor masses.

SAMENVATTING

Jaarlijks is kanker nog altijd één van de belangrijkste doodoorzaken in Europa waarbij nog steeds 3.45 miljoen nieuwe kanker patiënten geregistreerd worden. Huidige kanker diagnose-, beelvormings- en therapiestrategiën missen nog altijd efficientie en zijn invasief waardoor het veel neveneffecten heeft voor de patient. Ondanks dat het onderzoek rond gouden nanopartikels in een startende fase zit, zouden deze nanoparticles deze noden kunnen voldoen door hun unieke optische en thermische eigenschappen. Deze eigenschappen zijn de basis voor hun beeldvormings (bv: fotoakoestische beeldvorming) en therapeutische (bv: fotothermale) capaciteiten. Bijgevolg kunnen ze zelf gebruikt worden als een theranostische agentia waarbij hun beeldvorming en therapeutische capaciteiten gecombineerd worden.

In deze doctoraatsthesis hebben we gouden nanosterren gebruikt als een theranostische agentia voor HER2 expressie brengende tumorcellen. Deze nanosterren zijn gekozen door hun sterkere optische eigenschappen in vergelijk met andere anistrope nanosterren. Voor ze gebruikt kunnen worden in klinische condities moeten deze nanosterren voldoen aan een paar voorwaarden zoals het licht absorberen in het NIR gebied, een hydrodynamische diameter hebben onder 100 nm en stabiel zijn in fysiologische condities. Dit werd gerealiseerd door bestaande synthese en functionalisatie processen te optimaliseren. Met behulp van *in vitro* en *in vivo* experimenten (intratumorale injectie) werd hun theranostische eigenschappen bevestigd waarbij de opname van de nanosterren in vesiculaire structuren van de tumor cel werd gevisualiseerd. Voor de finale toepassing, moeten de nanosterren specifiek opstalen in de tumor massa's na intraveneuze toediening. Hiervoor zijn er twee strategiën beschreven, zowel de passieve targeting waarbij de nanosterren diffuseren in het tumor interstitium, of de actieve targeting waarbij de nanosterren gefuntionaliseerd worden met een biologisch molecule dat een kankerspecifiek ligand herkent op de tumorcellen. Ondanks dat voor de nanosterren een effectieve opname in de tumor cellen is waargenomen *in vitro*, afhankelijk van de eindgroep op de chemische stabiliserende laag, kon deze resultaten *in vivo* niet geraliseerd worden. Actieve targeting van de HER2 receptors zou deze nanoster opname in de tumorcellen kunnen verhoren met behulp van nanobodies. Specifieke opname van deze biologisch gefunctionaliseerde nanosterren werd *in vitro* and *in vivo* gerealiseerd na het deactiveren van de actieve groepen op de oppervlakte van de nanosterren waardoor de protein corona diameter geminimaliseerd werd rond de nanosterren.

Het gebruik van nanosterren als een theranostische agentia voor cancer is een multidisciplinair onderzoek op de grens van chemie, biologie en nanotechnologie. Deze studie heeft bijgedragen

op het vlak van de theranostische eigenschappen als ook op de geoptimaliseerde targeting strategie van de nanosterren in tumor massa's.

ACKNOWLEDGEMENTS

CONTENTS

1 INTRODUCTION 1
1.1 CANCER 1
1.1.1 Diagnosis of cancer 2
1.1.2 Therapy of cancer 4
1.1.3 Theranostics 5
1.2 NANOPARTICLES 6
1.2.1 Localized Surface Plasmon Resonance 7
1.2.2 Required properties for in vivo use 12
1.2.3 Gold nanoparticle synthesis and functionalization 17
1.3 GOLD NANOPARTICLES AS A THERANOSTIC AGENT 20
1.3.1 Photoacoustic imaging 20
1.3.2 Surface Enhanced Raman Scattering 23
1.3.3 Computed Tomography 26
1.3.4 Photothermal therapy 28
1.3.5 Nanotheranostics 31
1.4 OBJECTIVES 32
2 ASSESSMENT OF THE THERANOSTIC POTENTIAL OF GOLD NANOSTARS – A MULTIMODAL IMAGING AND PHOTOTHERMAL TREATMENT STUDY. 35
2.1 INTRODUCTION 35
2.2 MATERIALS AND METHODS 38
2.2.1 Synthesis and chemical functionalization of nanostars 38
2.2.2 Dynamic light scattering and zeta protocol 39
2.2.3 Transmission Electron Microscopy 39
2.2.4 Cell culture 40
2.2.5 Inductively coupled plasma optical emission spectroscopy (ICP-OES) 40
2.2.6 In vivo xenograft model and nanostar administration 40
2.2.7 Photoacoustic imaging 41
2.2.8 Computed tomography (CT) 41
2.2.9 Photothermal therapy (PTT) 41
2.2.10 Magnetic resonance imaging (MRI) 42

2.2.11 Bioluminescence imaging (BLI) *42*
2.2.12 Histopathology *42*
2.2.13 Data analysis *43*
2.3 RESULTS 43
2.3.1 Synthesis and functionalization of nanostar-shaped AuNPs optimized for in vivo use *43*
2.3.2 PAI and CT confirm efficient nanostar uptake by tumor cells *47*
2.3.3 Effective in vitro photothermal tumor cell ablation using gold nanostars *50*
2.3.4 In vivo CT and PAI confirms nanostar delivery into tumors *51*
2.3.5 Gold nanostars mediate in vivo photothermal therapy *52*
2.4 DISCUSSION 58
2.5 CONCLUSION 62
3 UNREVEALING THE REASONS FOR THE INEFFECTIVENESS OF PASSIVE TARGETING USING NANOSTARS. **63**
3.1 INTRODUCTION 63
3.2 MATERIALS & METHODS 65
3.2.1 Nanostars synthesis and functionalization *65*
3.2.2 Darkfield microscopy analysis of cell/ nanostar interaction. *66*
3.2.3 In vivo biodistribution using ICP-OES and darkfield microscopy. *66*
3.2.4 In vivo photothermal treatment and evaluation with BLI and MRI *67*
3.3 RESULTS 67
3.3.1 SAM functionalization and characterization *67*
3.3.2 Difference in cellular uptake by changing the end group of the SAM. *68*
3.3.3 In vivo biodistribution of nanostars after systemic administration *71*
3.3.4 In vivo PTT after passive targeting of the tumor *74*
3.4 DISCUSSION 79
3.5 CONCLUSION 82
4 LIMITING THE PROTEIN CORONA: A SUCCESSFUL STRATEGY FOR *IN VIVO* ACTIVE TARGETING OF ANTI-HER2 NANOBODY-FUNCTIONALIZED NANOSTARS. **84**
4.1 INTRODUCTION 84
4.2 MATERIAL AND METHODS 86
4.2.1 Nanostar synthesis, functionalization and characterization *86*
4.2.2 Cell culture. *87*
4.2.3 Darkfield microscopy *87*
4.2.4 In vivo tumor model and photoacoustic imaging of the nanostars in vivo. *88*

4.2.5 Histopathology *89*
4.2.6 Statistical analysis *89*
4.3 RESULTS 89
4.3.1 Nanostar biofunctionalization *89*
4.3.2 In vitro visualization of active targeting using biofunctionalized nanostars. *92*
4.3.3 Reducing the size of the protein corona reduces passive targeting *96*
4.3.4 In vitro visualization of active targeting using biofunctionalized nanostars. *99*
4.3.5 In vitro visualization of active targeting using biofunctionalized nanostars. *101*
4.3.6 In vivo imaging of biofunctionalized nanostars. *105*
4.4 DISCUSSION 110
4.5 CONCLUSION 113
5 DEVELOPMENT OF RAMAN-LABELED NANOSTARS AS A BIOCOMPATIBLE TUMOR CONTRAST AGENT FOR *IN VIVO* SERS IMAGING. 114
5.1 INTRODUCTION 114
5.2 MATERIALS AND METHODS 116
5.2.1 Nanostars synthesis and functionalization *116*
5.2.2 Darkfield microscopy analysis of cell- nanostar interaction. *116*
5.2.3 Evaluation of in vivo biodistribution using ICP-OES and darkfield microscopy. .. *117*
5.3 RESULTS 117
5.3.1 Nanostar synthesis and functionalization with SERS label *117*
5.3.2 SERS to visualize the in vitro uptake in tumor cells *121*
5.3.3 SERS as an in vivo imaging tool using nanostars as contrast agents *123*
5.3.4 Discussion *125*
CONCLUSION 127
6 CONCLUSION 128
7 FUTURE PERSPECTIVES. 133
SCIENTIFIC CONTRIBUTIONS 154

LIST OF TABLES

TABLE 1.1 EXAMPLES OF NANOPARTICLES USED AS A CANCER THERANOSTIC AGENT 5
TABLE 2.1 TEMPERATURE DIFFERENCE OF THE IRRADIATED SKIN COMPARED TO THE BODY TEMPERATURE SHOWN FOR DIFFERENT POWERS AND IRRADIATION SURFACES 53
TABLE 3.1. LSPR SHIFT, HYDRODYNAMIC DIAMETER SHIFT, ZETAPOTENTIAL AND PROTEIN CORONA INCREASE FOR THREE DIFFERENT FUNCTIONALIZATION OF THE NANOSTARS EITHER, WITH SAM MAL, SAM MALOH OR SAM COOH. DATA REPRESENTS MEAN VALUES AND STANDARD DEVIATIONS OF 3 INDEPENDENT EXPERIMENTS. 68
TABLE 4.1 FOR THE DIFFERENT SETS OF NANOSTARS FUNCTIONALIZED WITH NANOBODIES, THE LSPR BAND SHIFT, HYDRODYNAMIC DIAMETERS AND ZETAPOTENTIAL ARE REPORTED. DATA REPRESENT MEAN VALUES ± STANDARD DEVIATIONS FOR THREE INDEPENDENT EXPERIMENTS. 91
TABLE 4.2 ZETAPOTENTIAL GIVEN FOR THE NANOSTARS EITHER NON-BLOCKED (MAL) OR BLOCKED WITH DIFFERENT TYPES OF MOLECULES 98
TABLE 5.1. FOR A GIVEN SET OF DTNB CONCENTRATION THE LSPR BAND SHIFT, HYDRODYNAMIC DIAMETER INCREASE IS REPORTED TOGETHER WITH THE MAXIMUM SALT CONCENTRATION WHERE THE NANOSTARS REMAIN IN SUSPENSION. 118

LIST OF FIGURES

FIGURE 1.1. SCHEMATIC OVERVIEW OF THE NON-INVASIVE IMAGING TECHNIQUES. (A) MAGNETIC RESONANCE IMAGING (B) X-RAY COMPUTED TOMOGRAPHY (C) POSITRON EMISSION TOMOGRAPHY (D) ULTRASOUND (E) FLUORESCENCE IMAGING (F) PHOTOACOUSTIC IMAGING. 4

FIGURE 1.2. SCHEMATIC DRAWING OF THE LSPR EFFECT. 8

FIGURE 1.3. A. TEM PICTURE OF NANORODS HAVING DIFFERENT ASPECT RATIO. B. LSPR SPECTRA OF NANORODS WITH INCREASING ASPECT RATIO BY USING LOWER GOLD SEED CONCENTRATION DURING SYNTHESIS. 10

FIGURE 1.4. A. SEM PICTURE OF THE NANOCAGES STARTING FROM SILVER CUBES (A) TO GOLD NANOCAGES (D). AS INSET A TEM PICTURE WHERE THE HOLLOW SHAPE OF THE NANOCAGES IS SHOWN. B. LSPR SPECTRA OF THE NANOCAGES AFTER ADDITION OF DIFFERENT VOLUMES OF GOLD SALT RESULTING IN THICKER GOLD WALLS. DIFFERENT COLORS ARE OBSERVED FOR THESE NANOCAGES AS SEEN ON THE PHOTOGRAPH 11

FIGURE 1.5. A. SEM PICTURE OF THE NANOSTARS HAVING AN INCREASING LENGTH OF THEIR BRANCHES. B. LSPR SPECTRA OF THESE NANOSTARS HAVING A DIFFERENT LSPR MAXIMUM. 12

FIGURE 1.6. SCHEMATIC DRAWING OF THE BIOLOGICAL WINDOW (650-900 NM) WHERE HEMOGLOBIN AND WATER SHOW MINIMAL ABSORPTION 13

FIGURE 1.7. SCHEMATIC REPRESENTATION OF THE ENHANCED PERMEABILITY AND RETENTION EFFECT IN THE TUMOR 14

FIGURE 1.8. SCHEMATIC OVERVIEW HOW POLYETHYLENE GLYCOL PREVENTS UPTAKE BY THE RES (A) NANOPARTICLES (A1) ARE COATED WITH OPSONIN PROTEINS (A2) AND ASSOCIATE WITH MACROPHAGES (A3) FOR TRANSIT TO THE LIVER (A4). MACROPHAGES STATIONARY IN THE LIVER, KNOWN AS KUPFFER CELLS, ALSO PARTICIPATE IN NANOPARTICLE SCAVENGING. (B) NANOPARTICLES COATED WITH PEG COATING (B1) PREVENTS THIS OPSONIZATION (B2), RESULTING IN DECREASED LIVER ACCUMULATION (B3) AND INCREASED AVAILABILITY OF THE AUNP FOR IMAGING OR THERAPY. 15

FIGURE 1.9 (A) CONVENTIONAL ANTIBODY WITH TWO HEAVY AND TWO LIGHT CHAINS. (B) HEAVY-CHAIN ONLY ANTIBODY FROM A CAMELID THAT COMPRISES ONLY TWO IDENTICAL HEAVY CHAINS. (C) NANOBODY THAT CONSISTS OF THE VARIABLE DOMAIN OF ONE HEAVY CHAIN OF SUCH A HEAVY CHAIN ONLY ANTIBODY (VHH). .....

FIGURE 1.10. SCHEMATIC DRAWING OF THE SYNTHESIS AND FUNCTIONALIZATION OF AUNPS EITHER USING IN SITU OR EX SITU STRATEGY 18

FIGURE 1.11. SCHEMATIC DRAWING OF SELF-ASSEMBLED MONOLAYER AROUND THE AUNPS WITH THEIR SPECIFIC SUBUNITS. 19

FIGURE 1.12. SCHEMATIC REPRESENTATION OF PAI USING GOLD NANOPARTICLES AS A CONTRACT AGENT 20
FIGURE 1.13. OVERVIEW OF THE PA MAIN RESULTS WITH SILICA COATED NANORODS. LEFT. ACTIVE TARGETING OF TWO DIFFERENT CELL LINES USING SILICA COATED NANORODS EITHER HAVING THEIR ABSORPTION MAXIMUM AT 780 NM (YELLOW) OR RED (830 NM). ON TOP THE ULTRASOUND PICTURE, WHERE IN THE MIDDLE THE PA SIGNAL AT 830 NM INDICATES WHICH CELL TYPE CONTAINS SILICA COATED NANORODS. AT THE BOTTOM THE UNMIXING OF BOTH DIFFERENT NANORODS, SHOWING THE SELECTIVITY OF THESE NANORODS FOR THE CANCER CELLS. RIGHT. ON TOP THE 3D ULTRASOUND OF THE TUMOR BEFORE AND AFTER I.V. INJECTION OF NON BIOFUNCTIONALIZED NANORODS AND ON THE BOTTOM THE PA SIGNAL, WHERE AN INCREASE OF SIGNAL IS MEASURED AFTER NANOROD INJECTION. 22
FIGURE 1.14. *IN VIVO* CANCER TARGETING AND SURFACE ENHANCED RAMAN DETECTION BY BIOFUNCTIONALIZED GOLD NANOSPHERES RECOGNIZGING THE BIOMARKER EGFR. SERS SPECTRA ARE SHOWN FOR THE TUMOR AND THE LIVER BY USING TARGETED (A) AND NON-TARGETED (B) NANOSPHERES. C. PHOTOGRAPHS SHOWING THE LASER BEAM FOCUSING ON EITHER THE LIVER OR THE TUMOR FOR OBTAINING THE SERS SPECTRUM. 25
FIGURE 1.15. *IN VIVO* X-RAY CT OF MOUSE BEFORE INJECTION (A), 6 HOURS AFTER INJECTION OF EITHER UNTARGETED NANOSPHERES (B) OR TARGETED NANOSPHERES (C). THE LAST ONE SHOW CLEAR TUMOR ACCUMULATION WHILE THE UNTARGETED DOESN'T. CT-VALUES ARE QUANTIFIED FOR THE TUMOR, LIVER AND KIDNEY CONFIRMING THE CT IMAGES 27
FIGURE 1.16. OVERVIEW OF *IN VIVO* PTT EXPERIMENTS USING NANORODS. TOP. THERMOGRAPHIC SURVEILLANCE OF PHOTOTHERMAL HEATING IN NANOROD INJECTED (TOP) AND SALINE-INJECTED (BOTTOM) MICE. BOTTOM. VOLUMETRIC CHANGES IN MDA-MB-435 TUMOR SIZES ARE PLOTTED OVER TIME AFTER PTT IRRADIATION (810 NM, 2 W/CM2, 5 MIN USING NANORODS AFTER I.V. INJECTION. ON THE RIGHT, THE SURVIVAL OF MICE AFTER IRRADIATION IS PLOTTED VERSUS TIME AFTER IRRADIATION. 30
FIGURE 1.17. LEFT. THE SCHEMATIC DRAWING OF THE TRIPLE MODALITY IMAGING CONCEPT FOR SURGICAL REMOVAL OF THE BRAIN TUMOR. RIGHT. TWO-DIMENSIONAL AXIAL MRI, PHOTOACOUSTIC AND RAMAN IMAGES. THE POST-INJECTION IMAGES OF ALL THREE MODALITIES SHOWED CLEAR TUMOR VISUALIZATION (DASHED BOXES OUTLINE THE IMAGED AREA) 32
FIGURE 2.1. UV-VIS ABSORPTION SPECTROSCOPY OF NANOSTARS USING DIFFERENT FLOW RATES FOR $HAuCl_4$, WITH A SHIFT OF THE LSPR BAND TO THE NIR REGION WITH LOWER FLOW RATES. TEM IMAGES OF THE NANOSTARS FROM TOP TO BOTTOM THAT WERE GENERATED WITH FLOW RATES OF 50 ML/MIN, 25 ML/MIN AND 12.5 ML/MIN, RESPECTIVELY. .....

FIGURE 2.2. UV-VIS ABSORPTION SPECTROSCOPY OF NANOSTARS, NORMALIZED TO ABSORBANCE OF 1 A.U., EITHER AFTER SYNTHESIS (NANOSTARS) OR AFTER SAM FUNCTIONALIZATION (NANOSTARS SAM)..... 45

FIGURE 2.3. A. UV-VIS ABSORPTION SPECTROSCOPY OF NANOSTARS FOR 1 AND 7 DAYS IN EITHER WATER OR CELL CULTURE MEDIUM. B. DLS INTENSITY PLOTS OF THE NANOSTARS IN WATER FOR 1 AND 7 DAYS SHOWED NO INCREASE OR DECREASE IN DIAMETER. C. DLS INTENSITY PLOTS OF THE NANOSTARS IN CELL CULTURE MEDIUM FOR 1 AND 7 DAYS. D. THE ZETA-POTENTIAL OF THE NANOSTARS FUNCTIONALIZED WITH THE SAM IN WATER WITH AN AVERAGE VALUE OF -41.3 +/- 1.2 NANOSTARS ARE STABLE IN WATER AND CELL CULTURE MEDIUM. .....

FIGURE 2.4 LEFT. PAI IMAGES OF NANOSTARS AND WATER IN TUBE, WHICH WERE QUANTIFIED BY PLOTTING THE SIGNAL AMPLITUDES. RIGHT. CT IMAGES OF MICRO CENTRIFUGE TUBES EITHER FILLED WITH WATER OR NANOSTARS SUSPENSION. THE CORRESPONDING SIGNAL AMPLITUDES WERE USED FOR QUANTIFICATION. (N=3)..... 47

FIGURE 2.5. INTRACELLULAR GOLD CONCENTRATION OF DIFFERENT INCUBATION TIME SLOTS DETERMINED BY ICP-OES. AS INSET A TEM IMAGES VISUALIZING THE NANOSTARS INSIDE THE TUMOR CELLS. .....

FIGURE 2.6 LEFT. PA IMAGES OF A PHANTOM LOADED WITH TUMOR CELLS (N=3) INCUBATED FOR DIFFERENT TIMES WITH THE NANOSTARS. RIGHT. PA SIGNAL PLOTTED FOR THE DIFFERENT GOLD MASSES PER CELL, WHERE THE DOTTED LINE SUGGESTS AN EXPONENTIAL RELATION BETWEEN THOSE 2 VARIABLES..... 49

IGURE 2.7 LEFT. CT IMAGES OF A PHANTOM LOADED WITH TUMOR CELLS (N=3) INCUBATED FOR DIFFERENT TIMESWITH THE NANOSTARS. RIGHT. CT SIGNAL QUANTIFIED AS DENSITY (GREY VALUES) PLOTTED FOR THE DIFFERENT GOLD MASSES PER CELL, WHERE THE DOTTED LINE SUGGESTS AN EXPONENTIAL RELATION BETWEEN THOSE 2 VARIABLES. 49

FIGURE 2.8 A. TEMPERATURE PROFILE OF TUBES THAT WERE FILLED WITH EITHER GOLD NANOSTARS (4.6×10^{10} NANOSTARS/ML) OR WATER AND WERE IRRADIATED WITH A CONTINUOUS LASER (2 W/CM^2)..... 50

FIGURE 2.9 LEFT. FLUORESCENCE IMAGES OF THE LIVING CELLS STAINED WITH CALCEIN AM FOR TUMOR CELLS (N=3) INCUBATED FOR DIFFERENT TIMES WITH THE NANOSTARS AFTER PTT. RIGHT. RELATIVE GREEN PIXEL NUMBERS PLOTTED FOR THE GOLD MASS PER CELL WHERE THE FLUORESCENCE SIGNAL IS RELATIVELY CALCULATED TO THE CONTROL SAMPLE (0H). 51

FIGURE 2.10 A. CT IMAGES BEFORE AND AFTER INJECTION OF NANOSTARS INTO THE TUMOR. AN INCREASED CONTRAST IS NOTICED AT THE TUMOR SITE AFTER GOLD NANOSTARS INJECTION (ARROW) B. *IN VIVO* PA IMAGES BEFORE AND 24 H AFTER NANOSTAR INJECTION. THE PAI

SIGNAL (RED PIXELS) IS OVERLAID OVER THE ANATOMICAL ULTRASOUND IMAGES (GREY PIXELS).....

FIGURE 2.11 TOP. NIR IMAGES OF THE SUBCUTANEOUS INJECTED NANOSTAR/MATRIGEL CONCENTRATION SOLUTION FOR DIFFERENT CONCENTRATIONS LEFT. TEMPERATURE DIFFERENCE COMPARED TO THE BODY TEMPERATURE DURING PTT OF DIFFERENT NANOSTARS/MATRIGEL CONCENTRATION SOLUTIONS. RIGHT. THE MAXIMUM TEMPERATURE PLOTTED PER GOLD CONCENTRATION WHERE THE DOTTED LINE SUGGEST A LOGARITHMIC CORRELATION BETWEEN THOSE TWO VARIABLES.....54

FIGURE 2.12 A. *IN VIVO* BLI BEFORE (DAY 0) AND AFTER PTT (DAYS 1, 5, 8) ILLUSTRATED IN A COLOR-CODED INTENSITY MAP. A QUANTIFICATION OF THE BLI SIGNAL INTENSITY RELATIVE TO DAY 0 (SET AT 100% PER MICE) IS PLOTTED FOR BOTH NANOSTAR-INJECTED AND CONTROL (PBS-INJECTED) TUMORS (RT) B. MR IMAGES OF THE TUMOR-BEARING HIND LIMBS TAKEN AT CORRESPONDING TIME POINTS (DAYS) AFTER NANOSTAR- OR PBS-INJECTION. THE YELLOW ARROW INDICATES THE TUMOR DAMAGE (HYPOINTENSE AREA) AFTER PTT AT THE NANOSTAR-INJECTED TUMOR. THE RELATIVE MASS VOLUMES WERE QUANTIFIED RELATIVE TO DAY 0 (SET AT 100% PER MICE). (FOR BOTH BLI AND MRI GRAPHS THE ERROR BARS REPRESENT SD; N = 6) 56

FIGURE 2.13 A COMPLETE OVERVIEW OF THE HISTOLOGICAL SECTION OF EITHER THE TUMOR INJECTED WITH NANOSTARS (TOP) OR PBS (BOTTOM) AFTER THERAPY. THE BLUE 'CLOUD' IN THE TUMOR IS CAUSED BY THE GOLD NANOSTARS, WHICH IS ABSENT IN THE CONTROL TUMOR 57

FIGURE 2.14 A. BRIGHT FIELD MICROSCOPY IMAGES OF CONTROL (RIGHT) AND NANOSTAR (LEFT) INJECTED H&E STAINED TUMOR SECTIONS. DEFRAGMENTED NUCLEI OF THE TUMOR CELLS COULD BE VISUALIZED AFTER THERAPY. B. *EX VIVO* TEM IMAGES OF TUMOR CELLS THAT INDICATE THE PRESENCE OF NANOSTARS CLUSTERS IN ENDOSOMES. THE RIGHT PANEL SHOWS A ZOOMED SECTION OF THESE ENDOSOMES WITH VESICULAR STRUCTURES VISIBLE AROUND THE NANOSTARS.....58

FIGURE 3.1. NANOSTAR/CELL MEAN SIGNAL INTENSITY DEDUCTED OF DARKFIELD MICROSCOPY IMAGES PLOTTED OF SKOV3 CELLS INCUBATED EITHER WITH NANOSTARS SAM MAL, SAM MALOH AND SAM COOH FOR DIFFERENT TIME POINTS (1, 3, 6, 12 AND 24H; REPEATED MEASURED TWO WAY ANOVA) 69

FIGURE 3.2. DARKFIELD MICROSCOPY IMAGES OF SKOV3 CELLS INCUBATED WITH EITHER NANOSTARS SAM MAL, SAM MALOH AND SAM COOH FOR DIFFERENT TIME POINTS (1, 3, 6, 12 & 24H) 70

FIGURE 3.3. LEFT: RELATIVE GOLD CONCENTRATION OF DIFFERENT ORGANS AT TWO TIME POINTS (1 AND 24H) AFTER INJECTION OF EITHER NANOSTARS SAM MAL OR PBS INJECTION WHERE THE RELATIVE GOLD CONCENTRATION IS PLOTTED IN COMPARISON TO

THE INJECTED AMOUNT OF GOLD FOR THE DIFFERENT TISSUES (ONE WAY ANOVA). RIGHT: NANOSTAR/CELL MEAN SIGNAL INTENSITY OF THE DIFFERENT ORGANS 24H AFTER INJECTION FOR EITHER NANOSTARS SAM MAL OF PBS INJECTION (T-TEST). 71
FIGURE 3.4. DARKFIELD IMAGES OF DIFFERENT ORGANS AFTER I.V. INJECTION OF EITHER NANOSTARS SAM MAL OR PBS. 73
FIGURE 3.5 RELATIVE GOLD CONCENTRATION OF TISSUES EITHER 1H AFTER NANOSTARS COOH, 24H AFTER NANOSTAR SAM COOH OR PBS INJECTION WHERE THE RELATIVE GOLD CONCENTRATION IS PLOTTED IN COMPARISON TO THE INJECTED AMOUNT OF GOLD FOR THE DIFFERENT TISSUES (ONE WAY ANOVA) 74
FIGURE 3.6 THE TEMPERATURE INCREASE PLOTTED OVER TIME WHERE THE TUMOR IS IRRADIATED AT TIME POINT 0 UNTIL 300 SEC WHERE NO SIGNIFICANCE WAS MEASURED (ANOVA; $P \leq 0.05$) 75
FIGURE 3.7. RELATIVE BLI INTENSITY (LEFT) AND TUMOR VOLUMES (RIGHT) OF THE TUMORS AFTER PTT FOR EITHER I.V. INJECTED NANOSTARS OR PBS MICE. TREATMENT WAS EXECUTED AT DAY 1 WHERE NO SIGNIFICANCE WAS SHOWN OVER TIME FOR THE NANOSTAR AND PBS ADMINISTERED MICE (ANOVA; $P \leq 0.05$) 76
FIGURE 3.8 MEAN WEIGHT OF THE MICE IN EACH GROUP DURING THE FOLLOW UP AFTER PTT. NO SIGNIFICANT DECREASE IN WEIGHT WAS MEASURED (ANOVA; $P \leq 0.05$) 77
FIGURE 3.9 HISTOLOGY IMAGES OF SKOV3 TUMORS EITHER STAINED TARGETING CD31 OR ASMA 77
FIGURE 3.10. HISTOLOGY IMAGES AFTER H&E STAINING OF THE TUMOR, SPLEEN, LIVER, KIDNEY AND HEART AFTER EITHER I.V. INJECTION OF THE NANOSTARS SAM MAL OR PBS. 78
FIGURE 4.1 UV-VIS ABSORPTION SPECTROSCOPY FOR NANOSTARS FUNCTIONALIZED WITH VARIOUS CONCENTRATIONS OF EITHER MONOMER 2RB17C (A), MONOMER CABCII10 (MONOMER), REDUCED DIMER 2RB17C (C), REDUCED DIMER CABCII10 (C) 90
FIGURE 4.2 UV-VIS ABSORPTION SPECTROSCOPY OF THE NANOSTARS – BIOFUNCTIONALIZED AND/OR BLOCKED WITH SHOH - IN HEPES BUFFER (A), CELL CULTURE MEDIUM WITH SERUM (B) AND CELL CULTURE MEDIUM WITHOUT SERUM (C). 92
FIGURE 4.3 DARKFIELD MICROSCOPY IMAGES OF SKOV3 CELLS (GREEN) INCUBATED WITH EITHER NON-BIOFUNCTIONALIZED NANOSTARS (MAL), BIOFUNCTIONALIZED WITH 2RB17C (POS) AND CABCII10 (NEG) FOR DIFFERENT INCUBATION CONDITIONS VISUALIZED BY THE YELLOW SPOTS. .....
FIGURE 4.4 DARKFIELD MICROSCOPY IMAGES OF CHO CELLS INCUBATED WITH EITHER NON-BIOFUNCTIONALIZED NANOSTARS (MAL), BIOFUNCTIONALIZED WITH 2RB17C (POS) AND CABCII10 (NEG) FOR DIFFERENT INCUBATION CONDITIONS. 95

FIGURE 4.5 NANOSTAR/ CELL INTENSITY FOR SKOV3 CELLS (A) OR CHO CELLS (B) INCUBATED WITH EITHER NON-BIOFUNCTIONALIZED NANOSTARS (MAL), BIOFUNCTIONALIZED WITH 2RB17C (POS) AND CABCII10 (NEG) FOR DIFFERENT INCUBATION CONDITIONS. 96
FIGURE 4.6 NORMALIZED ABSORBANCE OF THE NANOSTARS THAT ARE FUNCTIONALIZED WITH THE BLOCKING AGENTS SHNH (A), SHOH (B), SHCOOH (C), PEGCH (D) AND PEHCOOH (E) FOR DIFFERENT CONCENTRATIONS (1,2 MM; 2,4 MM AND 12 MM) IN EITHER MES-BUFFER OR CELL CULTURE MEDIUM WITH SERUM. 97
FIGURE 4.7 HYDRODYNAMIC DIAMETER DIFFERENCE SHOWN FOR THE DIFFERENCE NANOSTARS - NON-BLOCKED OR BLOCKED – UNDER SERUM-CONTAINING CONDITIONS COMPARED TO THEIR HYDRODYNAMIC DIAMETER IN WATER (CONTROL) 99
FIGURE 4.8 DARKFIELD IMAGES OF SKOV3 CELLS INCUBATED WITH THE DIFFERENT (NON-)BLOCKED NANOSTARS DURING 6 OR 24 H OF INCUBATION 100
FIGURE 4.9 NANOSTAR/CELL INTENSITY PLOTTED FOR DIFFERENT SKOV3 CELLS INCUBATED WITH NON-BIOFUNCTIONALIZED NANOSTARS EITHER NON-BLOCKED OR IN THE PRESENCE OF A BLOCKING AGENT. 101
FIGURE 4.10 DIFFERENCES IN HYDRODYNAMIC DIAMETERS MEASURED FOR THE NANOSTARS – BIOFUNCTIONALIZED AND/OR BLOCKED WITH SHOH - IN CELL CULTURE MEDIUM CONTAINING SERUM COMPARED TO THE HYDRODYNAMIC DIAMETER MEASURED IN WATER. DATA IS SHOWN FOR SKOV3 CELL 102
FIGURE 4.11 DARKFIELD MICROSCOPY IMAGES OF SKOV3 CELLS INCUBATED WITH EITHER NON-BIOFUNCTIONALIZED NANOSTARS (MAL), BIOFUNCTIONALIZED WITH 2RB17C (POS) OR CABCII10 (NEG). ALL NANOSTARS WERE FUNCTIONALIZED WITH THE BLOCKING AGENT SHOH. 103
FIGURE 4.12 DARKFIELD MICROSCOPY IMAGES OF CHO CELLS INCUBATED WITH EITHER NON-BIOFUNCTIONALIZED NANOSTARS (MAL), BIOFUNCTIONALIZED WITH 2RB17C (POS) OR CABCII10 (NEG). ALL NANOSTARS WERE FUNCTIONALIZED WITH THE BLOCKING AGENT SHOH. 104
FIGURE 4.13 NANOSTAR/ CELL INTENSITY FOR SKOV3 CELLS (A) OR CHO CELLS (B) INCUBATED WITH EITHER NON-BIOFUNCTIONALIZED NANOSTARS (MAL), BIOFUNCTIONALIZED WITH 2RB17C (POS) AND CABCII10 (NEG) BUT ALL FUNCTIONALIZED WITH BLOCKING AGENT SHOH FOR DIFFERENT INCUBATION CONDITIONS 105
FIGURE 4.14 . TOP: PHOTOACOUSTIC IMAGES OVERLAID ON ULTRASOUND IMAGES ARE SHOWN FOR SKOV3 TUMORS BEFORE AND AFTER SYSTEMIC INJECTION (I.V.) OF NON-BIOFUNCTIONALIZED NANOSTARS (MAL) OR BIOFUNCTIONALIZED WITH EITHER 2RB17C (POS) OR CABCII10 (NEG). ALL NANOSTARS WERE ALSO BLOCKED WITH SHOH. THE PA SIGNAL OF THE NANOSTARS IS SHOWN IN GREEN PIXELS. BOTTOM: QUANTIFICATION OF THE PA SIGNALS. 106

FIGURE 4.15 PHOTOACOUSTIC IMAGE OF THE SKOV3 TUMOR AFTER SPECTRAL UNMIXING TO VISUALIZE OXYHEMOGLOBINE (RED) AND THE 2RB17C FUNCTIONALIZED NANOSTARS, BLOCKED WITH SHOH (GREEN). BY SPECTRAL UNMIXING, A DISTINCTION BETWEEN THE OXYHEMOGLOBINE AND NANOSTARS SIGNAL WAS MADE .....

FIGURE 4.16 REPRESENTATIVE *EX VIVO* DARKFIELD IMAGES OF THE TUMOR TISSUE SECTION AFTER SYSTEMIC INJECTION OF THE 2RB17C FUNCTIONALIZED NANOSTARS (POS), CABCII10 FUNCTIONALIZED NANOSTARS (NEG) AND NON-BIOFUNCTIONALIZED NANOSTARS (ALL FUNCTIONALIZED WITH THE BLOCKING AGENT SHOH). THE NANOSTARS ARE VISUALIZED AS YELLOW SPOTS INSIDE THE TUMOR TISSUE..... 108

FIGURE 4.17 *EX VIVO* DARKFIELD IMAGES OF SECTIONS OF DIFFERENT ORGANS OF MICE THAT WERE SYSTEMICALLY INJECTED WITH THE 2RB17C FUNCTIONALIZED NANOSTARS (POS), CABCII10 FUNCTIONALIZED NANOSTARS (NEG) AND NON-BIOFUNCTIONALIZED NANOSTARS (ALL WERE FUNCTIONALIZED WITH THE BLOCKING AGENT SHOH). THE NANOSTARS ARE VISUALIZED AS YELLOW SPOTS INSIDE THE TUMOR TISSUE. 109

FIGURE 5.1 LEFT: UV-VIS OF THE NANOSTARS FUNCTIONALIZED WITH A CONCENTRATION RANGE OF DTNB. A SECOND BAND IS APPEARING DUE TO THE FORMATION OF TNB-. RIGHT: LSPR BAND OF THE NANOSTARS FUNCTIONALIZED WITH 0.1 MM DTNB FOR DIFFERENT SALT CONCENTRATIONS, SHOWING THE NANOSTAR INSTABILITY BY A DECREASE IN INTENSITY..... 118

FIGURE 5.2 LEFT: UV-VIS SPECTRUM OF THE 'NAKED' NANOSTARS, NANOSTARS FUNCTIONALIZED WITH 0.1 MM DTNB AND WITH A SAM. AS INSET THE LSPR BAND SHIFT TO THE NIR REGION DUE TO THE BINDING OF THESE MOLECULES TO THE NANOSTAR SURFACE. RIGHT: LSPR BAND OF THE NANOSTARS FUNCTIONALIZED WITH DTNB AND SAM FOR DIFFERENT SALT CONCENTRATIONS SHOWING NO INSTABILITY. 119

FIGURE 5.3 LEFT: BRIGHTFIELD MICROSCOPY IMAGES OF THE NANOSTARS DRIED ON A SILICA WAFER WHERE THE SERS SIGNAL INTENSITY AT 1333 CM^{-1} IS VISUALIZED IN THE ZOOM PICTURE. RIGHT: SERS SPECTRUM OF THE CORRESPONDING NANOSTARS EITHER LABELED WITH DTNB AND SAM OR ONLY FUNCTIONALIZED WITH THE SAM MOLECULE. 120

FIGURE 5.4 LEFT: DARKFIELD MICROSCOPY PICTURES WHERE AN INCREASE OF GOLD NANOSTARS INSIDE THE TUMOR CELLS IS VISUALIZED OVER TIME RIGHT: SERS SPECTRUM OF THE CORRESPONDING CELLS LABELED WITH NANOSTARS, SHOWING THE HIGHEST INTENSITY PEAK AT 1333 CM^{-1} 122

FIGURE 5.5 BRIGHTFIELD IMAGE OF A TUMOR CELL OVERLAID BY A SERS INTENSITY IMAGE WHERE AT HIGH INTENSITIES AT THE WAVENUMBER OF 1333 CM^{-1} YELLOW SPOTS ARE VISUALIZED. .....

FIGURE 5.6 SERS SPECTRUM OF THE LIVER AND TUMOR 3 HOURS AFTER I.V. INJECTION OF THE NANOSTAR WHERE THE BACKGROUND AND CONTROL TISSUE HAVE BEEN SUBTRACTED. FOR BOTH A CLEAR PEAK AT 1333 CM^{-1} WAS VISIBLE. 124
FIGURE 5.7 LEFT: DARKFIELD IMAGES OF THE DIFFERENT TISSUES WHERE NANOSTARS (GOLD SPOTS) WERE CLEARLY VISUALIZED INSIDE THE LIVER, SPLEEN AND IN LESS AMOUNT AT THE TUMOR BORDER. RIGHT: SERS SPECTRA OF THE DIFFERENT TISSUES WHERE A DTNB SPECTRUM WAS OBSERVED FOR THE SPLEEN, LIVER AND TUMOR BORDER. 125

LIST OF APPENDICES

Appendix 1……..137

LIST OF ABBREVIATIONS AND ACRONYMS

Au	Gold
AuNP	Gold Nanoparticle
BLI	Bioluminescence Imaging
BSPP	bis(psulfonatophenyl)phenylphosphine dihydrate dipotassium
CNR	Contrast to noise ratio
COOH	Carboxyl
CT	Computed Tomography
CTAB	cetyltrimethylammonium bromide
Cu	Copper
DNA	Deoxyribonucleic acid
DTNB	5,5'-dithiobis-(2-nitrobenzoic acid)
EGFR	Epidermal Growth Factor Receptor
EPR	Enhanced Permeability and Retention
Fe	Iron
HER2	Human Epidermal Growth Factor 2
i.v.	Intravenous
LOD	Limit of detection
LSPR	Localized Surface Plasmon Region
MAL	Maleimide
MALOH	Maleimide / Hydroxyl
MRI	Magnetic Resonance Imaging
NIR	Near-infrared region
NP	Nanoparticle
PA	Photoacoustic
PAI	Photoacoustic Imaging
PEG	Poly-ethylene glycole
PEGCH	O-(2-Mercaptoethyl)-O′-methyl-hexa(ethylene glycol)
PEGCOOH	(O-(2-Mercaptoethyl)-O′-(2-carboxyethy) hepta-ethylene glycol
PET	Positron Emission Tomography
PTT	Photothermal therapy

PVP	Polyvinylpyrrolidone
RES	Reticuloendothelial System
SAM	Self-assembled Monolayer
SDS-PAGE	Sodium dodecyl sulphate polyacrylamide gel electrophoresis
SEM	Scanning electron microscopy
SERS	Surface Enhanced Raman Scattering
SHCOOH	3-mercaptopropionic acid
SHNH	2-mercaptoethylamine
SHOH	2-mercaptoethanol
SKOV3	Human ovarian carcinoma cell line
SPIO	Superparamagnetic iron oxide
TEM	Transmission electron microscopy
UV	Ultra-Violet light
VEGFR	Vascular epidermal growth factor

1 INTRODUCTION

Currently, cancer is still one of the most deadly diseases in the world. In Europe 3.45 million new cases of cancer and 1.75 million deaths as a result of cancer are registered annually[1]. In view of these high numbers, various imaging and therapeutic techniques are currently employed as a standard of care for these patients. These techniques face still severe limitations to be practical and their usage depends on the actual cancer disease[2]. Therefore new approaches are needed to develop a target delivered therapy that can be monitored by imaging. Hereby solutions could be offered by the bionanotechnology field where nanoparticles may play a crucial role[3].

1.1 Cancer

The conception of cancer has changed over the last decades. While previously tumors were seen as masses of proliferating cancer cells, nowadays they are noted as complex tissues consisting of different cell types participating in several cell interactions. The tumor cells interact specifically with other cells, ranging from immune to epithelial cells, resulting in an unique tumor microenvironment [4].Contributing to this microenvironment, ten essential hallmarks are defined, where each one is crucial for cancer development. The follow up of these hallmarks defines the neoplastic characteristics of each tumor[5].

Each hallmark is characterized by the down or up regulation of specific biological molecules due to genetic mutations. One example is the human epidermal growth factor 2 receptor (HER2) showing an overexpression in 20-30 % of breast cancer which is assigned to the hallmark of sustaining proliferative signaling. This overexpression is associated with tumor aggressiveness and an increased probability for recurrent disease[6]. The main reason for this cause of aggressiveness is the role of the tyrosine kinase receptor as a transducing growth stimulator to the cell interior, enhancing cell proliferation. Having an over-expression, tumor cells are hyper-responsive to ambient levels of growth factors that normally would not trigger cell proliferation. This overexpressed receptor is an ideal target for cancer therapies, such as the monoclonal antibody Herceptin targeting HER2[6].

Overall, the hallmark of metastasis formation, the spread of the tumor cells of the primary tumor to other organsq is responsible for 90% of the human cancer deaths. Diagnosing and treating the tumor before the formation of metastases is still one of the main challenges in current cancer treatment[5].

1.1.1 Diagnosis of cancer

Until today, there is no single test that can diagnose cancer. Rather a combination of various techniques ranging from biomarker tests, histopathology after tumor biopsy and medical imaging techniques are required to verify if a patient has cancer. These imaging techniques are described as the visualization of the interaction of electromagnetic radiation or sound waves with an object as a tumor[7]. Since each imaging technique has its own key strengths and limitations, they are often complementary used for diagnostic imaging.

In the clinic, three imaging methods are often used for cancer diagnosis: magnetic resonance imaging (MRI), X-ray computed tomography (CT) and position emission tomography (PET)[8]. Contrast in MRI is based on the relaxation time of hydrogen proton spins after applying an external magnetic pulse (Figure 1.1). Having different hydrogen relaxation times in soft tissue with and without contrast agents, MRI is commonly used as a soft tissue contrast imaging tool

ideally for cancer imaging[9]. Still, MRI is an expensive technique necessitating long scanning times for generating high spatial resolution. Conversely, CT uses the X-ray attenuation properties of tissues/bones for generating contrast (Figure 1.1). With faster scanning times and broadly available instrumentation, CT is commonly used for diagnosing particular cancers, e.g. mammography for breast cancer[10]. At last, PET is based on the detection of ionizing radiation emitted by a radioactive contrast agent/ tracer (Figure 1.1). The radioactive label is typically part of a biologically active molecule (e.g. glucose) having a higher uptake or accumulation in specific cells such as tumor cells. These agents provide highly sensitive functional / metabolic imaging with limited anatomical information. This technique is routinely used for detecting tumors/metastasis using e.g. fluorodeoxyglucose or radiolabeled amino acids[9].

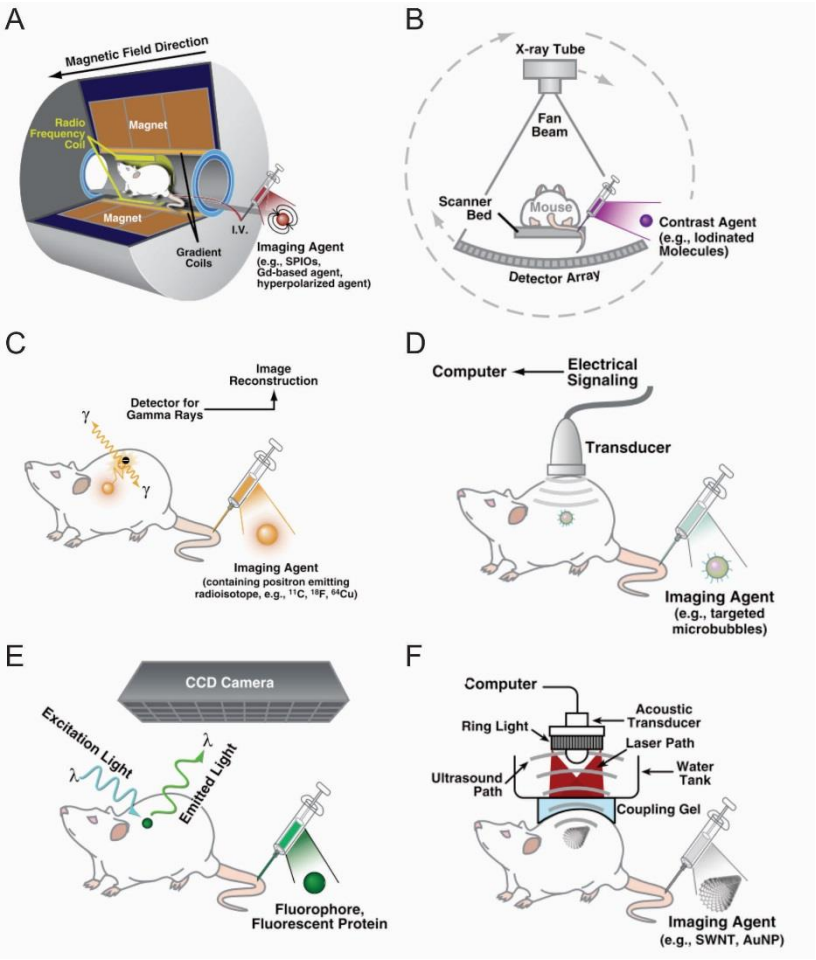

Figure 1.1. Schematic overview of the non-invasive imaging techniques. (A) Magnetic Resonance Imaging (B) X-ray Computed Tomography (C) Positron Emission Tomography (D) Ultrasound (E) Fluorescence Imaging (F) Photoacoustic imaging.

Less commonly used imaging techniques for cancer have gained particular interest in the field of biomedical research during the last years. Ultrasound, imaging the interaction of ultrasound waves with biological tissues, is commonly used for maternity imaging and in cardiology (Figure 1.1). By using microbubbles targeting cancer, this technique could be applied as a sensitive and cost efficient cancer imaging technique. Optical imaging techniques (fluorescence, bioluminescence, and Surface Enhanced Raman Imaging) rely on the emission of photons by specific molecules (Figure 1.1). Having high sensitivity due to the use of optical agents but low penetration depth, these techniques focus rather on preclinical imaging in small animals or as guidance during surgical removal of tumor lesions (interventional imaging). At last, photoacoustic imaging, a combination of optical and ultrasound imaging is making its way in the (pre-) clinical field (Figure 1.1). This technique relies on the thermo-elastic expansion of a contrast agent after laser irradiation with a nanosecond pulse. Consequently, it combines the benefits of both imaging techniques[11].

1.1.2 Therapy of cancer

The most critical step in cancer treatment is the actual therapy itself. This stage is highly dependent on the type and stage of the cancer.

Current common cancer treatment techniques are surgery, radiotherapy and chemotherapy, which are applied as single techniques or in combination[12]. Surgical removal is used when a non-metastasized tumor is located in non-crucial parts of organs. In the best case, all the tumor cells are removed during surgery, affecting healthy cells as least as possible[13]. For tumors located close to complex organs, radiotherapy is often opted. With this therapy ionizing radiation causes DNA damage that can be repaired efficiently by cells, but not by tumor cells. By applying the right radiation dose, tumor cells will be affected while healthy cells are able to recover. Still, radiotherapy efficiency is dependent on the amount of cells the radiation has to pass and an

efficient local application of the radiation[14]. Another common treatment technique for metastizing tumors in the clinic is chemotherapy, where specific cytotoxins are applied to inhibit growth or even kill fast proliferating cells like cancer cells. Unfortunately, next to cancer cells, other cells such as bone marrow, leukocytes etc. are also affected. In many cases a combination of chemotherapy is applied, where a cocktail of medicines is used to limit side effects and spread the toxicity over the whole body instead of over only one organ, and to limit the resistance against specific medicines. Overall these techniques are rather invasive, resulting in a long and complex recovery for the patient after therapy[15].

Because current cancer treatment approaches clearly have limitations and disadvantages, there is a huge interest in new therapeutic strategies, such as targeted delivery and hyperthermia. During hyperthermia treatment, heat is applied to the tumors resulting in a specific cell death. This heat can be applied on a local level at the tumor site or to the whole body. Currently this heat is applied by external fluid applied around the body, ultrasound, fluctuating magnetic fields or laser based therapy[16]. Moreover this heat can be used for thermally triggered drug release which can result in a specific cancer therapy[17].

1.1.3 Theranostics

In the last decade, major efforts have been intiated to develop more specific and individualized therapies to particular sub-types of tumors by combining the diagnostic and therapeutic capabilities into one agent[9]. Since cancer is such a complex disease, current therapies are only effective for a limited amount of patients in a specific stage of the disease. It is generally believed that by the integration of diagnostic and therapeutic capabilities into one agent, a more controlled and specific therapeutic protocol per individual could be achieved. This concept of combining diagnosis and therapy is called ‘theranostics’[3].

Table 1.1 Examples of nanoparticles used as a cancer theranostic agent

Trade Name	Description of Nanoparticle	Cancer targeted by the Nanoparticle	Phase of Development
Resovist	Carboxydextran-coated SPIO	MRI contast agent for imaging hepatocellular carcinoma	Approved
Nanotherm	Aminosilane-coated SPIO	Local ablation of glioblastoma multiform	Approved
Nanotherm	Aminosilane-coated SPIO	Pancreatic and prostate cancer	Phase 1
Aurimmune	Gold nanoparticle loaded with tumor necrosis factor	Solid tumors	Phase 1
AuroShell	Near-infrared irradiation with gold nanoshells (localized thermal ablation)	Head an Neck Cancers	Phase 0 (pilot study)
C-dots	PEG-coated SiO2	Melanoma	IND approved

Nanotechnology plays a crucial role within this emerging research field to combine therapy and imaging into one agent, a so-called nanoparticle. Several types of nanoparticles have been studied ranging from solid nanoparticles (magnetic, gold etc.) to polymeric structures such as liposomes[18]. Those nanoparticles can be coupled with targeting moieties like antibodies, nanobodies or small molecules [19]. Therapy can be achieved by either the properties of the core particles themselves or by linking or loading the nanoparticles with chemotherapeutic agents[20,21]. The interest in solid nanoparticles as a theranostic agent is also illustrated by several companies starting within this field (Table 1)[22]. In this work, the focus is on gold nanoparticles and their tumor targeting capabilities as a nanotheranostics agent.

1.2 Nanoparticles

A nanoparticle is defined as “a particle with all three external dimensions in the nanoscale”[23]. When one of the dimensions is greater than 100 nm, or at least significantly larger than the other two, the name nanofiber is more appropriate. Potentially, nanoparticles have applications in a wide range of fields, such as medicine engineering, energy and many more[24,25].

Within this medical field, a huge range of different nanoparticles are either studied or either currently used as a standard of care. A main division within this field of nanoparticles can be

made between organic and inorganic nanoparticles. Organic nanoparticles consist of biological molecules where the most studied ones are bilipid layered structures called micelles. Inorganic nanoparticles comprise a huge variety of nanoparticles such as quantum dots, iron oxide, silica, gold nanoparticles etc. All these types of nanoparticles have their advantages and disadvantages to use them in the medical field[26,27].

Within the field of inorganic nanoparticles, noble metal nanoparticles have fascinated scientists since long times because of their specific properties in comparison to their bulk material. A main difference between noble metal nanoparticles and the noble metal bulk material is the bright color of nanoparticles. This is the result of a plasmon absorption band, which is lacking in the bulk material[28].

1.2.1 Localized Surface Plasmon Resonance

The plasmon absorption band is seen when metal nanoparticles are exposed to light which causes the 'localized surface plasmon resonance' (LSPR) effect. Here the electromagnetic field of the light induces a resonant coherent oscillation of the free electrons of the metal conduction band (Figure 1.2). This results in a charge separation around the nanoparticle surface, perpendicular to the incoming electromagnetic field, causing a dipole moment along the axis of the electromagnetic field. When the frequency of the light is in resonance with the eigenfrequency of the electron oscillations of the nanoparticles, the amplitude of the oscillation will be maximal. This results in a strong absorption band at the 'plasmon frequency'. The decay of the surface plasmon is fast and happens radiative, by emission of a photon, and non-radiative, by the creation of electron-hole pairs. The former results in elastic/Rayleigh scattering, the latter in absorption, followed by a conversion to heat[29].

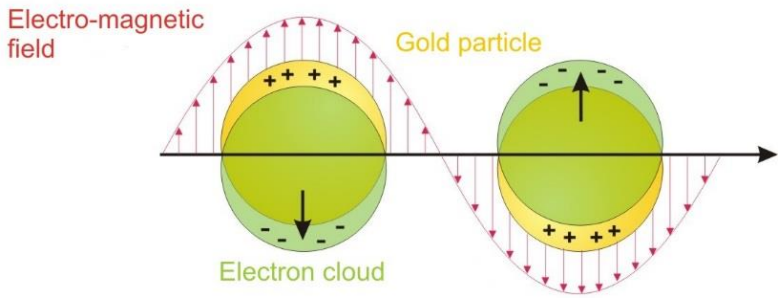

Figure 1.2. Schematic drawing of the LSPR effect.

The LSPR effect was theoretically explained by Mie in 1908 by solving the Maxwell's electromagnetic equation for the interaction of light with spherical nanoparticles[30]. For nanoparticles smaller than the wavelength of the incident light ($\lambda >> 2R < 25$ nm), only the dipole absorption of the Mie equation contributes to the extinction cross section of the nanoparticles[29]. This results in the following equation:

$$C_{ext} = \frac{24\pi^2 R^3 \varepsilon_m^{3/2}}{\lambda} \frac{\varepsilon_r}{(\varepsilon_i + 2\varepsilon_m)^2 + \varepsilon_r^2}$$

In this equation C_{ext} is the extinction cross section (nm^2), R is the radius of the metallic (nm) nanoparticle, λ is the wavelength of the incident light (nm), ε_m is the dielectric constant of the medium of the nanoparticle, ε_r and ε_i are the real and imaginary compound of the nanoparticle's dielectric function, respectively. The ε_r determines the position of the surface plasmon resonance, the ε_i the width of this band. As can be derived from the simplified Mie equation, will the absorption maximum will be attained when $\varepsilon_r = -2\ \varepsilon_m$. The real part of this equation determines the wavelength position of the resonance, the imaginary part determines the bandwidth. As a result of this, spherical golden nanoparticles display a typical absorbance band around 520 nm. The exact location of this absorbance band is dependent on multiple factors, as described below[31].

1.2.1.1 Effect of the nanoparticle material

The material effect of LSPR in the Mie function can be explained by the ($\varepsilon_r + 2\varepsilon_m$) part of the dipole approximation. Most noble metal nanoparticles (e.g. lead, mercury, tin and cadmium

nanoparticles) show an absorbance band in the UV range, and therefore do not exhibit strong color effects[32]. An exception to nanoparticles with a LSPR band in the UV-Vis range are the coinage metals: copper (Cu), silver (Ag) and gold (Au)[33]. Due to the d-d band transition, the absorbance band of these coinage metal nanoparticles is in the visible region of the spectrum. Copper nanoparticles with a diameter of 20 nm show an absorption band around 620 nm, while silver at 400 nm and gold around 520 nm, respectively. For biological studies, gold nanoparticles (AuNPs) are preferred due to ease of synthesis, higher stability, limited toxicity, and higher biocompatibility[31,34].

1.2.1.2 Effect of the nanoparticle size

The Mie equation shows only a size dependence of the extinction cross intensity but not of the plasmon resonance. However, there is still a strong size dependence on the plasmon bandwidth and position with nanoparticles smaller than the wavelength of the incoming electromagnetic wave. Supposedly, this dependence is attributed to the dielectric function, ε_m. This size-dependence is called the intrinsic size effect.

For larger nanoparticles (diameter (2R) > 25 nm), the extrinsic size effect occurs. In this case, higher order oscillations and scattering should be taken into account for solving the Mie equation. These higher order oscillations are explained by an inhomogeneous polarization of the nanoparticles when their size is comparable to the wavelength. By superposition of the dipole oscillations and higher order oscillations, such as quadrupole and octopole, a broadening of the plasmon band occurs. Furthermore, the higher order oscillations and scattering are explicitly size-dependent and therefore a red shift occurs as the particle size increases. This increase in extinction coefficients by increasing size is mainly due to the relative contribution of the scattering coefficient[31,35].

1.2.1.3 Effect of the surrounding medium

It is known that the total extinction coefficient is sensitive to the dielectric properties of the surrounding medium, explained by the ε_m factor[36]. More specific the refractive index close to the

material plays a crucial role. An increase in the refractive index will cause a red shift of the plasmon band, where a linear increase has been found for some nanoparticles with increasing refractive index.

1.2.1.4 Effect of the nanoparticle shape

The shape of the nanoparticles has a notable effect on the position of the LSPR band, even more than the material, size and surrounding medium[37]. Next to changing the position of the absorption plasmon band into the NIR region, changing the shape can also increase the cross extinction coefficient. In addition to spherical particles, rod-, shell-, cage-, cross, hollow- and star-shaped particles have been synthesized, each shape having their specific optical properties[38].

In the case of elongated nanoparticles, such as rods, the direction of the plasmon oscillation depends on the orientation of the particle axis with respect to the oscillating electric field of the incident light. This results in two plasmon bands, one for the longitudinal absorption and one for the transverse absorption (Figure 1.3)[32]. The relative position of these bands depends on the ratio of long to short axis, the so-called aspect ratio. When the aspect ratio increases, the wavelength difference between the two bands will be larger[39].

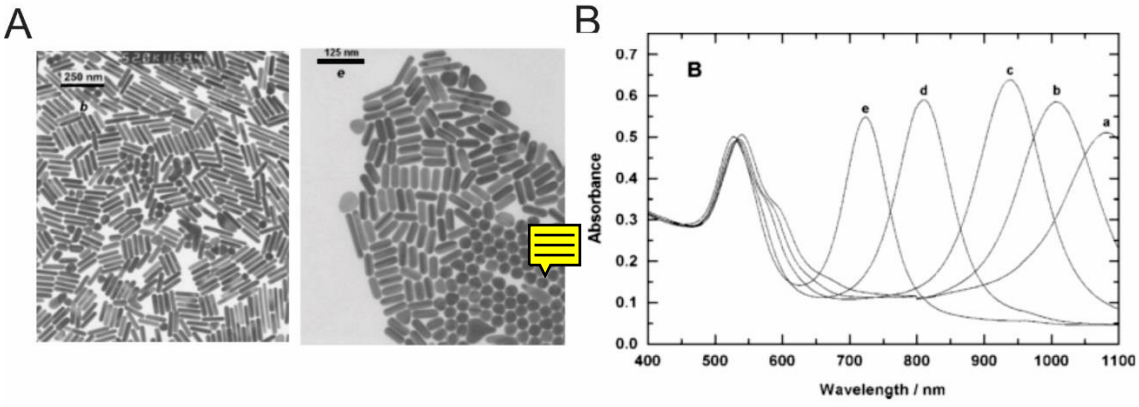

Figure 1.3. A. TEM picture of nanorods having different aspect ratio. B. LSPR spectra of nanorods with increasing aspect ratio by using lower gold seed concentration during synthesis.

Gold nanocages represent a new type of nanoparticles with a hollow interior and a thin porous wall. By changing the thickness and porosity of the walls, their absorption band can be tuned into the near infrared region (NIR; Figure 1.4). During synthesis, the basis silver cubes are replaced by hollow gold nanocages with pores. By increasing the gold concentration during synthesis, the wall thickness will increase shifting the plasmon band to longer wavelengths[40,41].

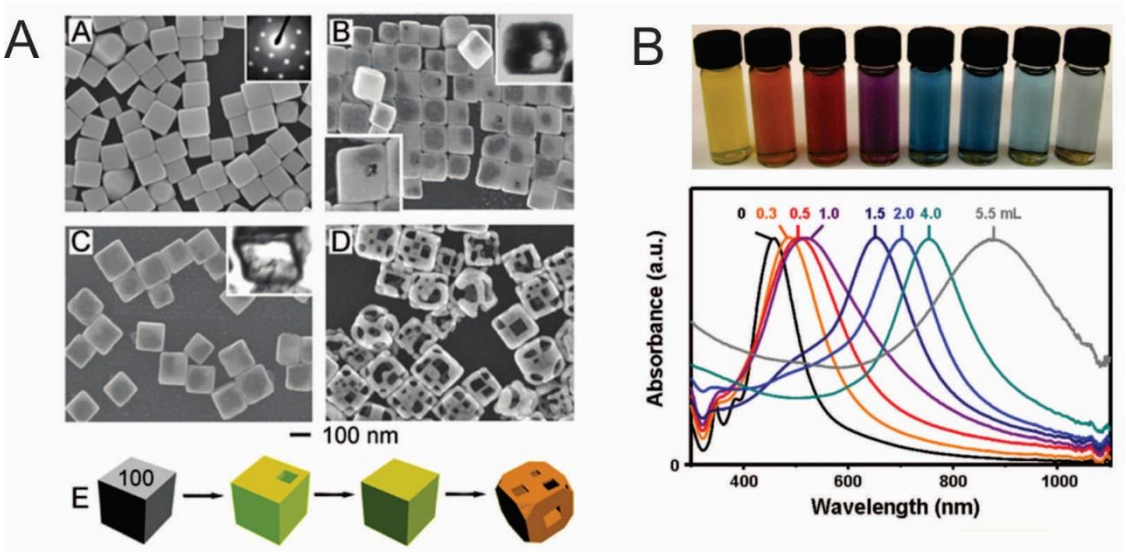

Figure 1.4. A. SEM picture of the nanocages starting from silver cubes (A) to gold nanocages (D). As inset a TEM picture where the hollow shape of the nanocages is shown. B. LSPR spectra of the nanocages after addition of different volumes of gold salt resulting in thicker gold walls. Different colors are observed for these nanocages as seen on the photograph

Also for star-shaped nanoparticles is the plasmon band red-shifted compared to spherical particles, typically resulting in a plasmon band in the near infrared region (NIR). This shift mostly results from the sharpness and length of the branches, and less from the size of the particles. When the branches increasing in length, a shift towards the NIR is measured (Figure 1.5)[42,43].

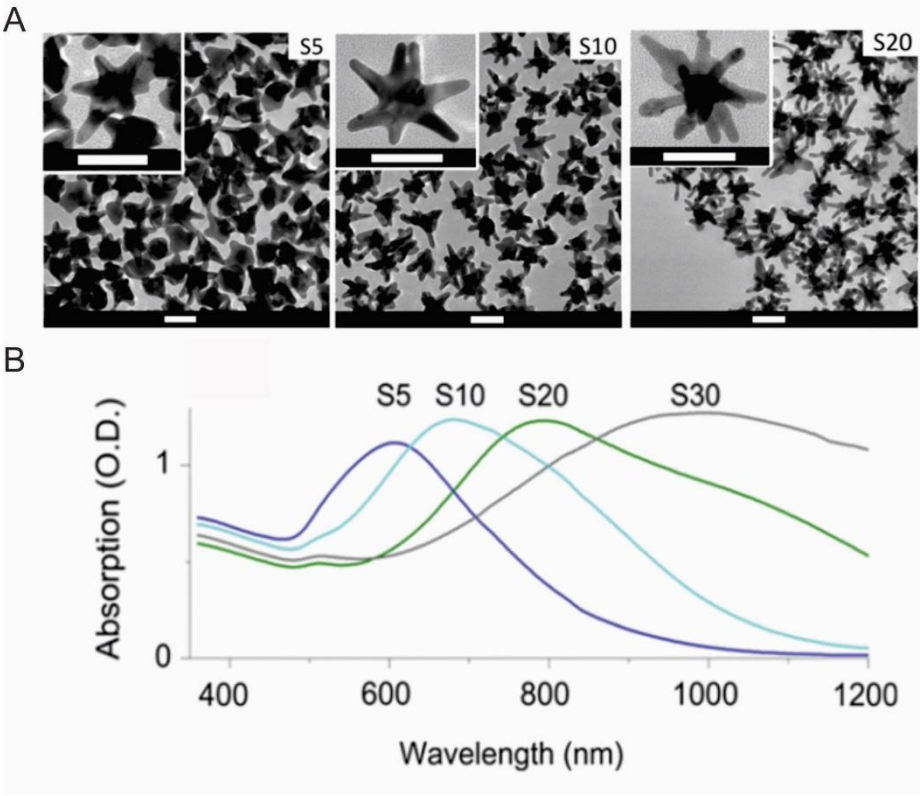

Figure 1.5. A. SEM picture of the nanostars having an increasing length of their branches. B. LSPR spectra of these nanostars having a different LSPR maximum.

1.2.2 Required properties for in vivo use

To apply these nanoparticles *in vivo* as a theranostic agent against cancers, they need to comply with a number of requirements ranging from the position of the LSPR band, size and stability in physiological conditions.

1.2.2.1 The biological window

As a first requirement, the maximum LSPR band of the gold nanoparticles must be tuned to the NIR region for maximum depth penetration. Within this region, the light can penetrate up to a few centimeters inside the human (or animal) body. This pronounced effect is caused by the lower

absorption of light by water and hemoglobin at this specific wavelength zone compared to other wavelength zones (Figure 1.6). Consequently this region is called, the biological window[44].

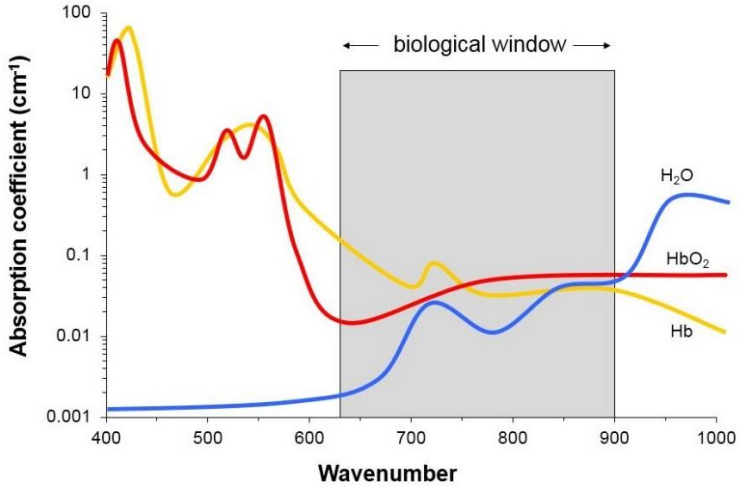

Figure 1.6. Schematic drawing of the biological window (650-900 nm) where hemoglobin and water show minimal absorption

Gold nanoparticles can be tuned to have their maximum of the LSPR band in the NIR region by changing their shape. Several special shaped gold nanoparticles have been introduced such as nanorods, nanocages, nanoshells, hollow nanospheres, nanostars etc [18].

1.2.2.2 Enhanced Permeability and Retention Effect

To deliver the nanoparticles to the therapeutic site like a tumor, the particles have to overcome biological barriers like the one between the vasculature to the interstitial space. A crucial parameter to overcome this barrier is the size of these nanoparticles, which has to be small enough to passively diffuse through the vascular pores of the tumor masses. Particles with a size between 20-600 nm have been shown to passively diffuse more easily into the tumor due to the Enhanced Permeability and Retention Effect (EPR)[45]. This effect can be explained by the leaky vasculature of the tumor compared to the healthy tissue (Figure 1.7). Due to this defective tumor vascular architecture, which results in fenestrations, there is no constant blood flow and the lymphatic drainage is inefficient which leads to enhanced retention into the tumors. This is typical for

tumors, but can also appear in several other organs, such as the sinus endothelium of the liver. Nanoparticles can accumulate inside the interstitial space by escaping the blood vessel through pores in the endothelial cell layer. This effect can be observed in almost all human cancers, with the exception of hypovascular tumors such as prostate cancer or pancreatic cancer[46]. If the nanoparticles are smaller than 20 nm, a more widespread distribution in all other organs will occur [47].

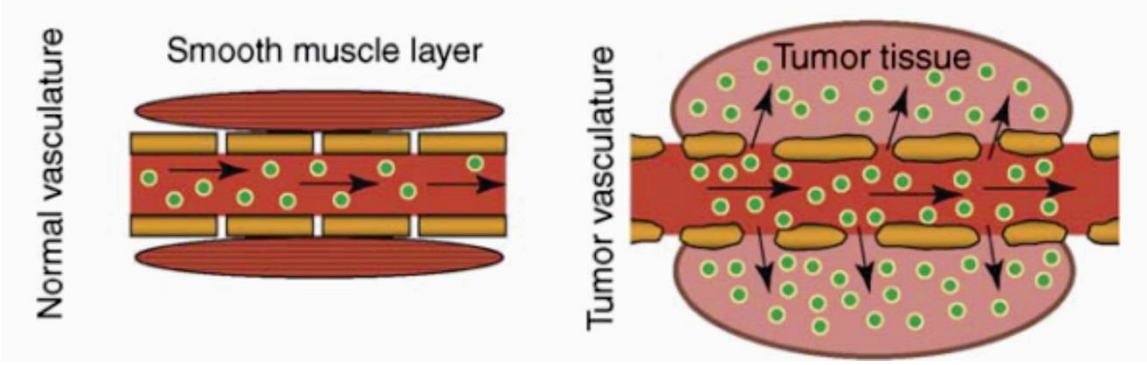

Figure 1.7. Schematic representation of the enhanced permeability and retention effect in the tumor

1.2.2.3 Retention time

The blood retention time of nanoparticles (after intravenous (i.v.) injection) is a crucial parameter for its systemic delivery. Having a long retention time will increase the possibility of the nanoparticles to accumulate inside the tumor. Several determining factors for the blood retention time have been described[48]. The first factor is that not only tumors, but also the spleen and liver are characterized by fenestrae instead of vascular tight junctions. Materials up to 600 nm can pass through these gaps, ending up in these organs. Second, the reticuloendothelial system (RES) has a crucial role to phagocyte xenobiotic materials, such as nanoparticles circulating in blood and lymphatic systems[26]. This system is composed of different cells including monocytes, reticulum cells, Kupffer cells etc. The first step in the recognition of the nanoparticles by the cells is the opsonization process[49]. Here, plasma proteins are adsorbed on the surface of the nanoparticles to facilitate phagocytosis. This phagocytosis will lead to the elimination of these nanoparticles from the blood stream.

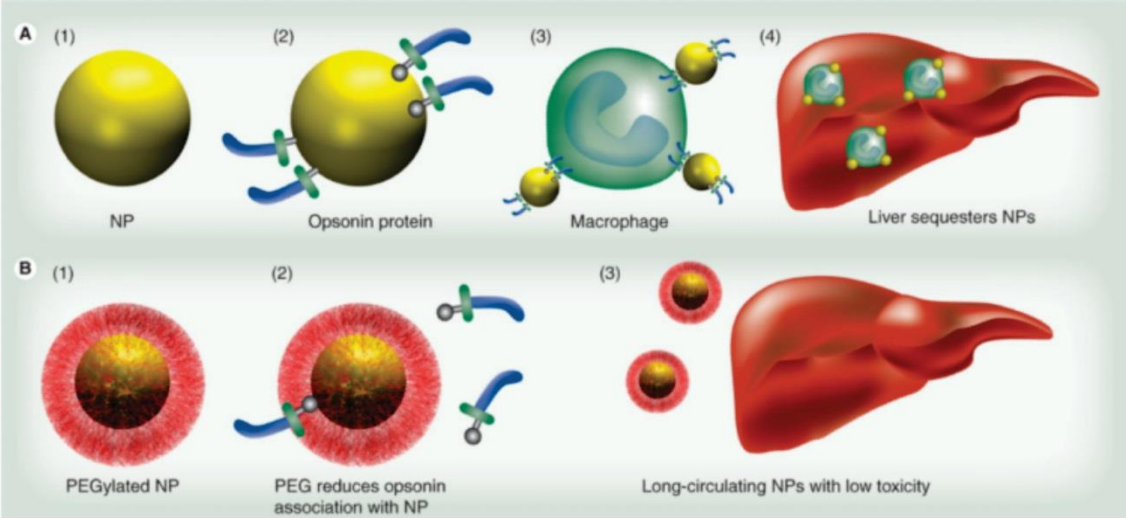

Figure 1.8. Schematic overview how polyethylene glycol prevents uptake by the RES (A) Nanoparticles (A1) are coated with opsonin proteins (A2) and associate with macrophages (A3) for transit to the liver (A4). Macrophages stationary in the liver, known as Kupffer cells, also participate in nanoparticle scavenging. (B) Nanoparticles coated with PEG coating (B1) prevents this opsonization (B2), resulting in decreased liver accumulation (B3) and increased availability of the AuNP for imaging or therapy.

For increasing the retention time, the size, coating and charge of the nanoparticles play a determining role. Within the diameter size range for nanoparticles between 40 and 600 nm, nanoparticles with larger diameters show a smaller blood retention time. Larger particles are more easily recognized by the RES, resulting in an increased uptake in liver and spleen[50]. Changing the shape compared to spherical shapes also has a profound effect on the blood retention time and organ distribution over time. For example, nanorods or discoidal shaped particles show less accumulation in liver since they avoid accumulation by non-specific cells. As a consequence, they show a longer blood-retention time which could result in a higher tumor accumulation[51,52]. By changing the coating of the nanoparticles, the opsonization process can be reduced. Nanoparticles functionalized with a hydrophilic coating such as PEG coating and a neutral charge show the least uptake by the RES system[53–55]. Neutral charges have been proven to reduce the interaction with the RES by reducing the interaction with the plasma proteins. The hydrophilic PEG layer on the other hand, improves the stability of the nanoparticles, preventing them from aggregation and interaction with the RES (Figure 1.8). Due to the PEG coating, the particles will show a longer

blood retention time. The thickness of the PEG layer is a crucial factor for diminishing the opsonization process[56].

1.2.2.4 Targeting

Having the right properties, nanoparticles can passively accumulate in the tumor by the EPR effect as described above[45,46]. Due to a longer retention time these nanoparticles have more chance to diffuse inside the tumor masses. This targeting technique is called passive targeting. The disadvantage of this targeting strategy is that nanoparticles are located in the tumor peripheum but their uptake by tumor cells will not be promoted. An alternative strategy, to enhance binding or uptake of nanoparticles by tumor cells, is to link these particles with biomolecules (peptide, antibody, aptamers etc.) recognizing over-expressed receptors on the tumor site to improve tumor targeting[19]. This active targeting may change the intratumoral accumulation of these nanoparticles, resulting in a more efficient uptake over time. Hereby, a biological ligand is chosen which targets either an over-expressed receptor on the tumor cells itself such, as HER2 or a target on the tumor vasculature, such as VEGFR. The latter has the advantage that there is no extra boundary of passive diffusion of these nanoparticles to the tumor cells. Still a debate is ongoing if active targeting will result in a more efficient targeting to the tumor or if it just has a minor effect on the intratumoral distribution of the nanoparticles[57,58].

Choosing the right biological molecule can be crucial to succeed in active targeting. Size, activity and stability are crucial parameters within this decision. Nanobodies are chosen in this thesis as the biological ligand, which is the antigen-binding region of the functional heavy-chain only antibody of camelids.

Conventional antibodies are Y-shaped and consist of two identical heavy and two identical light chains [59]. These heavy chains consist of three or four constant regions (counting from the N terminus: CH1, CH2, CH3 and possible CH4) and one variable region (VH), while the light chains have only one constant region (CL) and one variable region (VL). Disulfide bonds will link the heavy chains to each other but also each heavy chain with one light chain. The two variable domains associate and determine the antigen binding specificity [60]. Heavy-chain antibodies on the

other hand don't have these light chains, so that the antigen will be bound by only one variable domain. Thus the variable domain of these heavy chains represent the complete binding domain of the antibody and are called nanobodies (Figure 1.9)[59].

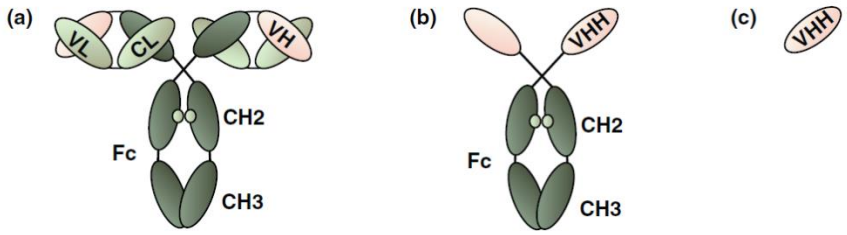

Figure 1.9 (a) Conventional antibody with two heavy and two light chains. (b) heavy-chain only antibody from a camelid that comprises only two identical heavy chains. (c) Nanobody that consists of the variable domain of one heavy chain of such a heavy chain only antibody (VHH).

The nanobodies have shown to be completely functional in antigen binding, due to small adaptation in the variable region compared to conventional variable region. These adaptations generate benefits ranging from increased stability in gastric and jejuna fluid, thermal stability, possibility of multimerization and ability to bind into clefts and cavities which can be of great therapeutic use since it can interfere with biological interactions [61].

1.2.3 Gold nanoparticle synthesis and functionalization

With these specific requirements in mind, many methods have been optimized to generate metal nanoparticles in the last decades[62]. Generally, there are two strategies to obtain these nanoparticles. Bottom-up methods where nanoparticles are produced from the reduction of ions and top-down method where material is removed from the bulk material, resulting in the desired nanoparticles[28,63]. While the latter one has minimum size limitations due to the restrictions of lithography, by using the bottom-up method all sizes and shapes could be synthesized but at rather low yield. Still, for mixing different materials on one particle the top down synthesis is preferred.

The bottom up synthesis technique for gold nanoparticles is based on the reduction of positive gold ions with chemicals in well-defined quantities and under controlled temperature and

pressure[28]. For bottom up synthesis, one can differentiate between an *in situ* (one step) and *ex situ* (multiple steps; Figure 1.10). By using the *in situ* method monolayer-forming materials are mixed with nanoparticle- forming materials to create functional nanoparticles in a single reaction. For the *ex situ* method, nanoparticles are synthesized first and in a second step monolayer-forming materials (e.g. polyethylene glycol (PEG) layer) are added to the mixture. A monolayer is then formed upon the freshly synthesized particles. The most standard *ex situ* procedure for gold nanoparticle synthesis is the citrate reduction method also named the Turkevitch method[62]. Hereby, citrate is used as the reducing agent and after proper mixing well defined spherical gold nanoparticles will be generated. The citrate will also function as a capping agent forming a well-defined layer around the nanoparticles. Nanoparticles with a different shape (such as nanorods, nanostars etc.) can only be synthesized by *ex situ* methods by adding extra capping agents as CTAB, BSPP, PVP, etc [64–66].

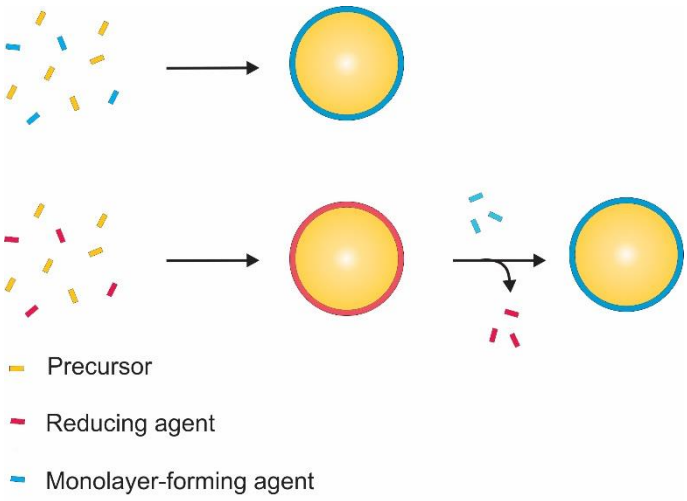

Figure 1.10. Schematic drawing of the synthesis and functionalization of AuNPs either using in situ or ex situ strategy.

The monoforming layer can range from polymers, silica to organic molecules with a thiol group, having a high affinity for gold[28]. These layers must increase the stability of the nanoparticle, which is crucial for later biomedical applications, like increasing the blood retention time. A common monoforming layer used for gold nanoparticles is the self-assembled monolayer (SAM). SAMs provide a unique opportunity to stabilize metal nanoparticles based on steric and electrostatic repulsion to prevent agglomeration[67]. SAMs will form a layer on top of the gold

nanoparticles with a charge at the end of the SAM. These SAMs must meet specific standard requirements[68]. First, the SAM molecules must form a densely ordered layer and should have high affinity for the used nanoparticles. Second, they must be suspendable in water and have the ability to increase the circulation time when used for *in vivo* purposes. Third, when used *in vivo*, one should choose a SAM with as little aspecific binding as possible. Fourth, for targeting biological molecules SAMs should have a functional chemical end group on which a biological ligand can be coupled. This is a necessity for specific coupling onto tumor cells[69].

A commonly used standard SAM molecule contains, in the following order, a thiol end group, an alkyl chain group, a polyethylene glycol (PEG), and a functional end group (Figure 1.11). The sulfur atom of the thiol molecule will bind chemically on the gold atoms of the nanoparticle. This thiol group has a higher affinity than the COOH group of the citrate capping agent and will preferentially bind to the gold nanoparticle surface[62]. The alkyl chain is the backbone of the SAM, creating an ordered monolayer through van der Waals forces between the methylene groups. This alkyl chain should preferentially be longer than 10 methylene units to efficiently stabilize the gold nanoparticles[69]. To increase the water solubility of the SAM-gold nanoparticle complex, a PEG chain is included in the long thiol molecule. Furthermore, poly-ethylene glycol (PEG) units are known to minimize the non-specific adsorption of proteins due to their hydrophilic nature, increasing the blood circulation time of nanoparticles[56]. At last, the functional end group will enable the binding with biological ligands.

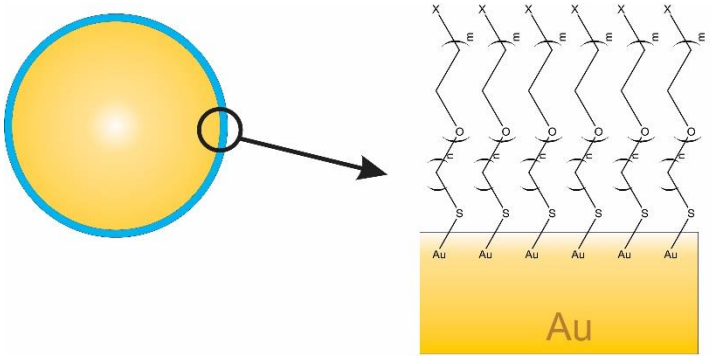

Figure 1.11. Schematic drawing of self-assembled monolayer around the AuNPs with their specific subunits.

1.3 Gold Nanoparticles as a theranostic agent

Gold nanoparticles can be used for diagnosis, assessment of particle delivery to the tumor and therapy[18]. As for diagnosis, several imaging techniques are described where gold nanoparticles can be used as an imaging technique as SERS, CT, PAI. Using these techniques, the particle delivery of the nanoparticles could be monitored which is crucial criterion in cancer research. At last these nanoparticles can be used for hyperthermia using a laser which is called photothermal therapy (PTT) but also for photodynamic therapy or drug release by hyperthermia[22].

1.3.1 Photoacoustic imaging

Photoacoustic effects are based on the thermo-elastic expansion of an agent after laser irradiation with a nanosecond pulsed laser (Figure 1.12)[70]. Due to the combination of optical and ultrasound imaging, it combines the spectral selectivity of molecular excitation by the laser with the high resolution of the ultrasound imaging[71].

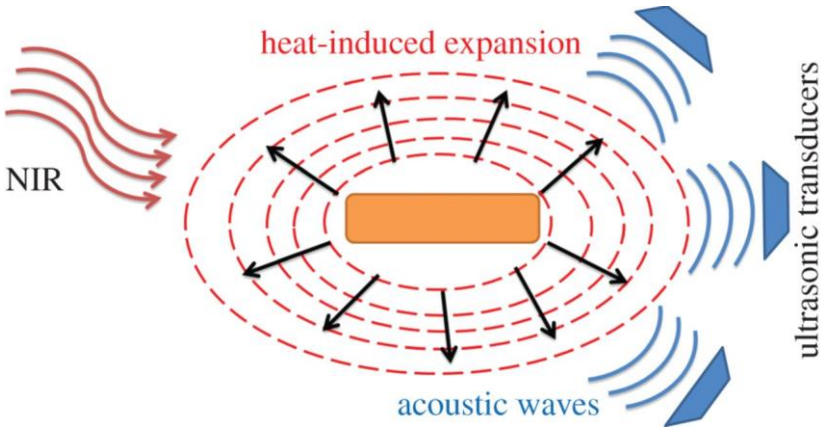

Figure 1.12. Schematic representation of PAI using gold nanoparticles as a contract agent

To generate significant PA signals, two conditions must be met, referred to as the thermal and stress confinement. First the thermal confinement defines that the pulse width of the laser light

should be shorter that the time required for diffusing the heat. Second, the time that the absorbant expands in volume must be smaller than this pulse width which is described as the stress confinement[72]. Fulfilling these two conditions, the pressure raised by the pulsed laser can be described as:

$$p_o(r) = \frac{\beta c^2}{C_p}\mu_a F = \Gamma A$$

where β is the isobaric volume expansion coefficient in K^{-1}, C_p is the specific heat in J/(K kg), μ_a is the absorption coefficient in cm^{-1}, F is the local light fluence in J/cm^2, A is the local energy deposition density in J/cm^3: $A=\mu_a F$, and Γ is referred to as the Grüneisen coefficient expressed as $\Gamma = \beta c^2/C_p$ [70].

The optical absorption needed for the pressure raise in PAI can either be performed by both internal and external contrast agents. A typical endogenous contrast agent is (oxy-) hemoglobin showing a high specific absorption spectrum in the visible-NIR region. Therefore PAI has shown to be a powerful tool for blood vessel imaging and oxygenation of the blood in preclinical and clinical applications[73]. Next to endogenous contrast agents, exogenous agents can be divided in two classes. Either nanoparticles as gold nanoparticles are used having a high absorption coefficient due to the LSPR effect or NIR organic dyes are chosen, showing lesser absorption capabilities. As a consequence, gold nanoparticles show a higher sensitivity compared to NIR dyes[74].

Since PAI is based on the optical absorption of light by the gold nanoparticles, the absorption cross section is a determining factor for photoacoustic sensitivity. A study by Hu et al compared different gold shaped nanoparticles for their absorption and scattering properties and their potential theranostic application[75]. These capabilities have been compared between nanoshells, nanorod and nanocages with their peak of the LSPR band at 800 nm. For all three nanoparticles, the absorption cross section is higher than their scattering cross section, which is crucial for PAI. The nanorods and nanocages have a much larger absorption and scattering cross section then nanoshells[75]. Another study by Van de Broek et al has proven that nanostars have even a larger absorption cross section then nanorods, which could increase the sensitivity of these nanostars as a photoacoustic contrast agent[65]. This difference in absorption cross sections is resulting in a minimum limit of detection concentration for PAI for the nanorods at 24 pM, for the nanocages

at 4.5 pM and for the nanostars at 1 pM[20,76] . Due to these low detection concentrations, these nanoparticles are introduced into the preclinical field for cancer theranostics.

Within the class of nanorods, the first proof of principle has been published in 2007 using gold nanorods as specific agent for prostate cancer, targeting HER2. With these nanorods, a first proof of principle of *in vivo* PAI is shown after implementation of a gel loaded with nanorods[77]. Li et al showed the multiplexing capability of PAI *in vitro* and *in vivo* by using two different nanorods, absorbing the light at a different wavelength (785 and 1000 nm), targeting either HER2 or EGFR[78]. This active targeting application using nanorods visualized by PAI has been confirmed by other groups[76,79]. For increasing the PA signal per particle, these nanorods can be plated with a certain thickness of a silica layer. With this layer an three-fold increase of PA signal could be achieved[80,81]. With these silica-coated nanorods, the first steps are accomplished for specific targeting of cancer cells and *in vivo* PAI using a passive targeting strategy (Figure 1.13)[82,83].

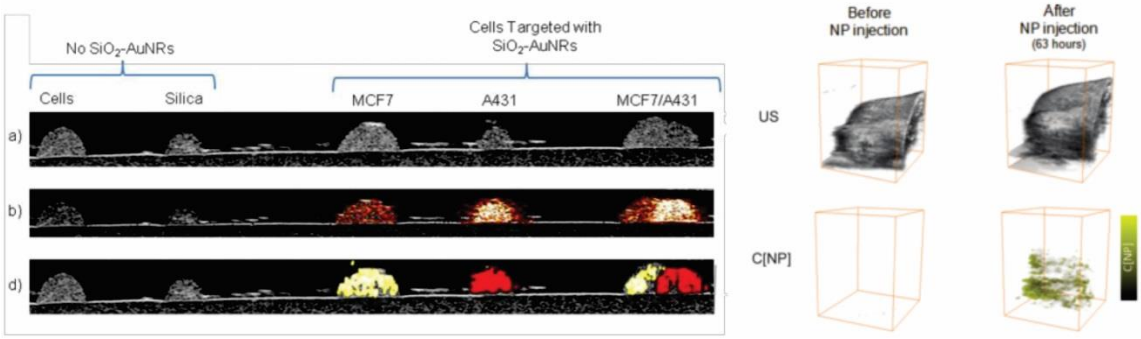

Figure 1.13. Overview of the PA main results with silica coated nanorods. Left. Active targeting of two different cell lines using silica coated nanorods either having their absorption maximum at 780 nm (yellow) or red (830 nm). On top the ultrasound picture, where in the middle the PA signal at 830 nm indicates which cell type contains silica coated nanorods. At the bottom the unmixing of both different nanorods, showing the selectivity of these nanorods for the cancer cells. Right. On top the 3D ultrasound of the tumor before and after i.v. injection of non biofunctionalized nanorods and on the bottom the PA signal, where an increase of signal is measured after nanorod injection.

Next to nanorods, both nanocages and nanostars have gained interest as a photoacoustic agent for *in vivo* cancer imaging. In 2008 Song et al. has shown the applicability of these nanocages as a photoacoustic agent for lymph node mapping on a rat model using a home-build photoacoustic

set-up[84]. Kim et al. has shown that using active targeting, PAI shows a 300 % signal increase compared to passive targeting 6h after intravenous injection of the nanocages[84]. For the nanostars, a first *in vivo* photoacoustic experiment has been performed where the accumulation of the nanostars in the lymph nodes have been mapped[85]. A recent study has shown the use PAI after active targeting of the vasculature of the tumor and the follow-up of the disrupture of this vasculature[20].

1.3.2 Surface Enhanced Raman Scattering

One of the emerging optical techniques is SERS which is based on the Raman scattering of molecules[86]. This Raman Effect describes the inelastic scattering of the light that occurs with the vibration of the molecule. This vibration results in a loss or gain of the light's energy, causing a frequency shift of the scattered light. However, this Raman Effect is exceedingly weak compared to other optical effects. For example, the Raman cross section of the molecule is around 10^{-30} and 10^{-25} cm^2, while with fluorescence the cross section is around 10^{-17} and 10^{-16} cm^2 [87].

When bringing these molecules in close contact to a gold surface, the intensity of the inelastic scattering light will be enhanced by approximately 10^{-10}-10^{-12} .This enhancement is due to two effects, namely the electromagnetic and chemical effect. The electromagnetic effect is caused by the LSPR effect of the gold nanoparticles[88]. When the ~~Raman~~ molecule is in close contact with the surface of the gold nanoparticle, they will experience the enhanced electrical field by the LSPR field. As a consequence, the incoming light and Raman scattered signal will be enhanced by the LSPR effect. This electromagnetic effect is the main contribution factor for the signal enhancement of SERS. The second effect has a more chemical origin but is still not completely understood. One of the theories is the inelastic tunneling of the excited electron from the highest occupied molecular orbital of the metal to the lowest unoccupied molecular orbital of the chemisorbed molecule[88,89]. When this electron returns to its initial state, a Raman-shifted photon is emitted.

The total SERS signal can be described by[90]:

$$P_{SERS} \sim N\, I_L\, |A(\nu_L)|^2 |A(\nu_S)|^2 \sigma_{ads}^R$$

Where N is the number of molecules involved in the SERS process I_L the excitation intensity and the effective cross section σ_{SERS}described by the two field enhancement factors for both the excitation $A(\nu_L)$ and scattered $A(\nu_S)$ enhancement and the chemical SERS effect, described by the increased Raman cross section of the adsorbed molecules as σ_{ads}^R.

Since SERS depends on the specific vibration of chemical groups in the molecule, a specific fingerprint spectrum will reflect the identity of the molecule[91]. This gives the opportunity to identify these molecules at small quantities. Hereby, several molecules have been examined for their capacity of an ideal SERS molecule fulfilling requirements such as the ability to bind on the gold surface and a high Raman cross section. As a result, up to pico- and femtomolar concentration, these Raman labeled gold nanoparticles are still detectable[76,92]. Therefore, SERS is appealing for biophysical and biomedical applications ranging from the detection of specific molecules on histological sections, pH sensing inside the cell to intraoperative imaging during surgical removal of a tumor[76,93,94].

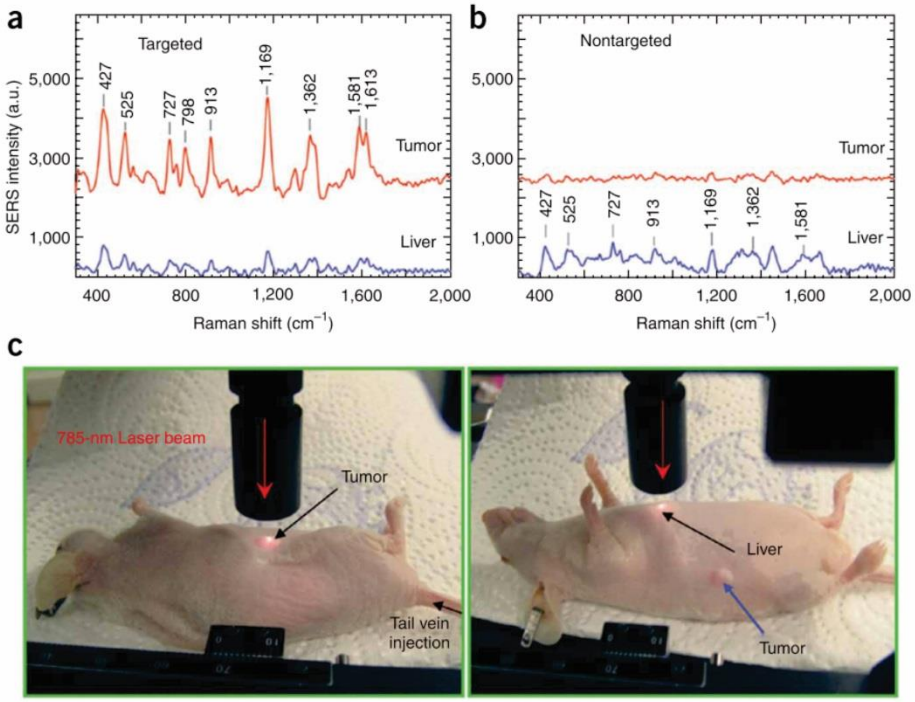

Figure 1.14. ***In vivo*** **cancer targeting and Surface Enhanced Raman detection by biofunctionalized gold nanospheres recognizging the biomarker EGFR. SERS spectra are shown for the tumor and the liver by using targeted (A) and non-targeted (B) nanospheres. C. Photographs showing the laser beam focusing on either the liver or the tumor for obtaining the SERS spectrum.**

Compared to other imaging techniques, very few examples are described on using gold nanoparticles (-sphere, rod, star) as an *in vivo* SERS diagnostic imaging agent. Qian et al showed in 2008 the first *in vivo* application of tumor SERS imaging using Raman labeled gold nanospheres by active targeting. An SERS spectrum could be deducted from the tumor site corresponding to the nanospheres inside the tumor (Figure 1.14)[95]. Next to nanospheres, nanorods have been shown as a specific SERS contrast agent for imaging a tumor overexpressing HER2 where a 30 times stronger signal is measured compared to HER2 targeting nanospheres[96]. The SERS contrast imaging capabilities using nanorods have been further examined by other groups from *in vitro* to *in vivo* [76,97]. Also the nanostars as a SERS diagnostic agent have been extensively studied by two groups led by Liz-Marzan and Von-Dinh. Due to the spikes of the nanostars, a four times higher SERS signal could be measured compared to nanospheres, where the sharpness and size of the nanostars are the crucial factors [43]. With these unique properties, SERS has been

shown as an ideal tool to image the uptake of nanostars intracellularly by passive targeting[98–101]. Still no *in vivo* data has been published of using nanostars as a SERS imaging contrast agent.

Switching over from Raman spectroscopy to 2D Raman imaging, Gambhir et al. utilized SERS as a powerful tool for intraoperative imaging using either nanorods or nanospheres. Using the high specificity of the SERS signal, the tumor border can be well defined during surgery, resulting in a more effective surgical removal of the tumor [76].

1.3.3 Computed Tomography

CT is one of the most commonly used clinical imaging modalities nowadays. This technique is based on the X-ray attenuation by different tissues, providing high-resolution images of electron dense materials such as bones and metal implants. However, it is difficult to distinguish subtle difference between soft tissues. Consequently, exogenous contrast agents are required for better delineation of the specific soft tissues using iodine or barium sulfate suspensions[102].

An X-ray image is based on the degree of the attenuation of these electromagnetic waves. This attenuation is caused by absorption or scattering of these waves by an object. The degree of X-ray attenuation is described by:

$$I = I_O e^{\Sigma_i - \mu_i x_i}$$

Where I is the intensity of the transmitted X-ray, I_O is the intensity of the incident X-ray, μ is the mass attenuation coefficient of the object, and x is the thickness of the object.

During X-ray imaging there are three types of interactions between the X-ray and the object: Compton scattering, coherent scattering and the photoelectric effect. The last effect is the dominant factor for the attenuation of the X-ray waves. Here the incident X-ray photon transfers its energy to the inner-shell electrons, resuling in ejection from the atom. The resulted vacancy of the electron (typically K or L shell) is filled by outer-shell electrons, producing characteristic X-ray photons in random directions. An important criteria is that the X-ray energy is slightly higher than the binding energy of the inner-shell electron, resulting in a higher effectiveness[102].

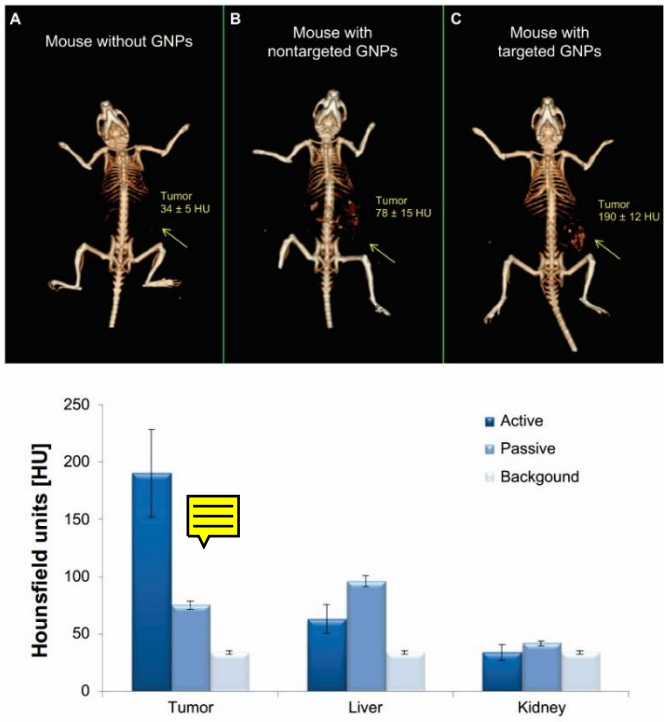

Figure 1.15. ***In vivo*** **X-ray CT of mouse before injection (A), 6 hours after injection of either untargeted nanospheres (B) or targeted nanospheres (C). The last one show clear tumor accumulation while the untargeted doesn't. CT-values are quantified for the tumor, liver and kidney confirming the CT images**

The most commonly used contrast agents for CT are iodine, barium sulfate or gold. Iodine-based contrast agents are usually suspensions of small molecules which show a high excretion by the kidney and a non-specific distribution. By coupling these molecules to polymers, micelles or liposomal contrast agents, better contrast has been obtained at specific tissues. Compared to iodine, gold nanoparticles show a 2-fold signal increase for CT[102]. This is due to the high atomic number of gold (Z=79) and the k-edge value (80,7 keV) compared to idione, which has an atomic number of Z=53 and its k-edge value is 33,2 keV. Since higher resolution is possible with X-rays at higher energy, gold nanoparticles will show a better sensitivity than iodine[103].

With this in mind, several studies have used gold nanoparticles as an effective CT contrast agent for cancer imaging. Most studies have been performed with gold nanospheres since CT contrast does not depend on the shape/ LSPR absorbance of the gold nanoparticles[104]. Using specific

targeting moieties with these nanospheres, several targets (beta4 integrin, CD4, HER2 receptor or EGFR) have been tested and imaged using CT, all demonstrating a significant CT contrast at the tumor site (Figure 1.15). Hainfeld et al[103] showed that specific targeting of HER2 results in an accumulation of the nanospheres in the tumor periphery. Hereby, specific targeting resulted in a slightly better accumulation of particles compared to passive targeting [103]. Other particle shapes such as nanorods and nanostars have been less elaborately studied in either *in vitro* proof of principle studies or in *in vivo* targeting studies[100,105–107]. Next to tumor imaging, AuNPs have been mainly used as a blood-pool contrast agent, visualizing the kidneys and liver of the mouse[108].

1.3.4 Photothermal therapy

Gold nanoparticles can efficiently turn light into heat by the LSPR effect. Since tumor cells are rapidly growing cells compared to 'healthy' cells, they are more sensitive to external factors. One of these external factors is temperature, where an increase in temperature has shown a decrease in tumor growth. Gold nanoparticles can be used as a specific therapeutic agent for PTT.

An important factor is the upper limit of temperature applied to these tumor cells. When a temperature higher than 46°C is applied, thermoablation occurs which causes necrosis, coagulation and carbonization[109]. As a side effect to necrosis, the immune system will be activated. At temperatures between 41 and 46 °C, moderate hyperthermia is applied. This is a more favorable scenario for hyperthermia since cells undergo heat stress within this temperature range and will not induce an immune reaction. It is still debated what the specific cause of this cell death after heat stress is. Hypotheses includes scenrario's of lipid melting, protein denaturation, folding and aggregation, DNA cross linking[16]. Lately, protein denaturation has been shown as the major cause for late cell apoptosis after thermal stress. Here, the protein denatures and exposes its hydrophobic groups. These groups will interact, forming protein aggregates and disturbing crucial cellular pathways such as DNA metabolism, which will result in DNA damage. Nonetheless, this effect has been seen for all cells within this temperature range at *in vitro* level[110].

The effectiveness of tumor hyperthermia is more apparent on tissue level. Tumors show an altered vascularization where tumor blood flow has been shown to be lower than healthy cells [111]. During

hyperthermia, the heat cannot be dissipated as efficient as it does from healthy tissue with regular vasculature, leading to higher temperatures reached in the tumors. Consequently tumors are more sensitive to elevated temperatures leading to an effective hyperthermia-induced ablation and therapy.

Within the field of hyperthermia treatment, several techniques have been studied ranging from magnothermia, bases on switching magnetic fields, to PTT. PTT is based on therapeutic agents that convert laser light into heat. In this field, a substantial amount of concepts have been published using different types of gold nanoparticles for either passive or active targeting. A short overview of the main nanostructures will be discussed briefly.

Nanorods have been extensively studied as photothermal therapeutic agents in the last decade due to their large absorption cross section. Dickerson et al. have performed a first *in vivo* proof of principle study using either intratumoral injection or passive targeting[112]. After exposure to the NIR laser (808 nm, 1-2 W/cm^2, 10 min), tumor growth was significantly reduced for both treated groups. Still, the intravenously injected animals showed a less effective PTT compared to the animals were particles were injected directly into the tumors due to a lower nanorod concentration inside the tumor[112]. Other groups have shown effective therapy after passive targeting, resulting in a temperature increase of up to 70 °C during laser irradiation where controls without particles only showed an increase of up to 40 °C. Even after 50 days, no tumor recurrence has been observed for these treated animals (Figure 1.16)[105]. Bioconjugated nanorods have been used extensively for *in vitro* PTT using different biological ligands and irradiation powers (28; 10; 4; 0.05 W/cm^2). The variation in laser power is due to differences in incubation time, nanorod concentration etc. Also *in vivo* active PTT has been shown using different laser powers ranging from 24 until 4 W/cm^2 showing effective tumor eradication[105,112,113].

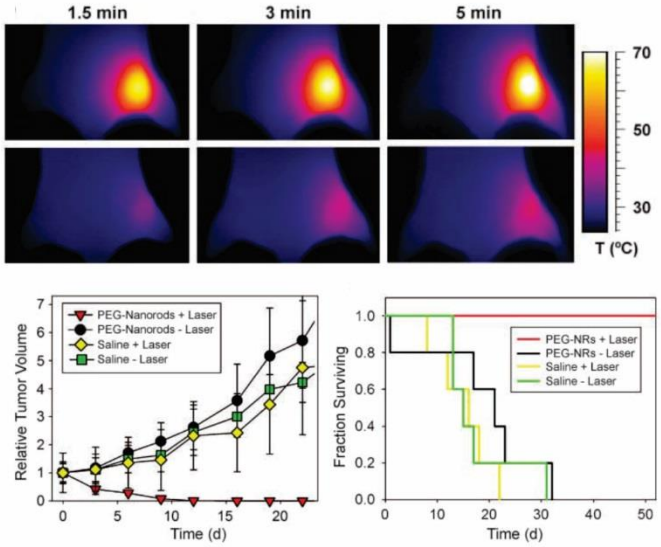

Figure 1.16. Overview of *in vivo* PTT experiments using nanorods. Top. Thermographic surveillance of photothermal heating in nanorod injected (top) and saline-injected (bottom) mice. Bottom. Volumetric changes in MDA-MB-435 tumor sizes are plotted over time after PTT irradiation (810 nm, 2 W/cm2, 5 min using nanorods after i.v. injection. On the right, the survival of mice after irradiation is plotted versus time after irradiation.

Nanocages have been described as successful photothermal therapeutic agents due to their equally large absorption cross section as nanorods[75]. Passive targeting studies show an effective treatment using a laser power of 0.7 W/cm^2 inducing a temperature increase of 14 °C. Specific targeting has been shown *in vitro* by targeting HER2 using monoclonal antibodies[114,115]. Due to the hollow shape of these nanocages, they could be combined with drug delivery which is released during PTT. As a consequence a more effective treatment is realised[41].

Also, nanostars have gained interest in the last years as a photothermal agent against cancer. Van de Broek et al. have shown, for the first time, specific *in vitro* PTT after active targeting of the nanostars using a nanobody recognizing the HER2 receptor. Using the same irradiation conditions, either non-labeled tumor cells or cells incubated with non- biofunctionalized nanostars do not show any therapeutic effects after photothermia[116]. Yuan et al. have reported the first *in vivo* PTT using nanostars with a passive targeting strategy. Using a window chamber, the nanostar accumulation around the tumor vasculature could be visualized using multiphoton microscopy.

After 48 hours, the tumor was irradiated (785 nm, 1.1 W/cm^2, 10 minutes) and localized oozing of blood could be seen due to disruption of the vasculature at the irradiation spot[117].

1.3.5 Nanotheranostics

The goal for future clinical applications in cancer treatment is to combine diagnostic and therapeutic capabilities into one gold nanoparticle. Several combinations have been studied from Raman/ PAI, fluorescence/ PAI, CT imaging/ PTT using different shapes of gold nanoparticles[80,100,105,106,118–123]. A crucial criterion within nanotheranostics is to choose the right multimodal approach with the largest benefit for cancer patients in the future. Kircher et al. demonstrates this multimodal potential by designing gold nanoparticles for combined MRI, photoacoustic and Raman imaging, where all three imaging modalities are used for a specific goal[124]. While MRI is used to locate the tumor on a whole body scale after i.v. injection of these gold nanoparticles, photoacoustic and Raman imaging are used for intraoperative guidance during surgery (Figure 1.17) Hereby PAI will guide the surgeon to locate the tumor within the tissue. Raman imaging will provide more into detail information about the finger protrusions of the tumor. This last imaging modality is crucial to decrease the likelihood of tumor reoccurrence after surgical removal [124].

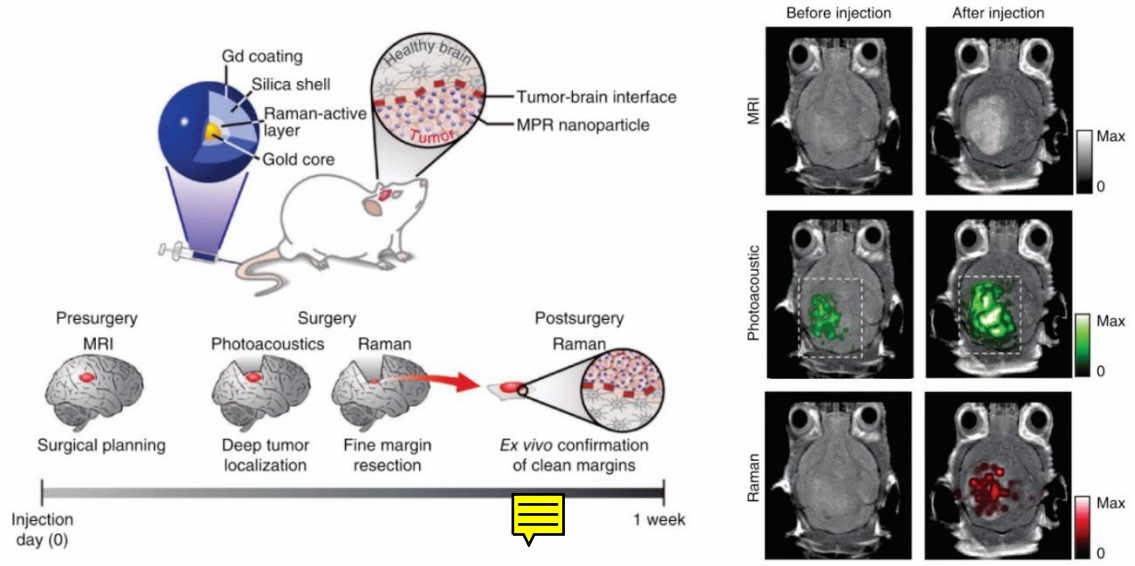

Figure 1.17. Left. The schematic drawing of the triple modality imaging concept for surgical removal of the brain tumor. Right. Two-dimensional axial MRI, photoacoustic and Raman images. The post-injection images of all three modalities showed clear tumor visualization (dashed boxes outline the imaged area)

1.4 Objectives

Nanotheranostic agents hold great potential as a new tool in the diagnosis and treatment of cancer. Several theranostic agents have been examined ranging from radioactive tracers, magnetic nanoparticles, microbubbles to gold nanoparticles[9,18]. The latter hold great promise due to their unique capabilities based on the LSPR effect of gold nanoparticles. Currently, several shapes of gold nanoparticles have been examined regarding their theranostic potential ranging from nanorods, nanoshells to nanocages. Nanostars are the least examined particles, although they have unique properties for theranostics due to their high absorption coefficient. Within this thesis, we aim to validate and improve the theranostic capabilities of the nanostars in an effective *in vivo* targeting strategy.

To be functional as theranostic agents against cancer, nanostars need to fulfill several requirements for later (pre-) clinical applications, which include their plasmon band in the NIR region, a hydrodynamic diameter below 100 nm and stable behavior under physiological conditions. To determine the ability of these nanostars as theranostic agents, both their imaging (CT; PA; SERS) and therapeutic (photothermal) capabilities must be examined in different set-ups. We have started from rather simplified settings studying the sensitivity or heat generation capacities of the nanoparticle solution to more complex arrangements *in vitro* and *in vivo*. Within these latter conditions, the stability of these nanostars in biological medium and absense to limited cytotoxicity are essential. The optimization of all imaging, hyperthermia and characterization techniques to study the theranostic potential are crucial for later targeting studies
Optimizing tumor targeting of gold nanostars

For reaching their final goal as a theranostic agent, the nanostars must be tailored to accumulate inside the tumor cells *in vivo*. Here, the efficiency of the two targeting strategies, passive and active, for the nanostars to reach a significant concentration in the tumor has been studied To achieve active targeting *in vitro*, the nanostars must be conjugated to a biological ligand. The influence of serum conditions on active targeting by the formation of a protein corona must be taken into account. Once optimized (non-) biofunctionalized nanostars are available, the *in vivo* targeting efficiency must be determined for both passive and active targeting for establishing ultimate targeting strategies. In a final phase the imaging and therapeutic capabilities of the nanostars after specific tumor targeting should be validated.
The mentioned goals, pursued during this PhD project, are presented in the following chapters.

In **Chapter 1**, general concepts of gold nanoparticles and their applications in cancer theranostics are introduced.

In **Chapter 2**, the potential of gold nanostars, synthesized in this project, as a multimodal imaging and therapeutic agent against cancer was thoroughly validated by their characterization *in vitro* and *in vivo*. The nanostar's synthesis and functionalization was optimized to fulfill the *in vivo* required properties. Having an optimal cell targeting protocol established, their photoacoustic, CT and photothermal properties were assessed.

To employ these nanostars as a theranostic agent against cancer, their targeting properties are a crucial criteria. In **chapter 3**, their optimization to successfully target tumor cells passively is reported and discussed. Active targeting is described in **chapter 4**. Both these targeting capabilities are examined *in vitro* and *in vivo* using an ovarian cancer cell line having an overexpression for the HER2 receptor. In **chapter 3**, the effect of the SAM end group on passive targeting is studied by dark-field microscopy *in vitro* and *in vivo* and by an extra quantification *in vivo* using ICP-OES. The problems encountering passive targeting are unveiled within this chapter. Targeting described in chapter 4 is based on nanostars functionalized with a nanobody to actively recognize the HER2 receptors on these tumors.

In **chapter 5**, the application of SERS-labeled nanostars as a diagnostic agent against cancer is studied. Hereby the functionalization of these nanostars with a Raman label is fully characterized using UV-Vis absorption spectroscopy, DLS and zetapotential. Based on these results, an optimal Raman label concentration is defined for sensitive detection. Contrast capabilities of the SERS-labeled nanostars are studied *in vitro* and *in vivo* using a passive targeting strategy where they tend to accumulate in the liver and tumor.

Finally, in **chapter 6**, the presented results are discussed, ultimate conclusions are drawn and suggestions for future research are made.

2 ASSESSMENT OF THE THERANOSTIC POTENTIAL OF GOLD NANOSTARS – A MULTIMODAL IMAGING AND PHOTOTHERMAL TREATMENT STUDY.

2.1 Introduction

'Nanotheranostics' – referring to the use of nanotechnology for combined imaging and treatment of diseases - is currently an active research field as combining diagnosis with therapy has several advantages. The knowledge of the biodistribution of therapeutic agents through imaging can improve the guidance and initiation of cancer therapy. This can, for example, help to decide on the best time point for applying PTT. In addition, therapy success can be assessed at earlier time points and follow-up of therapy efficiency can be improved drastically. In the clinic, this will ultimately result in earlier intervention, better patient management and improved prognosis[9]. Within the field of nanotheranostics, AuNPs that show a LSPR can have a significant impact, as the LSPR effect can be used for both imaging and therapy[31]. The LSPR effect can be explained by the collective oscillation of the conduction band electrons due to light. This collective

oscillation induces an enhanced absorption and scattering of light[27]. The scattering properties of light can be exploited by various imaging techniques including SERS[95] and darkfield microscopy[31]. The light energy that is not scattered by the particles but absorbed, is converted into heat. This specific heat generation is the basis for both PAI and PTT [3,125].

PAI is based on the acoustic waves generated by the thermo-elastic expansion that occurs when a specific compound absorbs a pulsed electromagnetic wave[72]. Exogenous contrast (e.g. carbon nanotubes, AuNPs) have shown to generate higher PAI contrast compared to endogenous molecules (e.g. hemoglobin)[75]. Due to the negligible scattering of ultrasound in tissue compared to light, a relatively high imaging depth of approximately 5 cm is possible with PAI[71]. PTT on the other hand is also based on the heat conversion of AuNPs during irradiation with a continuous laser[74]. Since cancer cells are more sensitive to heat than other cell types, a temperature increase above 43°C is lethal due to the inability to remove the heat in poorly vascularized tumor tissue[111]. For PAI and PTT, the ratio between the light scattering and absorption properties per AuNP is crucial. Hereto, several shapes of AuNPs have been studied ranging from nanorods, nanoshells, nanocages to nanostars[75]. Usually, nanostars have higher absorption *vs*. scattering coefficients compared to nanorods and nanoshells, but similar to nanocages[74,116]. This higher absorption coefficient is the crucial parameter for efficient heat conversion, important for PAI and PTT. Several studies have examined the use of gold nanorods as a contrast agent for PAI in tumors[76–79,82]. However, only non-quantitative *in vitro* data [100] and *in vivo* mapping of the lymphatic system has been shown for nanostars[85]. For PTT of tumors, several groups have reported on nanostars as an effective *in vitro* PTT agent[100,116,117] , but many questions remain regarding the PTT efficiency using these nanostars *in vivo*[21,117].

Alternatively, AuNPs can also be imaged with computed tomography (CT), since they absorb X-rays more efficiently compared to frequently used contrast agents such as iodine based compounds[105,126]. In general, heavy atoms are frequently used as a contrast agent for X-ray based CT for diagnostic imaging in the clinic and for preclinical research [105]. Nonetheless, relatively high local AuNP concentrations are needed to generate sufficient contrast for CT, in particular for small voxel sizes as required for preclinical imaging applications [127]. AuNPs, such as nanorods or spheres, have shown their effectiveness as blood-pool and tumor-targeting contrast agent using

CT [105,128]. However, for nanostars, quantitative *in vitro* and *in vivo* studies regarding their potential as contrast agents for CT are lacking[100].

Several routes have been explored to administer AuNPs as a theranostic agent against cancer, but many questions remain. Intratumoral administration is the most straight forward way for theranostic application, while i.v. injection has shown mixed results in terms of tumor accumulation[112,129]. Few reports showed reasonable tumor accumulation where the charge of the nanoparticles played a crucial role for tumor targeting[105,130]. Even functionalizing the nanoparticles with biological ligands gave different outcomes in terms of intra-tumor accumulation[57,58]. Active targeting, suggested to overcome problems with low intra-tumor accumulation after intravenous delivery, may have no influence on tumor uptake but it does affect the distribution of AuNPs within the tumor [58].

AuNPs have to fulfill some essential requirements to be applicable for *in vivo* theranostic photothermal approaches. First, the absorption band of the AuNP must be tuned to the near infrared region (NIR) frequency range for having maximal contrast generation and therapy efficiency due to its relative high depth penetration[44]. Second, the diameter of the AuNPs has to be around or below 100 nm to cross leaky blood vessels and being retained in the tumor. Third, charged particles are favored since such particles show better retention after intra-tumor injection because of immediate interaction with the tumor cells[131].

Nanostars have been defined as promising nanoparticles due to their high LSPR absorption coefficient per particle which have a significant effect on the theranostic efficiency of gold nanostars[75]. A mathematical model was developed to predict the absorption coefficient of gold nanostars[117]. The morphology of the star-shaped AuNPs can be approximated as a spherical core with several small nanorods, where these small nanorods have the highest impact on the LSPR effect. Hereby, the nanostars seem to have a higher absorption *vs*. scattering coefficient compared to nanorods and nanoshells, but similar as nanocages[65]. This higher coefficient may lead to a better heat conversion, which is important for PAI and PTT.

Given the limited data available in the literature, set out to further explore and validate the promising theranostic applications of nanostars. Exploiting the advantage of the specific high absorption capacity of nanostars, we have studied the potential of nanostars for PAI/CT and PTT *in vitro* and *in vivo*. In this study, we first optimized the synthesis and functionalization of nanostars for efficient uptake by tumor cells and assessed their PAI and PTT capabilities *in vitro* using an ovarian cancer cell line (SKOV3). For the *in vivo* validation, gold nanostars were intratumoral injected in a xenograft mouse model and their local distribution in the tumor assessed with CT and PAI. Finally, PTT was performed and its potential was evaluated using bioluminescence imaging (BLI), magnetic resonance imaging (MRI) and histology.

2.2 Materials and methods

2.2.1 Synthesis and chemical functionalization of nanostars

Gold nanostars were prepared based on the procedure described by Hao et al.[132] and further optimized by Van de Broek et al.[65]. In brief, 2 mg bis (p-sulfonatophenyl) phenylphosphine dihydrate dipotassium (BSPP; Strem Chemicals, Massachusetts, USA) and 100 µL H2O2 (30% v/v, Air Products, Vilvoorde, Belgium) were added to a 50 mL 6.8 mM aqueous sodium citrate solution (Acros Organics, Geel, Belgium). Next, 100 µL of 0.075 M $HAuCl_4$ (Acros Organics) was added slowly under constant stirring at room temperature. By using an Atlas Syringe Pump (Syrris, Ruisbroek, Belgium) a slower addition rate of 12.5 µL/min was used in comparison to previously published articles in order to achieve the desired shape and size[65]. The 50 mL AuNP suspension was centrifuged at 4500 rpm for 1 h and the pellet was re-suspended in 10 mL of water. The star-shape of the AuNPs was stabilized using a disulfide molecule, according to Lin et al.[133]. Hereby, 1 mL of an 1.2 mM disulfide $(S\text{-}(CH_2)_{11}\text{-}(O\text{-}CH_2\text{-}CH_2)_6\text{-}O\text{-}CH_2\text{-}CO\text{-}NH\text{-}(CH_2)_2\text{-maleimide})_2$ (Prochimia, Sopot, Poland) solution was added to 10 mL of the AuNP suspension mixed with 100 µL 0.5 M NaOH (Merck, Overijse, Belgium). After 90 min of shaking, the mixture was centrifuged at 4000 rpm for 60 min and re-suspended in water resulting in an optical density of ~ 1 at their maximum plasmon band. These nanostars were characterized in water and cell culture medium using UV-Vis absorption spectroscopy (Shimadzu UV-1601PC, Brussels, Belgium), dynamic light scattering (DLS; Malvern Nanosizer, WR, United Kingdom) and transmission electron microscopy (TEM; Tecnai F30, FEI company, Eindhoven, The Netherlands).

2.2.2 Dynamic light scattering and zeta protocol

For dynamic light scattering (DLS), the hydrodynamic diameters of the nanostars under investigation were measured using a Zetasizer Nano ZS90 DLS system equipped with a red (633 nm) laser and an Avalanche photodiode detector (APD) (quantum efficiency > 50% at 633 nm) (Malvern Instruments Ltd., England). A 1.5 mL semi-micro cuvette was used as sample container. The 'DTS applications 5.10' software was used to analyse the data. All sizes reported here were based on intensity average where the intensity was observed using a non-negative least squares (NNLS) analysis method. For each sample, two DLS measurements were conducted with a fixed 15 runs and each run lasts for 10 s. A detection angle of 173° was chosen for the size measurement. For determining the zeta potential an average was taken on three distinct measurements where the nanostars were dissolved in water. A U-shaped polycarbonate flow cell with embedded electrodes at either end, referred to as 'clear disposable zeta cell', was used during these measurements. As with the size experiments the 'DTS applications 5.10' software was used to process the data.

2.2.3 Transmission Electron Microscopy

We used a transmission electron microscopy (TEM) protocol as previously described134. In more detail, tumor tissue was collected after sacrificing the animals. Tissue was cut into cubes of 2mm3 and fixed overnight in 2% glutaraldehyde and 0.05 M sodium cacodylate buffer (pH 7.3) at 4°C. Tissue samples were post-fixed in 2% OsO4 in 0.05 M sodium cacodylate buffer (pH 7.3) for 1 h and stained with 2% uranyl acetate in 10% acetone for 20 min. Next, samples were dehydrated in graded concentrations of acetone and were embedded in epoxyresin (Araldite). Semi-thin slices (500 nm) were cut, stained with toluidine-blue and used for selecting regions of interest. Ultra-thin sections were mounted on 0.7% formvar coated grids, contrasted with uranyl acetate followed by lead citrate and examined with a Philips EM 208 transmission electron microscope operated at 80 kV. Digital images were taken with the MORADA 10/12 camera (Olympus, Hamburg, Germany). TEM analysis was performed with a Philips EM 208 S electron microscope (Philips, Eindhoven, The Netherlands). The microscope was provided with a Morada Soft Imaging System camera to acquire high resolution images of the evaluated samples. The images were processed digitally with the iTEM-FEI software (Olympus SIS, Münster, Germany).

2.2.4 Cell culture

SKOV3 cells (ATCC® HTB77, Cedex, France) were cultured in Roswell Park Memorial Institute medium (RPMI) 1640 medium supplemented with 10% fetal calf serum, 50 units/L penicillin, 50 µg/mL streptomycin and 2 mM L-glutamine. Cells were incubated at 37°C in a 5% CO_2 environment. All cell culture reagents were obtained from Life Technologies (Gent, Belgium). The SKOV3 cells were transduced with a lentiviral vector (LV-CMV-eGFP-T2A-fLuc) to stably express eGFP and firefly luciferase[135].

2.2.5 Inductively coupled plasma optical emission spectroscopy (ICP-OES)

For uptake confirmation, 100 000 cells per well were seeded in a 12-well plate. After 24h, nanostars ($2.3x10^{10}$ particles in 1 mL) were added to the cells and incubation continued for different time periods (1, 3, 6, 12 and 24h). Next, cells were washed with PBS and again incubated overnight with fresh medium. After trypsinization, 100 000 cells were acid-digested with kingswater (HCl/ HNO_3 at a ratio of 3:1) and diluted with de-ionized water to a volume of 10 mL for ICP-OES (3300 DV, Perkin-Elmer, Waltham, United States). Reference standards were prepared by dissolving $HAuCl_4$ to final concentrations between 0.1 and 2 ppm.

2.2.6 In vivo xenograft model and nanostar administration

Female Hsd:Athymic *Nude-Foxn1^{nu}* mice were used (8 weeks, Harlan, Horst, The Netherlands) during these experiments. All animal experiments were approved by the local animal ethics committee of the KU Leuven and were performed according to the national and European regulations. Animals were kept in individually ventilated cages with food and water *ad libitum*. A total number of 1×10^7 SKOV3 tumor cells suspended in 100 µL were injected into each hind limb of the mice and left for two weeks to grow into solid tumors[136].

After formation of tumors (size > 200 μm^3), 100 µL containing 9.2×10^{11} NPs/mL were injected into the tumor on the left hind limb. For controls, 100 µL PBS was injected into the right tumor in all animals (sham control). During all imaging experiments, tumor cell and nanostar injections, the animals were anesthetized with 1.5 % isoflurane in 100 % O_2. The body temperature and respiration rate was monitored and maintained at 37°C and 80-120 min^{-1}, respectively. For the

imaging experiments, three mice were used per condition while for the therapy experiments, six animals were used per condition.

2.2.7 Photoacoustic imaging

PAI was performed with a Vevo® Lazer 2000 (Fujifilms Visualsonics, Amsterdam, The Netherlands) using a 10 ns pulse laser (680-900 nm) with an energy fluence of 20 mJ/cm^2 and 21 MHz central frequency. These conditions were maintained for the *in vitro* and *in vivo* experiments. For *in vitro* PAI, 200 000 cells were suspended in 100 µL PBS and mixed with 100 µL warm agar (Sigma, Diegem, Belgium). This solution was added and solidified in a bigger agar block. During *in vivo* PAI, ultrasound imaging is used to determine the tumor location, after which PAI was performed to validate nanostar injection.

2.2.8 Computed tomography (CT)

In vivo and *in vitro* CT images were acquired using an *in vivo* microCT scanner (Skyscan 1076, Bruker microCT, Kontich, Belgium) with the following settings: 50 kV x-ray source, 200 µA source current, 0.5 mm Al filter, 120 ms exposure time, 22 x 29 mm field of view, 0.7° rotation step over a total angle of 180°, which results in a tomographic dataset with a 35 µm isotropic resolution. The data has been processed using software from the manufacturer (NRecon, Dataviewer, CTvox and CTan). Sample preparation was similar for CT as for PAI.

2.2.9 Photothermal therapy (PTT)

In vitro and *in vivo* PTT experiments were performed using a home-built laser setup[116]. For *in vitro* PTT, nanostars (2.3 x 10^{10} particles in 1 mL) were added to a 12-well plate containing 100 000 cells/ well that were pre-incubated overnight. The cells were then incubated with the nanostars for 24 h or with fresh medium as a control sample and washed twice with PBS. Next, the incubated cells were exposed to laser irradiation (690 nm, 20 W/cm^2, 5 min) and incubated for an additional 2 h at 37 °C. Afterwards, the cells were washed with PBS. The cell viability was assessed using a live/dead staining (Calcein AM/Hoechst; Life Technologies Europe B.V., Gent, Belgium). After staining, the cells were imaged using a fluorescence microscope with 5 x objective (CellR system, Olympus, Aartselaar, Belgium). During the *in vivo* experiments, the mice were irradiated for five minutes with a laser (λ = 690 nm; 2 W/cm^2), inducing PTT one day

after nanostar administration. During this laser treatment, the mice were anesthetized with ketamine/ domitor[137]

2.2.10 Magnetic resonance imaging (MRI)

MRI data acquisition and processing was similar to previous reports[138]. In brief, *in vivo* MRI was performed using a 9.4 T small animal MRI system (BioSpec, Bruker Biospin, Ettlingen, Germany) equipped with a gradient insert with a maximum gradient strength of 600 mT m^{-1}. A quadrature transmit-receive coil (Bruker Biospin) with an inner diameter of 7 cm was used for data acquisition. The MRI protocol included a spin echo sequence with TR = 6000 ms, TE = 15.8 ms, matrix = 200 x 200 mm, field of view 40 x 40 mm, slice thickness = 0.5 µm and 40 slices.

2.2.11 Bioluminescence imaging (BLI)

BLI experiments were performed with an IVIS 100 imaging system (Perkin Elmer, Massachusetts, United States). The mice were injected intravenously (i.v.) with D-luciferin (126 mg/kg body weight, Promega) dissolved in PBS (15 mg/kg). Afterwards, they were placed in the IVIS 100 imaging system and one image frame per second was acquired until a signal intensity plateau was reached. The following settings were used: 1 s exposure time, FOV of 10 cm, binning of 4 and an f/stop of 8. For *in vivo* quantification of fLuc reporter gene activity, the data were analyzed as photon flux per second (p/s) from an 1 cm^2 circular ROI located on the tumor using the Living Image software (version 2.50.1, Perkin Elmer). The signal intensity values at different time points (day 0, 1, 5, 8 and 15) were presented relative to the BLI signal of the same mouse at day 0.

2.2.12 Histopathology

Mice were sacrificed and transcardially perfused with 4% paraformaldehyde (PFA) in PBS 15 days after treatment. The tumors were dissected and post fixed overnight in 4% PFA. The tumor tissue was embedded in paraffin and sectioned into 5 µm slices, stained with hematoxylin and eosin (H&E) and visualized with a Mirax desk scanner (Zeiss, Jena, Germany). In addition to histopathology, TEM analysis was performed on the tumor tissue following the protocol supplied in the supplementary information of Trekker et al.[139].

2.2.13 Data analysis

For quantification of CT and PAI data, contrast to noise ratios (CNR = (SI_0-SI_1/ σ(noise)) were calculated. Statistical analyses were executed on the quantitative data using a paired t-test where the degree of significance is indicated with *: $p < 0.05$; **: $p < 0.01$; ***: $p < 0.001$.

2.3 Results

2.3.1 Synthesis and functionalization of nanostar-shaped AuNPs optimized for in vivo use

To be able to use nanostars as a theranostic agent *in vivo*, they need to be stable under physiological conditions, preferably absorb the light in the NIR-range and have a size around 100 nm for optimal retention in tumors. To meet these requirements, we optimized a two-step method of Van de Broek et al. by changing the flow rate of the $HAuCl_4$ from 50 µL/min to 12,5 µL/min during synthesis. As seen in Figure 2.1, the decrease in the flow rate shifted the LSPR band to the NIR region from an average value of 635.2 ± 5.7 nm to 665 ± 9.7 nm. Hereby no hydrodynamic diameter change of the nanostars was observed using DLS and by TEM the shape of the nanostars was visualized. However slight changes occurred at the morphology of the nanostars by using different flow rates. These images suggest that nanostars synthesized with lower flower rates of $HAuCl_4$ have less but longer branches. Nanostars synthesized at a low rate of 12,5 µL/min will be used throughout this manuscript.

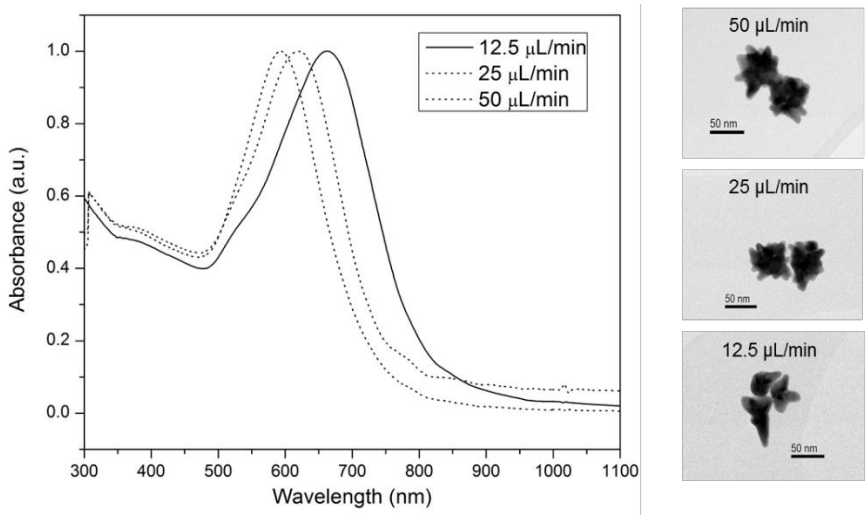

Figure 2.1. UV-Vis absorption spectroscopy of nanostars using different flow rates for $HAuCl_4$, with a shift of the LSPR band to the NIR region with lower flow rates. TEM images of the nanostars from top to bottom that were generated with flow rates of 50 µL/min, 25 µL/min and 12.5 µL/min, respectively.

These nanostars are unstable in physiological conditions, and to maintain their specific shape, they have to be functionalized with a SAM[116]. After SAM functionalization, the resulting nanostars showed a shift in their plasmon absorption band by 9.0 ± 2.5 nm (Figure 2.2). This red shift indicated a successful chemical functionalization with the disulphide, resulting from a local refractive index change due to the chemisorption of the disulphide onto the nanostars. These results were confirmed by DLS, showing an average diameter of 66.3 ± 7.8 nm for the freshly synthesized nanostars and 75.0 nm ± 5.6 nm for the SAM functionalized nanostars. After functionalization, the zeta potential was -41.3 ± 1.2 mV, indicating anionic nanostars (Figure 2.3). Incubating the nanostars in biological medium for 1 week did not show any indication for instability as confirmed by the absence of peak broadening of the LSPR band or increase in diameter of the nanostars over time (Figure 3). Still, an increase in diameter to 100.6 ± 1.8 nm was noticed immediately upon incubation of the nanostars in cell culture medium due to the formation of a protein corona. As a consequence, these optimized nanostars are suitable for *in vitro* and *in vivo* theranostic applications.

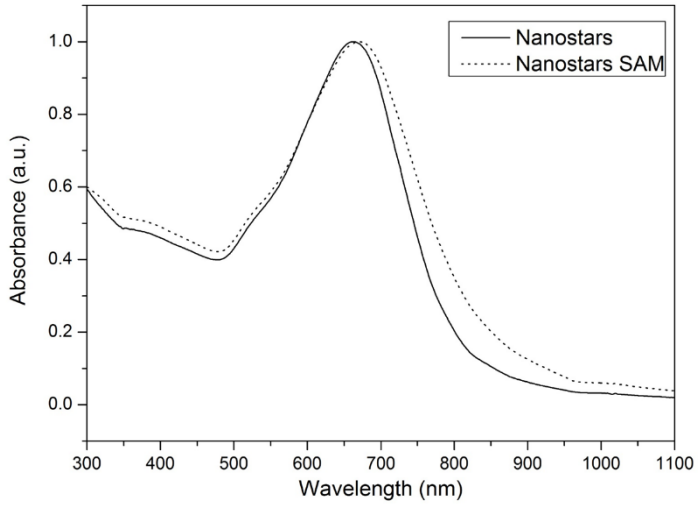

Figure 2.2. UV-Vis absorption spectroscopy of nanostars, normalized to absorbance of 1 a.u., either after synthesis (Nanostars) or after SAM functionalization (Nanostars SAM).

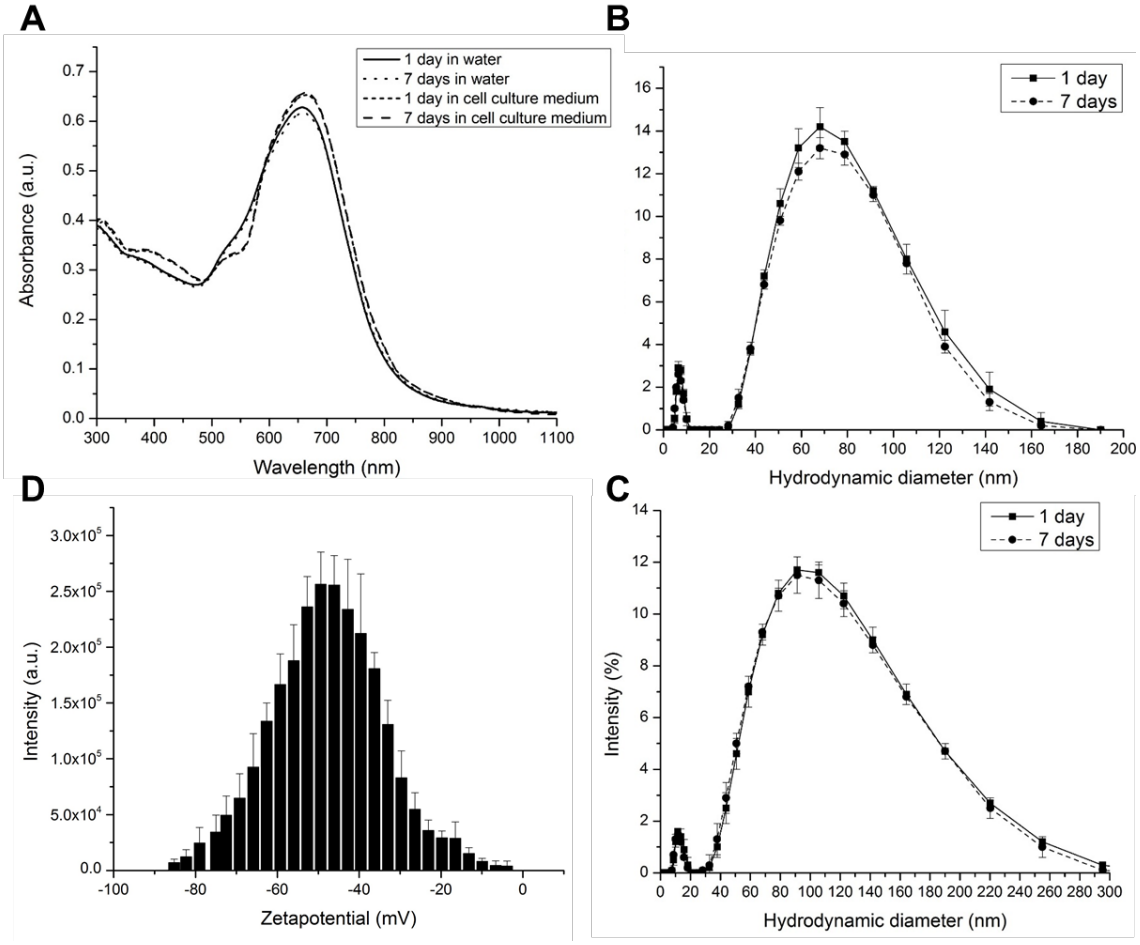

Figure 2.3. A. UV-Vis absorption spectroscopy of nanostars for 1 and 7 days in either water or cell culture medium. B. DLS intensity plots of the nanostars in water for 1 and 7 days showed no increase or decrease in diameter. C. DLS intensity plots of the nanostars in cell culture medium for 1 and 7 days. D. The zeta-potential of the nanostars functionalized with the SAM in water with an average value of -41.3 +/- 1.2 nanostars are stable in water and cell culture medium.

After functionalization, the capability of the nanostars to generate image contrast was studied in water using a concentration of 1.55 mg Au/mL. A PAI signal of 0.33 ± 0.04 a.u. was measured for the nanostars while water shows a signal of 0.13 ± 0.01 a.u. Figure 2.4). For CT, a signal of 175.67 ± 2.74 and 57.33 ± 0.17 for the nanostars and water was respectively measured. As a consequence, both imaging modalities showed almost an equal contrast to noise ratio (CNR) of 32.85 for PAI and 32.53 for CT.

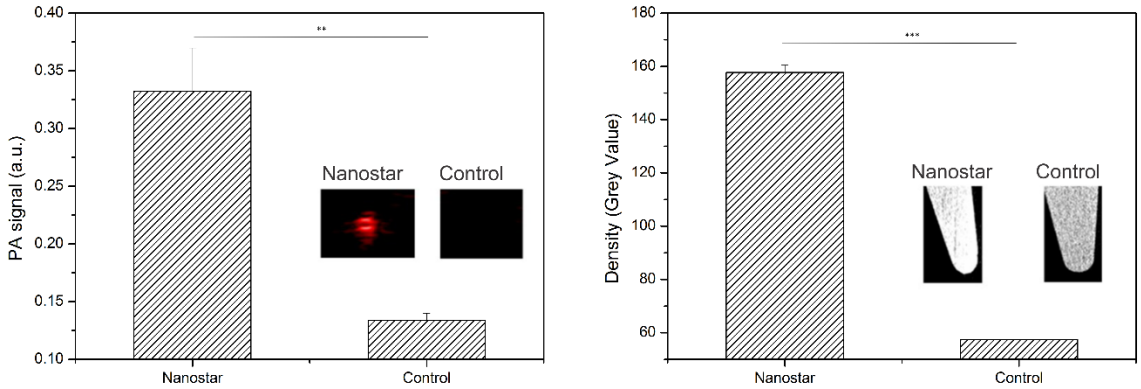

Figure 2.4 Left. PAI images of nanostars and water in tube, which were quantified by plotting the signal amplitudes. Right. CT images of micro centrifuge tubes either filled with water or nanostars suspension. The corresponding signal amplitudes were used for quantification. (n=3)

2.3.2 PAI and CT confirm efficient nanostar uptake by tumor cells

In order to test whether tumor cells efficiently take up the nanostars, SKOV3 cells were incubated for different times (1, 3, 6, 12 and 24 h) with these nanostars and the uptake of nanostars by tumor cells was examined using ICP-OES, CT and PAI. ICP-OES measurement shows for the first incubation time slots an almost linear increase of intracellular gold concentration while over time this seems to change into a plateau phase as visualized by the fitting curve (Figure 2.5). After 24h an intracellular gold concentration was measured of 11.28 ± 0.82 pg Au/cell was observed. TEM visualized the intracellular uptake of the nanostars inside vesicular structures of the cells where no nanostars were found at the cell membrane.

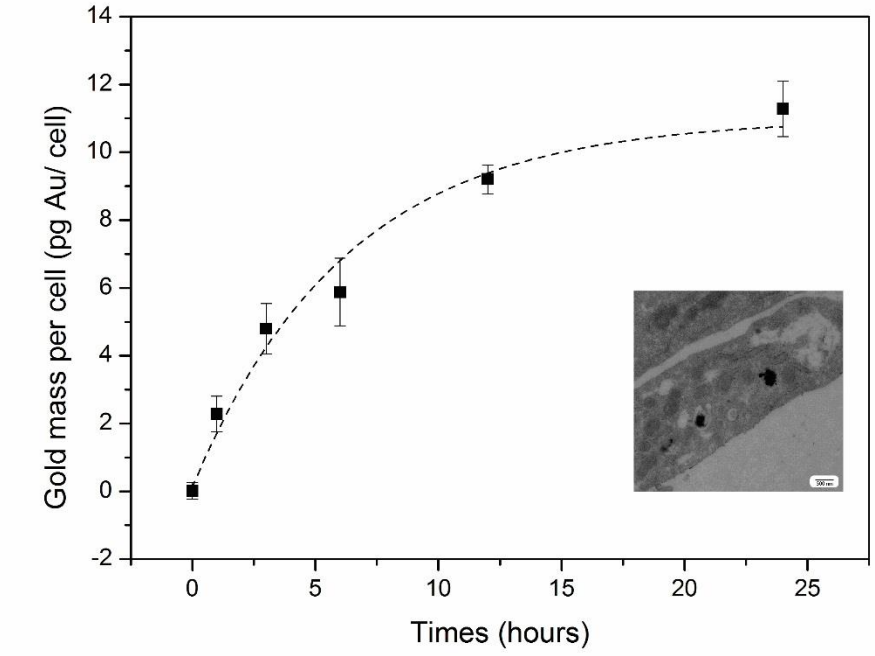

Figure 2.5. Intracellular gold concentration of different incubation time slots determined by ICP-OES. As inset a TEM images visualizing the nanostars inside the tumor cells.

We next evaluated whether this uptake was sufficiently high to follow-up by PAI and CT. Hereby the tumor cells labeled with different amount of gold nanostars were homogenously suspended in an agar phantom at 1000 cells/μL. PA images in Figure 2.6 shows the increased PA signal (red pixels) over incubation time, where an exponential correlation was found between the PA signal and intracellular gold concentration. After 24h a PAI signal 1.93 ± 0.42 a.u. was measured compared to a PA signal of 0.19 ± 0.02 a.u. for the unlabeled cells. This successful nanostars-labeling results in a CNR of 180.73 for PAI and a LOD of 3,5 pg Au/cell (17 μM).

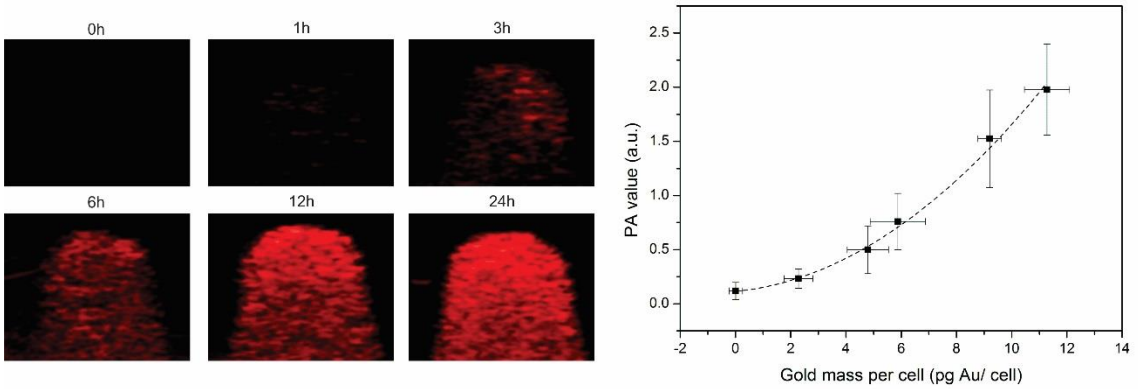

Figure 2.6 Left. PA images of a phantom loaded with tumor cells (n=3) incubated for different times with the nanostars. Right. PA signal plotted for the different gold masses per cell, where the dotted line suggests an exponential relation between those 2 variables.

For CT, the contrast visualized by grey intensity is shown in Figure 2.7 where an increase of density was noticed over time. When plotting these density values over the different intracellular gold concentrations, an exponential fit was deducted. After 24h a CT signal 161.33 ± 1.42 was measured for the 24h-labeled nanostars compared to 130.28 ± 3.25 for unlabeled cells. These CT imaging capabilities results in a CNR of 7.36 for CT and a LOD of 5.5 pg Au/cell (28 μM) .

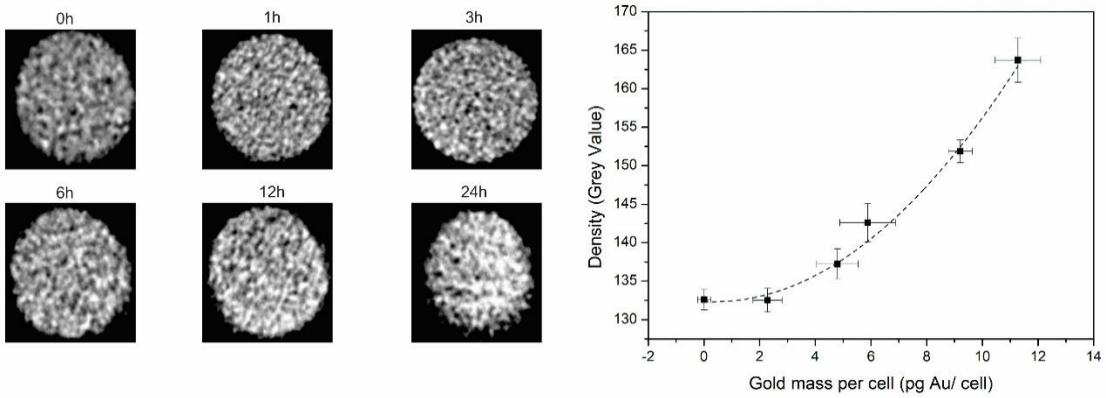

Figure 2.7 Left. CT images of a phantom loaded with tumor cells (n=3) incubated for different timeswith the nanostars. Right. CT signal quantified as density (grey values) plotted for the different gold masses per cell, where the dotted line suggests an exponential relation between those 2 variables.

2.3.3 Effective in vitro photothermal tumor cell ablation using gold nanostars

Since tumor cells were effectively labelled with nanostars, we investigate if the *in vitro* nanostar uptake in the tumor cells was sufficient to eradicate tumor cells by PTT. First, the potential of nanostars for heat generation necessary for PTT (2 W/cm^2) was measured where the temperature of the nanostars suspension increases to a plateau phase of 25°C, while no temperature increase for water was measured (Figure 2.8). Once the laser was turned off, the nanostars suspension immediately cooled down to room temperature, the same temperature as the water sample. For all next PTT experiments this same temperature profile was measured during laser irradiation.

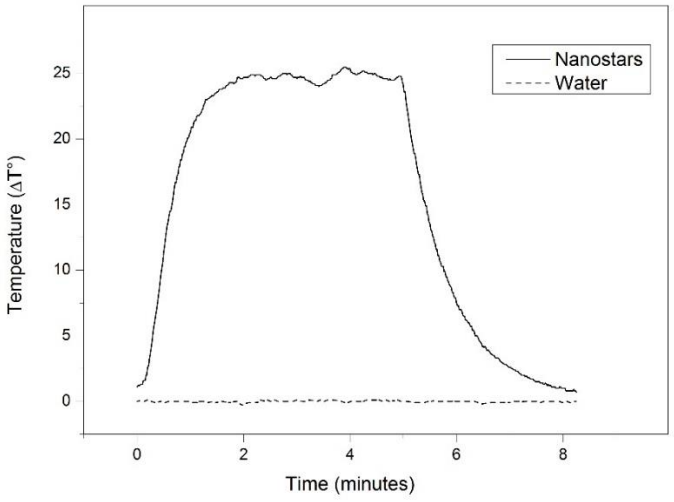

Figure 2.8 A. Temperature profile of tubes that were filled with either gold nanostars (4.6 x 10^{10} nanostars/mL) or water and were irradiated with a continuous laser (2 W/cm^2).

A crucial parameter for determining the effectiveness of PTT is to calculate the cell killing capacity (IC50 value). To determine this value, the tumor cells have been labelled with the nanostars using the same conditions as for the imaging experiments. After PTT, their cell death was visualized by calcein AM living cells staining and quantified by calculating the total green pixels. As visualized by fluorescence microscopy a radius increase of non-living cells at the laser spot indicates a higher PTT effectiveness with an increasing intracellular gold concentration (Figure 2.9). By plotting the relative green fluorescence signal compared to the fluorescence

signal of the control cells, a sigmoidal curve was fit where an IC50 of 4.8 pg Au/cell (23 μM) was calculated.

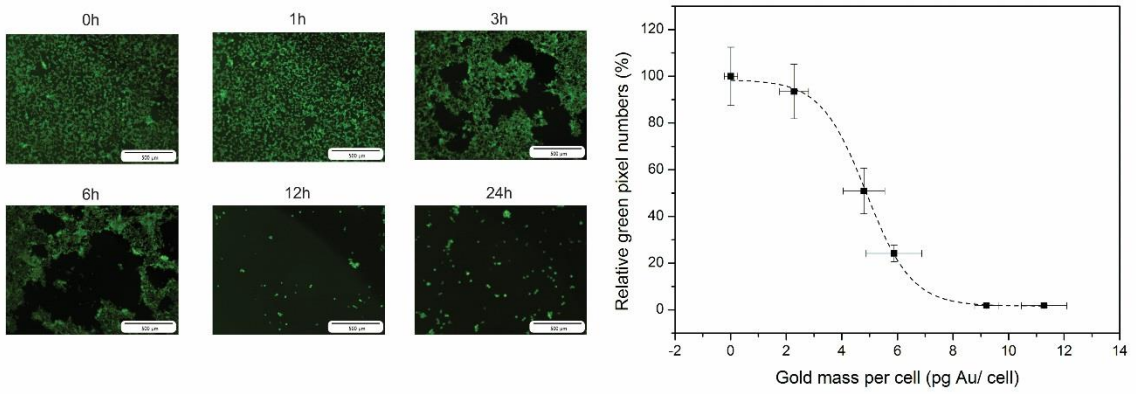

Figure 2.9 Left. Fluorescence images of the living cells stained with calcein AM for tumor cells (n=3) incubated for different times with the nanostars after PTT. Right. Relative green pixel numbers plotted for the gold mass per cell where the fluorescence signal is relatively calculated to the control sample (0h).

2.3.4 In vivo CT and PAI confirms nanostar delivery into tumors

We evaluated if nanostar injected into tumors can be visualized by *in vivo* imaging. Tumor-bearing mice (n=3) were imaged with CT and PAI before and one day after gold nanostar injection into the tumor. Before injection, only the contrast between the skeleton and the soft tissue was visible using CT (Figure 4, panel A). After injection of the nanostars, an intense contrast of 94.63 ± 6.77 was observed at the left side of the tumor, corresponding to the place of the tumor (Figure 10). No significant change in contrast was generated in the PBS-injected control tumor with a signal of 74.11 ± 1.43 (Figure 10). A CNR increase of 25.31 was calculated after intratumoral injection of gold nanostars, indicating that intratumoral delivery of nanostars can be monitored with CT *in vivo*.

Alternatively, we evaluated whether intratumoral nanostar delivery can also be followed up with PAI. Hereby, both ultrasound and photoacoustic images were overlaid as shown in Figure 2.10. Although some background photoacoustic contrast due to hemoglobin is present before nanostar injection, PAI could be used to visualize of the nanostars as indicated by the significant increase in signal intensity compared to the background (1.20 ± 0.17 a.u. compared to the control 0.44 ± 0.05 a.u.) with a CNR of 80.31.

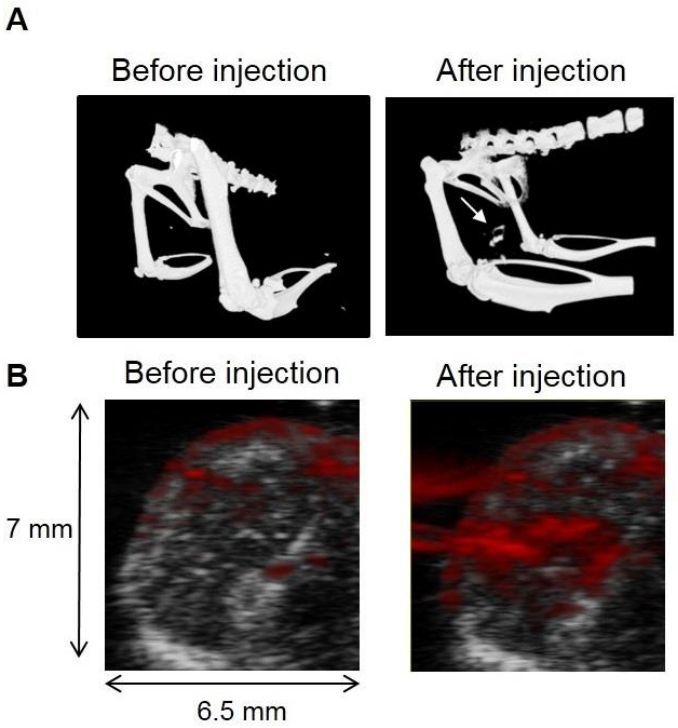

Figure 2.10 A. CT images before and after injection of nanostars into the tumor. An increased contrast is noticed at the tumor site after gold nanostars injection (arrow) B. *In vivo* PA images before and 24 h after nanostar injection. The PAI signal (red pixels) is overlaid over the anatomical ultrasound images (grey pixels).

2.3.5 Gold nanostars mediate in vivo photothermal therapy

Before executing *in vivo* photothermal treatment, some parameters have to be defined, like the laser power and the correlation of nanostar concentrations with the temperature during treatment.

As a basic rule for using laser in cancer treatment, no skin damage may occur after irradiating. The laser power may not be too strong, but still strong enough to heat the nanostars sufficiently. Changing the diameter of the irradiated surface and the optical density filter can vary the power density. Second, the tumor size must be taken into account when choosing the diameter of the laser spot. Crucially the laser spot has to cover the whole subcutaneously located tumor. Consequently by controlling these factors, the ideal power can be chosen.

To examine these factors, the laser was focused on the skin of the abdomen of a mouse which was not injected with nanostars. 18 different powers were measured using six different optical density filters (2 mm, 1.5 mm, 1 mm, 0.5 mm, 0.04 mm and no filter) in combination with three different diameters of irradiated surface (2 mm, 5 mm, 8 mm). During the 5 min irradiation, the skin temperature and the body temperature were monitored with a thermocouple and a NIR camera, respectively.

Table 2.1 Temperature difference of the irradiated skin compared to the body temperature shown for different powers and irradiation surfaces

	30 mm^2	200 mm^2	500 mm^2
7 mW	0.22	0.04	0.01
12 mW	0.38	0.06	0.02
66 mW	2.10	0.34	0.13
194 mW	6.17	1.00	0.39
540 mW	17.20	2.76	1.08
615 mW	19.58	3.14	1.22

Table 2.1 shows the maximum temperature difference between the skin at the laser spot and body temperature is shown for the different irradiation conditions. General higher temperatures were measured for higher powers and decreasing irradiation diameter. For further experiments a maximum powers must be defined where no skin damage was visible, usually around a temperature difference of 4°C. Depending on the size of the tumor no filter with a laser spot size of 0.5 cm could be used. This corresponds to a maximum power of 3.14 W/cm^2.

Besides choosing the laser power, the minimum temperature increase during treatment must be correlated to the injected nanostars concentration for later PTT after intratumoral nanostars

administration. To have an efficient treatment, a temperature difference of minimally 6°C is necessary[110].

For studying this temperature increase, different molar concentrations of nanostars were subcutaneously injected which were suspended in matrigel. By using the NIR-camera, their temperature was followed during laser irradiation for 5 minutes and 1 minute afterwards. In the meantime their body temperature was measure by a thermocouple. The highest temperature during irradiation is shown in Figure 2.11, where for all concentration a temperature increase was visualized. The relative temperatures during this measurement are visualized as a function of time where a temperature increase during the first 60 seconds was visible reaching a plateau. When the laser was switched off, the subcutaneous nanostars/matrigel cooled down to normal body temperature of the mouse. During irradiation significant temperature increase was found for the molar gold concentrations of 2.25 µM and 4.50 µM compared to the control.

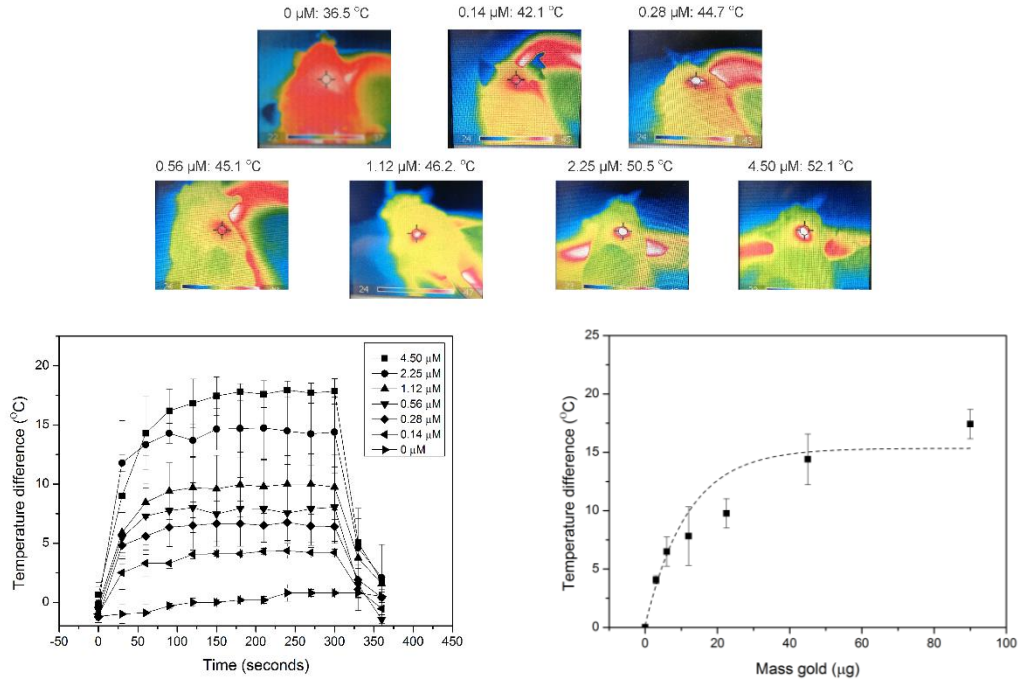

Figure 2.11 Top. NIR images of the subcutaneous injected nanostar/matrigel concentration solution for different concentrations Left. Temperature difference compared to the body temperature during PTT of different nanostars/matrigel concentration solutions. Right. The maximum temperature plotted per gold concentration where the dotted line suggest a logarithmic correlation between those two variables.

When plotting the maximum temperature by gold concentration, the temperature increase effectiveness could be deducted by using a logarithmic fit. For smaller concentrations an extensive temperature increase was noticed while for larger concentrations this reaches a plateau. As a consequence a minimum concentration of 2.25 μM is needed for later effective PTT.

The efficacy of nanostars to mediate PTT was studied in a xenograft mouse model (n = 6). The left tumor was used for injection with gold nanostars, while the right tumor acted as control after PBS sham injection. 24h after nanostar injection, both tumors were irradiated with a continuous laser (5 min, 690 nm and 2 W/cm^2). Therapy efficacy was assessed *in vivo* by using MRI and BLI to evaluate tumor regression and viability. For quantification of the tumor cell viability, the BLI signal was monitored one day before and 0, 1, 5, 8 and 15 days after PTT where day 0 is the baseline. The day before PTT and after imaging, nanostars/PBS were injected into the tumors. One day after PTT, a significant decrease in relative BLI signal intensity to 10.13 ± 1.41 % was observed for the nanostars-injected tumor compared to the tumor at day 0, indicating a decrease in viable tumor cells or vessel patency (Figure 2.12). After 5 days, an increase of the BLI signal intensity was noticed to a relative value of 45.78 ± 10.02 %, which indicates partial re-growth of the PTT treated tumor as probably not all tumor cells were photothermal ablated. Although, a significant difference in signal intensity was maintained when compared to the tumor at day 0. Additionally, the right control tumor showed a constant increase in BLI signal intensity over time until a relative BLI signal of 440.24 ± 51.14 % after 15 days, confirming that the viability of the control tumor was not affected by laser irradiation. When comparing the nanostars-injected with the control tumor, a significant difference in BLI signal intensity was detected at day 1, 5 and 8, indicating a significant effect of PTT on tumor growth.

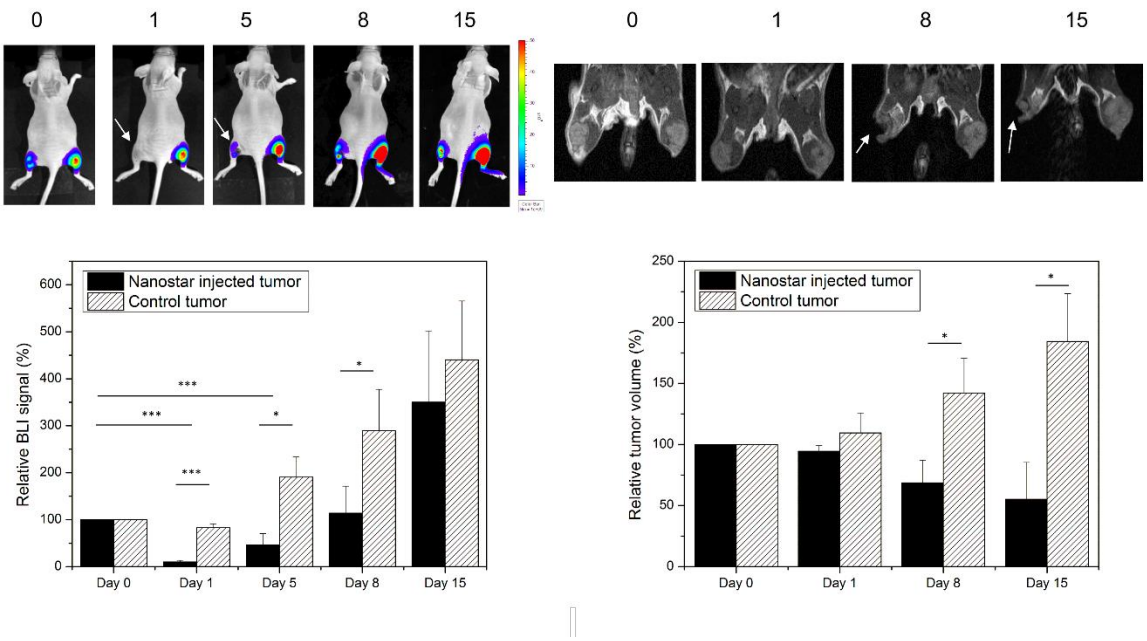

Figure 2.12 A. *In vivo* BLI before (day 0) and after PTT (days 1, 5, 8) illustrated in a color-coded intensity map. A quantification of the BLI signal intensity relative to day 0 (set at 100% per mice) is plotted for both nanostar-injected and control (PBS-injected) tumors (RT) B. MR images of the tumor-bearing hind limbs taken at corresponding time points (days) after nanostar- or PBS-injection. The yellow arrow indicates the tumor damage (hypointense area) after PTT at the nanostar-injected tumor. The relative mass volumes were quantified relative to day 0 (set at 100% per mice). (For both BLI and MRI graphs the Error bars represent SD; n = 6)

For providing more information on the therapeutic effect, MR images were acquired on day 0, 1, 8 and 15 to monitor tumor size, anatomy and heterogeneity. After 8 and 15 days, a relative tumor volume of 68.64 ± 18.45 % and 55.25 ± 30.1 % was observed for the left tumor compared to day 0, indicating effective PTT (Figure 2.12). This was confirmed by the significant difference between this volume and the volume of the control tumor (PBS injection), where a relative tumor volume of 142.27 ± 28.49 % at day 5 and 184.12 ± 39.13 % at day 8 was measured, respectively. MRI also showed that the nanostars injected tumors were not affected evenly by PTT, indicating local differences due to inhomogeneous distribution of the nanostars (Figure 2.12).

For validation, mice (n=3) were sacrificed after the first (day 1) and last (day 15) imaging time point following PTT. Tumors were resected and histologically examined. After one day, a distinct

blue color was seen on these histological slices coming from the nanostars with an LSPR band of 679 nm, which were visible in the tumor. These nanostars were only noticed in the tumor region where also necrotic cells were visible (Figure 2.13). As can be seen on the H&E stained images, the nuclei were either defragmented or darkened in comparison to the healthy cells (Figure 2.14). For the PBS-injected control tumors, the blue colour due to the nanostars was absent and the majority of cells appeared healthy. At the last imaging time point, no necrotic cells were visible on the histology sections for both the PBS- and nanostars-injected tumors (Figure 2.14).

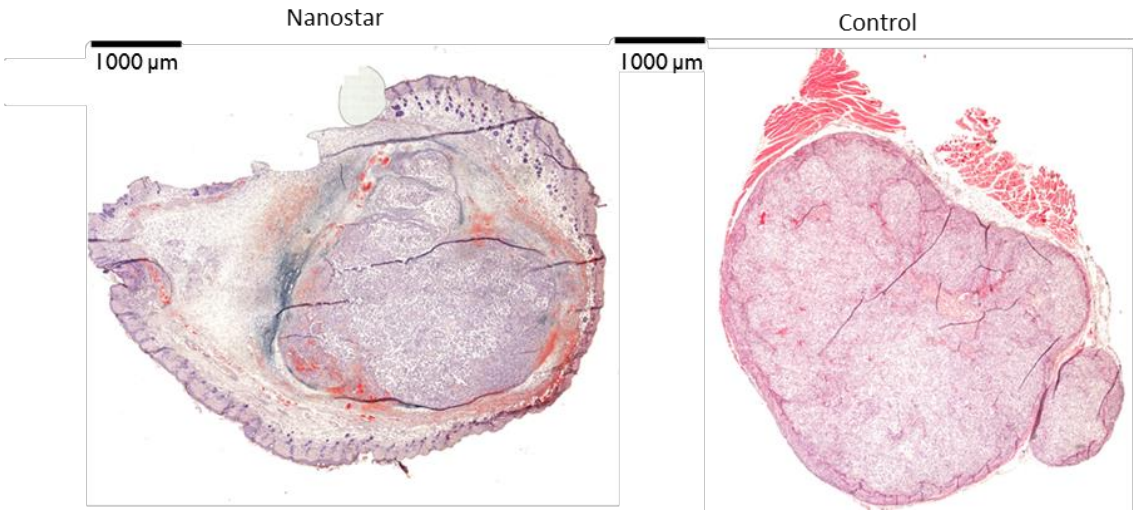

Figure 2.13 A complete overview of the histological section of either the tumor injected with nanostars (top) or PBS (bottom) after therapy. The blue 'cloud' in the tumor is caused by the gold nanostars, which is absent in the control tumor

Using TEM, the presence of nanostar clusters inside vesicles of the cells was confirmed (Figure 2.14). At the ultrastructural level, tumor cells were identified based on their pleomorphic aspects, increased nuclear/cytoplasmic ratio and distinct anaplasia. The latter was typically represented by nuclear hyperchromatism, thereby confirming that the tumor cells took up the nanostars. These nanostars were present in the cytoplasm and typically stored in membrane-bound compartments (endosomes, Figure 2.14). As the endosomes were packed with nanostars, it was difficult to identify single nanostars, demonstrating efficient intracellular uptake *in vivo* upon intratumoral injection.

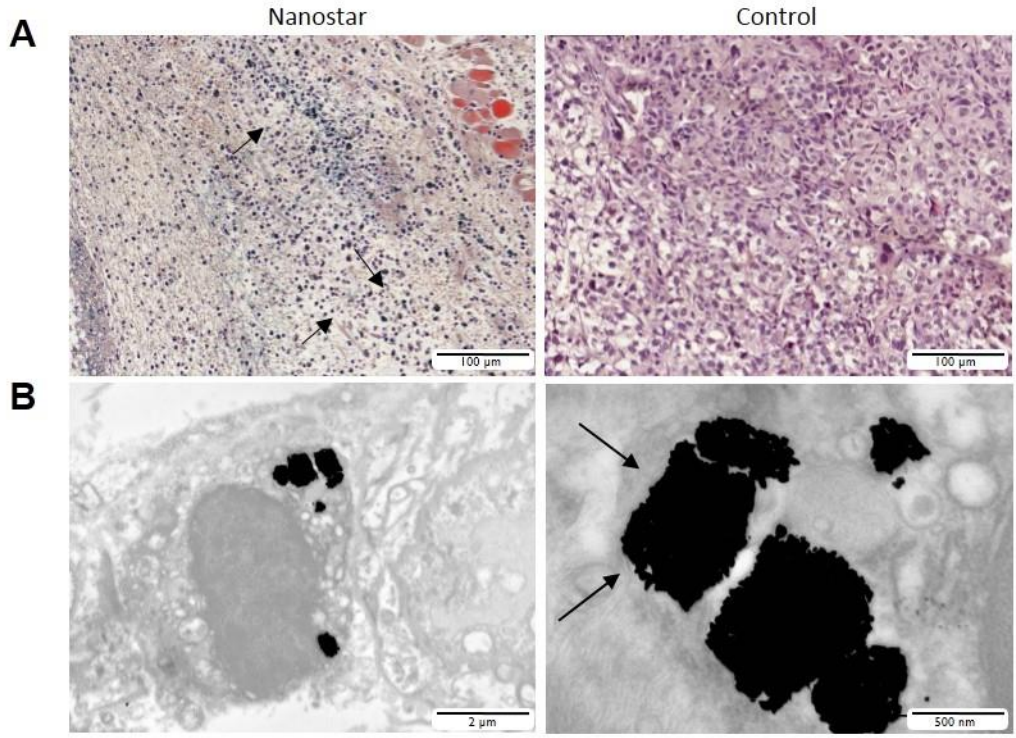

Figure 2.14 A. Bright field microscopy images of control (right) and nanostar (left) injected H&E stained tumor sections. Defragmented nuclei of the tumor cells could be visualized after therapy. B. *Ex vivo* TEM images of tumor cells that indicate the presence of nanostars clusters in endosomes. The right panel shows a zoomed section of these endosomes with vesicular structures visible around the nanostars.

2.4 Discussion

We report the use of gold nanostars as theranostic agent against cancer using their photoacoustic and CT imaging capabilities to guide PTT after intratumoral injection. This strategy has clinical potential for the ablation of superficially localized tumor masses, or to aim for complete tumor cell eradication during tumor resection surgery. The clinical potential for a similar approach was already shown using magnetic nanoparticles [109,129].

Crucial for PTT and PAI, is to synthesize nanostars with their LSPR band in the NIR-region. The aspect ratio of the tips at the nanostars plays a crucial role of LSPR band position [42]. In our synthesis set-up, a variability on the LSPR band was noticed using different gold salt flow rates.

By decreasing this flow rate of gold salt, a red shift of the LSPR band was noticed due to the formation of longer but less tips. We surmise the role of BSPP, the shape-determining detergent, in respect to the lower starting gold salt volume is the cause of these longer tips. Since tips will only grow on surfaces with poor surfactant binding as BSPP, this increase in BSPP compared to the starting gold salt volume will lead to less tips created on the nanostars. Since only the flow rate has changed and not the total volume of gold salt during, these tips could grow to longer tips. To use these nanostars for *in vivo* conditions, their nanostars shape must be maintained over time in different physiological conditions. Hereby citrate was replaced by the SAM molecule as indicated by a shift in the LSPR band due to a change in the refractive index [116], and an increase of hydrodynamic diameter due to SAM formation on the nanostars surface. With this SAM layer, the nanostars are stable in cell culture conditions due to an electrostatic and steric repulsion[24]. Moreover proteins have absorbed on the nanostars forming a protein corona which increases the stability [140].

Hereby, the efficient cellular uptake of nanostars into tumor cells is important for later *in vivo* applications. A first criterion is the size where two processes need to be considered: (1) optimal NP/cell interaction and (2) optimal tumor retention[141,142]. Nanoparticles having a hydrodynamic diameter above 100 nm are shown to have better tumor retention after intratumoral injection compared to smaller sized particles. *In vitro* studies, on the other hand, have shown that nanoparticles of around 50 nm diameter have the ideal size for cell interaction, while the cell uptake is less efficient for larger nanoparticles[141]. We have optimized our nanostars to have a hydrodynamic diameter of around 100 nm in serum conditions, which is the cut-off-value for optimal tumor retention and efficient tumor cell interaction. Second, the protrusions of the nanostars with a small curvature potentially increase cellular uptake by increasing their membrane interaction[142]. Third, our anionic particles show a much higher stability compared to cationic particles and still result in high cellular accumulation due to electrostatic interactions with the cell membrane[141]. Consequently, we were able to demonstrate that the nanostars were taken up reaching a gold concentration 11.28 ± 0.82 pg Au/cell after 24 h incubation, indicating that they are suitable for efficient passive labeling of tumor cells.

Given their right properties for cell labeling, we showed for the first time that nanostars can be used as an *in vitro* and *in vivo* theranostic agent combining both dual-modality imaging (PAI & CT) and PTT. Pure nanostar suspensions resulted in an almost equally high CNR for both imaging modalities. *In vitro* these CNR's could change since the nanostars will end up in acidic vesicles like lysosomes, where they could aggregate and may be depicted as one mass of gold nanostars. The exponential increase in signal for both PAI and CT with increasing intracellular gold concentration may be due to this aggregation. For CT this aggregation results in higher density of gold masses where the X-rays have to penetrate through, which increases the contrast. For PAI on the other hand, this aggregation results into a red shift of the LSPR band. Thereby the LSPR band will overlap more with the laser (700 nm) used for the PAI. When comparing the two imaging techniques a lower LOD and higher CNR was measured for PAI due to a higher optical sensitivity compared to CT. Still these *in vitro* experiments were performed in agar phantoms, creating a higher background for CT.

Effective PTT was possible for nanostar labeled tumor cells, whereas unlabeled cells remained unaffected by laser treatment. Hereby an IC50 of 4.8 pg Au/cell (23 μM Au) was shown, which lies between the LOD of PAI and CT. Since in a theranostic approach, the gold nanostars are first used as a diagnostic agent it is preferable that the LOD is lower than the IC50. As a consequence it shows the potential of PAI as a theranostic imaging technique compared to CT. For comparing PTT effectiveness between different nanoparticles, the irradiation power that is needed to cause cell death is used as an indicator. The radiation power of 2 W/ cm used in our study is in the same range as similar experiments performed with nanorods (10 W/cm^2)[143], nanoshells (35 W/cm^2)[13], and nanocages (5 W/cm^2)[115]. The low radiation power used for our nanostars indicates their efficacy when compared with many nanostars reported in the literature (15 W/cm , 38 W/cm and 0.2 W/cm^2)[79,111,116]. In addition to the inherent characteristics of the nanoparticles (absorption coefficient, size and wavelength), other factors like cellular labeling conditions, biofunctionalization of the AuNPs, etc. are equally important when comparing AuNPs regarding the irradiation power for PTT[142]. Consequently, there is a need for more in-depth and standardized studies for comparing different shapes of AuNPs and their theranostic potential.

In addition to the *in vitro* experiments, we evaluated the use of *in vivo* imaging modalities (CT and PAI) to monitor intra-tumor nanostar delivery and their corresponding contrast generating

capabilities. With the nanostars having the optimal dimensions for intratumoral delivery, efficient nanostar accumulation in the tumor after injection was confirmed by PAI and CT and TEM. These nanostars were densely packed in endosomes, as visualized by TEM. Looking at the contrast generation of these nanostars *in vivo*, for PAI a significantly higher CNR (80.21) was observed compared to CT (25.31). This already high sensitivity of PAI could potentially be further improved by coating the nanostars with a silica shell [81]. An additional advantage of PAI over CT is its high temporal resolution, while CT provides higher anatomical content. We were able to demonstrate that both imaging techniques can be used for intratumoral nanostar detection if high local concentrations can be achieved. By combining CT and PAI in a dual-modality approach using highly sensitive gold nanostars, PAI could provide rapid and detailed information on local nanostar distribution and their temporal changes, while CT could provide a full body scan with more detailed anatomical information.

We have also confirmed the efficiency of the nanostars for PTT. Due to their star shape, they have a high absorption coefficient resulting in a large temperature increase of 25 °C when irradiated with a laser power of only 2 W/cm^2. Reaching a local temperature higher than 43 °C will result in necrosis of tumor cells[127,144]. After determining the right laser power and gold nanostars concentration, i*n vivo* necrosis was shown in this study after tumor irradiation (2 W/cm^2), while the control tumors did not show any side effects of laser irradiation. During laser treatment a temperature increase of 15^{o}C was measured which corresponded to the gold nanostar concentration experiment. Using laser powers higher than the prescribed laser norm of 0.2 W/cm^2 defined by the American Laser Institute did not damage tissue when irradiating the control sample as confirmed by histology (Figure 6) [145]. Compared to nanoshells (4 W/cm^2) [13] and nanorods (2 W/cm^2) [112], the nanostars require the same magnitude of laser power to induce ablation after intratumoral injection. However, comparisons between different nanoparticles to assess their therapeutic efficiency are difficult due to the different experimental condition. Hereby, the combination with imaging techniques that provide information on the nanostar distribution and therapy outcome is of utmost importance. Additional treatment options to improve outcome are a combination of PTT with chemotherapy, photodynamic therapy or the introduction of tumor-targeting moieties to the nanostars[17,146].

2.5 Conclusion

We have demonstrated an optimized synthesis and use of nanostars as a theranostic agent for combined multimodal imaging using CT, PAI and PTT. Due to the red shift of the LSPR band and the high absorption coefficient, these nanostars could have a better theranostic outcome compared to other shaped nanoparticles. The gold nanostars created significant contrast in both CT and PAI and proved to be an effective therapeutic agent for PTT, due to a successful passive uptake by the tumor cells. Future work should focus on the intravenous delivery of gold nanostars (passively or actively) leading most likely to further improvements in the nanotheranostics field, aiming for imaging and therapy of specific tumor types, which has also the potential to target and treat tumor metastases

3 UNREVEALING THE REASONS FOR THE INEFFECTIVENESS OF PASSIVE TARGETING USING NANOSTARS.

3.1 INTRODUCTION

In the previous chapter, the potential of the nanostars was studied using an intratumoral injection approach. To enable more practical clinical applications, e.g. for diagnosing the tumor, the nanostars must accumulate inside the tumor after systemic administration. These particles spreading through the whole body via the bloodstream can either actively target the tumor or passively enter it by the specific characteristics of the tumor. Within this chapter the passive targeting will be studied *in vitro* and *in vivo*.

A crucial factor is the optimization of the nanoparticle-cell interaction where the nanoparticles tend to enter the tumor cells. Generally nanoparticles uptake inside the cell is facilitated by a clathrin mechanism[147]. More specific, when NPs approach the cell surface and bind to the cell surface by ligand-receptor interaction, clathrin molecules intracellular will facilitate the NP uptake by inducing invagination of the membrane. These nanoparticles end up in endosomal structures within the cell, which will fuse with lysosomes to degrade the nanoparticles or excrete them by exocytosis[148].

Different factors may influence the nanoparticles uptake such as size, shape and charge[141]. regarding size it has been shown that spherical nanoparticles around 50 nm are favored in terms of uptake compared to larger or smaller nanoparticles[149]. The exact reason is still not clear but it is suggested that the number of contact sites between the membrane and the nanoparticle play a crucial role for cellular uptake ref. It will take longer for the cell membrane to wrap a large particle and finally internalize it. Small particles below 50 nm however will form clusters that favor uptake[142]. Another factor is the charge of the nanoparticles, where cationic nanoparticles show a better intercellular uptake *in vitro* due to the electrostatic interaction with the negatively charged cell membrane. As a result, anionic nanoparticles are less taken up by these tumor cells. However some groups claim that they interact with the few cationic places on the cell membrane[150]. A last aspect is the shape of the nanoparticles where an increase in roughness already increases intracellular uptake[151]. For more atypical shapes it was suggested that rod like structures will experience longer wrapping times since the cells have to induce a bigger engulfment. On the contrary, *in vitro* experiments show a higher uptake of these rod-like structures favoring engulfment[152].

Nanoparticles can be used to target the tumor after i.v. injection using a passive targeting strategy. Here, the nanoparticles will accumulate inside the tumor due to the EPR effect where the tumor vasculature is more leaking, favoring diffusion of these nanoparticles inside the tissue (enhanced permeability). Hereby the particles should have a diameter between 40-600 nm to diffuse through the tumor's pores. When these nanoparticles diffuses inside the tumor tissue, they will have a low probability to circulate back into the blood mainly due to a defective lymphatic system[45,153] (enhanced retention). This EPR effect is dependent on either the tumor biology such as the vasculature and tumor extravascular environment and on the nanoparticles properties.

As with the *in vitro* nanoparticle-cell interaction the same aspects (size, charge and shape of the particles) play an essential role for the intratumoral accumulation and distribution[19]. Here, the diameter of the nanoparticles needs to be smaller than the cut-off size of the fenestrations in order to be able to diffuse inside the tumor. Moreover, this size will also affect the extravasation of the nanoparticles within the tumor. On average, nanoparticles with a size smaller than 50 nm show a preferential accumulation inside the tumor, and the smaller the better the extravasation in the tumor[154,155]. Still, if the particles are too small, they show a more wide spread distribution in

different organs, increasing possible toxicity[47]. Also the presence of a charge on the nanoparticles has a profound effect on the nanoparticle accumulation in the tumor. Overall, neutral nanoparticles will show better accumulation within the tumor compared to charged nanoparticles[53]. However, in literature mixed results are shown with these charged nanoparticles where some have seen tumor accumulation with charged nanoparticles where others did not[,156,157]. In general, cationic particles show the least accumulation in the tumor. Hereby the effect of the charge on the blood retention time must be taken into account[19]. As for tumor cells, charges will increase the recognition by the RES, decreasing the blood retention time. As a last factor the shape of the nanoparticles may play a crucial role. Discoidal elongated shapes will show a higher accumulation in the tumor with a high penetration within the tumor compared to spherical particles with the same size[51].

Due to these specific and complex interactions of nanomaterials with living organisms, differences in efficacy of passive targeting have been shown the last years. While some observed reasonable accumulation in the tumor[58,154,158], others reported almost no accumulation within the tumors[95]. When nanoparticles accumulate inside the tumor, most of them are found in the tumor peripheries[103] and could be used for theranostic purposes[20].
In this part of the study, the passive interaction of the nanostars with the tumor cells will be studied *in vitro* and *in vivo*. Nanostars with a different end group on their self-assembled monolayer (SAM) will be evaluated regarding the difference in their cellular uptake. The biodistribution after i.v. injection of both nanostars with a high and low *in vitro* cellular uptake will be examined for different organs. As a final step, the photothermal capacities of these nanostars will be tested after i.v. injection.

3.2 MATERIALS & METHODS

3.2.1 Nanostars synthesis and functionalization

Nanostars synthesis and chemical functionalization have been executed as explained in chapter 2. For the functionalization three different molecules have been used ‘SAM MAL’ ((HS–

$(CH_2)_{11}$–(O–CH_2–CH_2)$_6$–O–CH_2–MAL)$_2$, 'SAM MALOH' (HO-CH_2–O-(O–CH_2–CH_2)$_6$–$(CH_2)_{11}$–S-S–$(CH_2)_{11}$–(O–CH_2–CH_2)$_6$–O–CH_2–MAL) and 'SAM COOH' (HS–$(CH_2)_{11}$–(O–CH_2–CH_2)$_6$–O–CH_2–MAL). After functionalization, the nanostars were characterized using UV-Vis absorption spectroscopy, DLS and zetapotential, in either water or cell culture medium with serum.

3.2.2 Darkfield microscopy analysis of cell/ nanostar interaction.

As in chapter 2, tumor cells (SKOV3) were seeded by 150 000 cells per well in a 12-well plate to study the cell-nanostars interaction. After 24h, nanostars with different SAMs ($2.3x10^{10}$ particles in 1 mL) were added to the cells and incubated for 24h. After washing with PBS, these cells were again incubated overnight with fresh medium. After trypsinization, 300 µL of the cell suspension were plated on a coverslip in 1mL of fresh medium in a 12 well plate and incubated overnight. After fixation with 4-paraformaldehyde (4% PFA), these coverslips were mounted on a glass slide and visualized with darkfield microscopy. Darkfield microscopy images were quantified by using CoralPaint Software where yellow pixels (nanostars) and green pixels (tumor cells) were detected from the images and converted into white pixels. The amount of white pixels was calculated for both conditions where afterwards the amount of nanostars pixels was divided by the amount of cell pixels to result in the nanostars/cell mean signal density.

3.2.3 In vivo biodistribution using ICP-OES and darkfield microscopy.

Athymic nude mice were, as in chapter 2, inoculated with tumor cells to let a tumor grow for 2-3 weeks. Afterwards PBS or the nanostars (2,3 mg Au /ml) were injected via the tail vein (n=4 for each condition). After 1 or 24h the mice were perfused with 4-PFA and the heart, the liver, the spleen, the kidneys and the tumors were dissected and stored in PBS with 0,1% sodiumazide (Sigma). For ICP-OES, the organs were homogenized (Omni International Tm 125-220) in 1 ml distilled water. At each sample, 3 ml HCl and 1ml HNO_3 were added. These samples were shaken for at least 48h. Afterwards, the samples were filtered using a 0.2 µm acrodisc syringe filter with HT tuffryn membrane (PALL Life Sciences) before measurement of the Au-content using ICP-OES. For these measurements, standard Au Bibliography were used ranging from 1 – 100 ppm.

For darkfield microscopy and histology, the dissected organs were embedded in paraffin to make sections of 7 mm thickness with a microtome (HM360, Prosan). The sections were placed on microscope slides and deparaffinized for the darkfield microscopy slices and H&E staining.

3.2.4 In vivo photothermal treatment and evaluation with BLI and MRI

One day after nanostar injection, the tumors were all irradiated during five minutes with a monochrome NIR laser (λ = 690 nm; 1.00 W/ cm^2) using a home-build laser setup, as described in chapter 1. To visualize the tumor viability and size evolution, BLI and MRI (protocol see chapter 1) were performed before treatment and three times a week until 12 days after irradiation.

3.3 RESULTS

3.3.1 SAM functionalization and characterization

Nanostars were synthesized and functionalized as described in chapter 1 with a SAM molecule, either an alkanethiol or disulfide, all having a different end group. The alkanethiol is modified with a carboxyl end group (SAM COOH) while the disulfide is composed of either 50/50 maleimide hydroxide (SAM MALOH) or complete maleimide (SAM MAL). This functionalization was thoroughly characterized and summarized in Table 3.1. For all three SAM molecules used, a red shift of the LSPR band and an increase in hydrodynamic diameter was observed, confirming the successful functionalization. After functionalization a small difference in zetapotential is measured where the nanostars SAM COOH have a slightly more negative zetapotential compared to the nanostars SAM MAL and SAM MALOH. When incubating these nanostars in serum conditions, an increase of the hydrodynamic diameter is measured of 21.2 +/- 5.2 nm for the nanostars SAM MAL, 13.1 +/- 2.1 nm for the nanostars SAM MALOH and 4.5 +/- 3.6 nm for the nanostars SAM COOH.

Table 3.1. LSPR shift, hydrodynamic diameter shift, zetapotential and protein corona increase for three different functionalization of the nanostars either, with SAM MAL, SAM MALOH or SAM COOH. Data represents mean values and standard deviations of 3 independent experiments.

	SAM MAL	SAM MALOH	SAM COOH
LSPR shift (nm)	9.4 ± 2.6	8.6 ± 3.5	9.6 ± 2.6
Hyrdrodynamic diameter shift (nm)	7.8 ± 3.4	7.5 ± 1.3	8.6 ± 2.9
Zetapotential (-eV)	41.3 ± 1.2	36.1 ± 1.9	44.5 ± 3.6
Protein corona increase (nm)	21.2 ± 5.2	13.1 ± 2.1	4.5 ± 3.6

3.3.2 Difference in cellular uptake by changing the end group of the SAM.

To study and compare the intracellular uptake of the nanostars by the tumor cells, we used darkfield microscopy to compare the difference in uptake over time. As for the MAL and MALOH SAM functionalized nanostars a gradual intracellular uptake over time was, resulting in fully packed tumor cells after 24h. Between the cells no nanostars were found indicating efficient intracellular uptake of these nanostars. On the contrary, we observed almost no accumulation over time for the COOH SAM modified nanostars even after 1h incubation[1]. An indication of the amount of nanostars per cell was deducted by calculating the nanostars/cell density using darkfield microscopy. Here the same trend was observed where no difference was quantified for the cellular uptake of the nanostars SAM MAL and SAM MALOH up to a nanostar/cell mean signal intensity of 15.69 ± 1.27 % after 24h for the nanostar SAM MAL and 18.93 ± 5.18 % for the nanostar SAM MALOH while only a value of 1.54 ± 0.99 % was deducted for the nanostar SAM COOH. As a consequence a significant difference in uptake could be confirmed between the nanostars SAM MAL(OH) and nanostars SAM COOH using a two way repeated measure anova test. (1 These results were batch dependent)

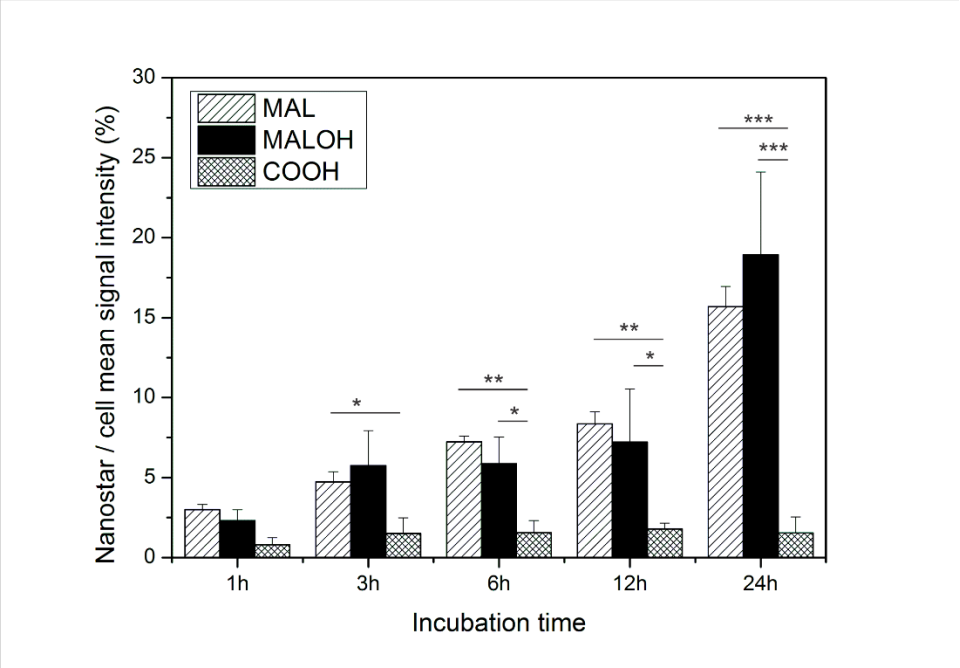

Figure 3.1. Nanostar/cell mean signal intensity deducted of darkfield microscopy images plotted of SKOV3 cells incubated either with nanostars SAM MAL, SAM MALOH and SAM COOH for different time points (1, 3, 6, 12 and 24h; repeated measured two way ANOVA)

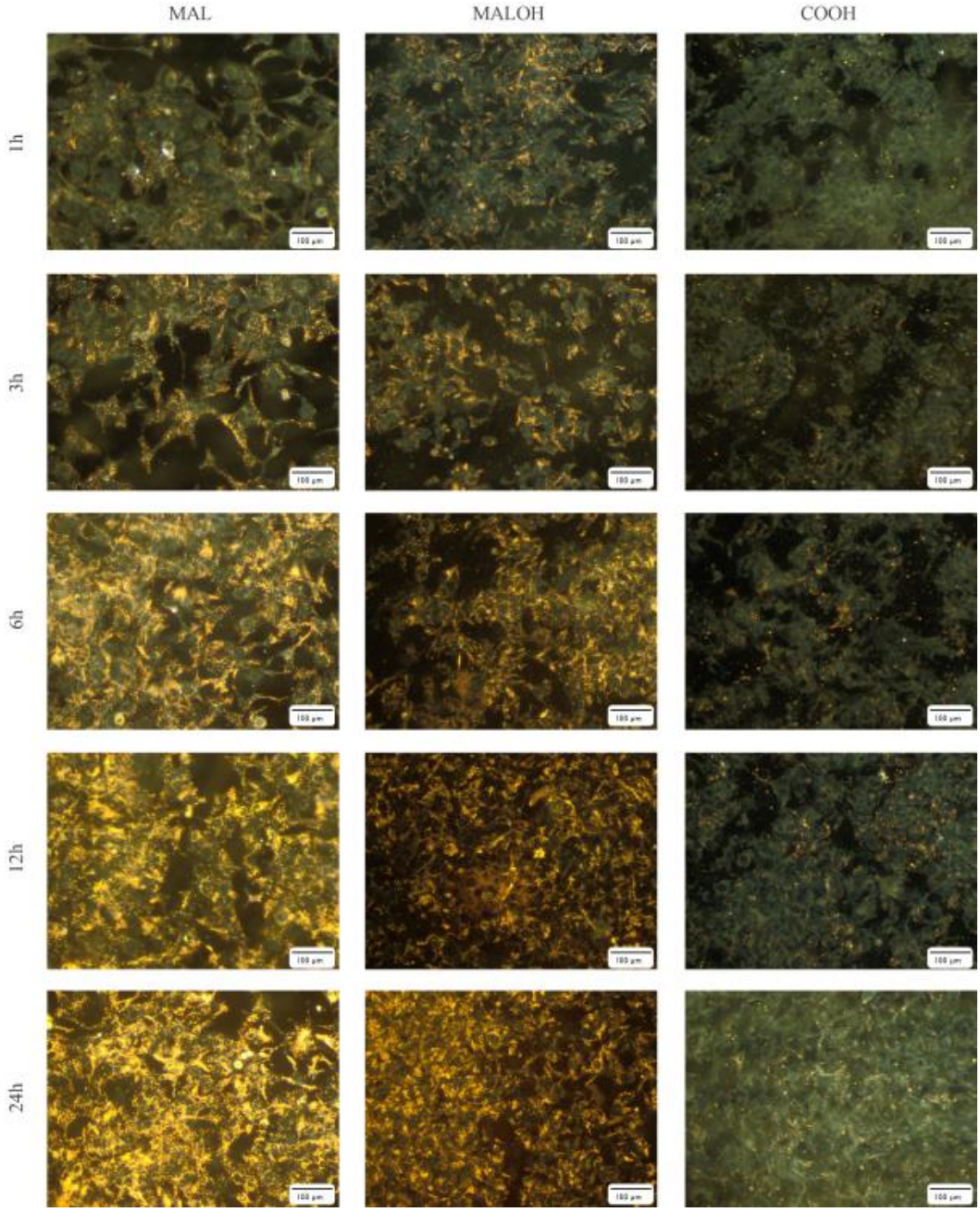

Figure 3.2. Darkfield microscopy images of SKOV3 cells incubated with either nanostars SAM MAL, SAM MALOH and SAM COOH for different time points (1, 3, 6, 12 & 24h)

3.3.3 In vivo biodistribution of nanostars after systemic administration

An important criterion for an effective theranostic agent is a maximal accumulation of the nanostars inside the tumor and a minimal uptake in other organs of the host. Two invasive techniques, darkfield microscopy and ICP-OES, are used to study the biodistribution of the nanostars after i.v. injection.

In Figure 3.3, a comparison of the relative gold concentration in the tumor is shown for two time points (1 and 24h after i.v. injection) compared to the injected amount of gold using ICP-OES. A high gold concentration of 9.2 ± 3.1% in the spleen and 74.8 ± 2.4% in the liver was measured 1h after i.v. injection compared to the injected amount gold. This gold concentration decreased over time (24h) by 47.8% for the spleen and 59.4 % for the liver. As for the tumor only small but non-significant gold concentration was measured after 1h (1.3 ± 1.6%) while a non-significant gold concentration (0.3 ± 0.3%) was measured compared to the control (0.7 ± 0.7%) 24h after i.v. injection. For the other organs (heart and kidney) no gold was measured using ICP-OES.

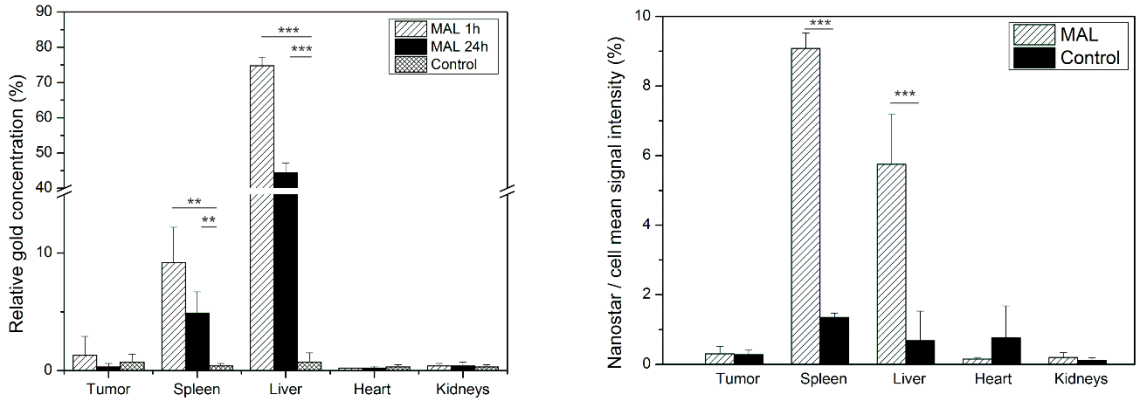

Figure 3.3. Left: Relative gold concentration of different organs at two time points (1 and 24h) after injection of either nanostars SAM MAL or PBS injection where the relative gold concentration is plotted in comparison to the injected amount of gold for the different tissues (one way Anova). Right: Nanostar/cell mean signal intensity of the different organs 24h after injection for either nanostars SAM MAL of PBS injection (t-test).

The distribution of these nanostars inside the organs was visualized 24h after injection using dark-field microscopy. As with ICP-OES, no nanostars were visualized inside the kidney, heart and tumor, while for the liver and spleen significant accumulation was noticed (Figure 3.4). In liver, these nanostars were visualized between the hepatocytes (the bigger cells within the image). In contrast, the nanostars in the spleen are more randomly distributed inside the spleen. When quantifying the gold nanostars pixels compared to the area of the tissue (Figure 3.3), an estimation of nanoparticle density in the tissue was calculated. The highest density was found inside the spleen (9.08 ± 0.44 %) whereas less but still significant levels were noticed inside the liver (5.75 ± 1.43 %). As expected for the tumor, heart and kidney no significant nanostar density was measured compared to the control.

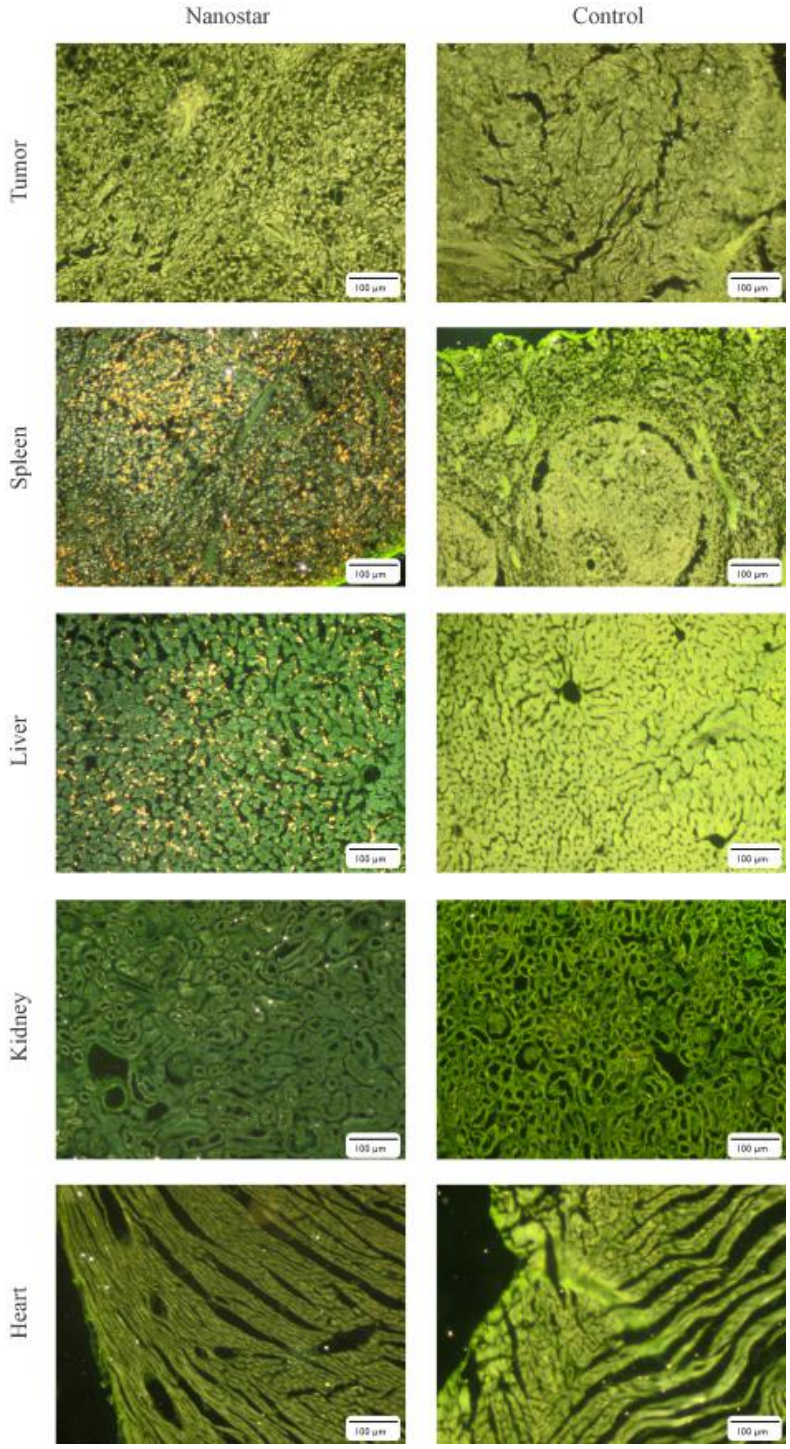

Figure 3.4. Darkfield images of different organs after i.v. injection of either nanostars SAM MAL or PBS.

Similar to the nanostars SAM MAL, ICP-OES experiments were performed after i.v. injection of nanostars SAM COOH (Figure 3.5). As for the SAM MAL functionalized nanostars, no gold was measured in the tumor after 1h (0.3 ± 0.2 %) and 24h (0.1 ± 0 %). The nanostars accumulate to a lesser extent in the liver and this for both time points (1h - 32.3 ± 3.2%; 24h - 28.1 ± 2.5%) after injection. As for the spleen the same gold concentration (9.4 ± 1.4%) was measured compared to the SAM MAL functionalized nanostars for which also a small decrease was observed after 24h (5.7 ±1.6%). A small, but significant gold concentration was measured in the kidney and heart for even 1 and 24h after injection.

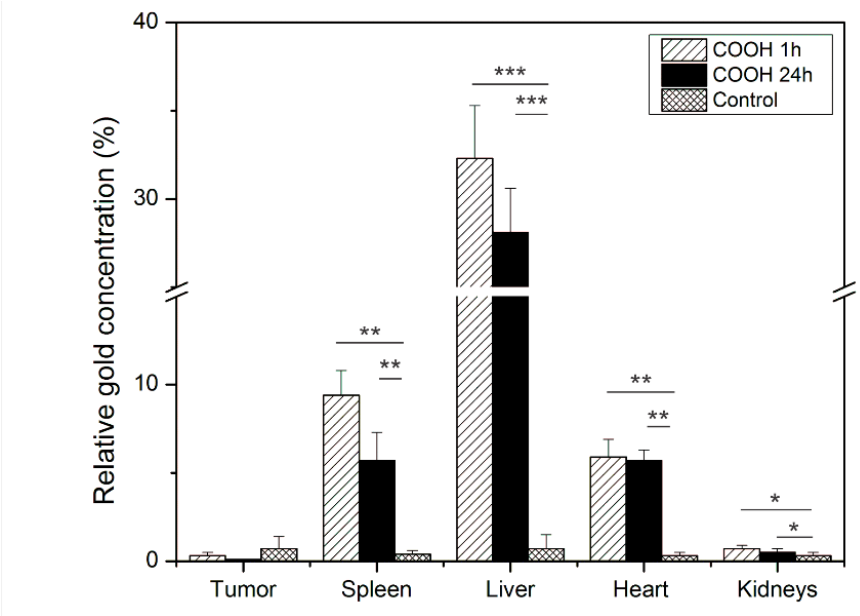

Figure 3.5 Relative gold concentration of tissues either 1h after nanostars COOH, 24h after nanostar SAM COOH or PBS injection where the relative gold concentration is plotted in comparison to the injected amount of gold for the different tissues (one way ANOVA)

3.3.4 In vivo PTT after passive targeting of the tumor

Since ICP-OES and darkfield microscopy are invasive techniques which require a perfusion step, it could happen that the nanostars have flushed out of the respective organs before the biodistribution was measured. As a consequence, a PTT experiment may confirm the ineffective labeling of the tumor cells with the nanostars after i.v. injection.

One day after nanostar administration, the tumors were irradiated for 5 minutes with a NIR laser while the tumor temperature was monitored using a NIR camera. For both the control and the nanostar-injected mice, a gradual increase of the temperature was recorded, reaching a plateau after 180 seconds (Figure 3.6). While in the nanostar injected animals this plateau value was at a temperature difference of 5.5°C, for the control mice around 2 °C. No significant difference between the two conditions in this plateau phase was recorded. Once the laser was turned off the temperature decreased again to normal body temperature after 300 seconds.

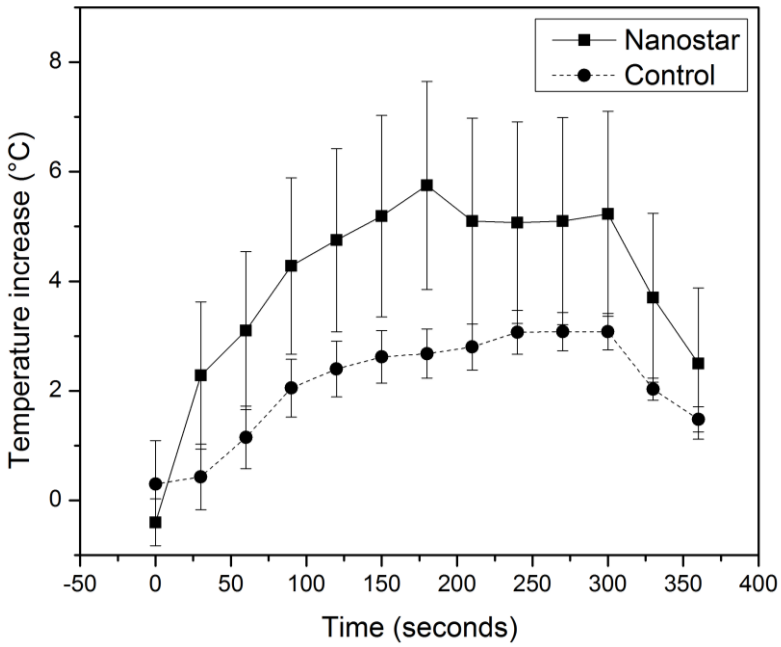

Figure 3.6 The temperature increase plotted over time where the tumor is irradiated at time point 0 until 300 sec where no significance was measured (ANOVA; $p \leq 0.05$)

The PTT effectiveness was monitored for 13 days after therapy for both the control and nanostar administered animals using BLI and MRI. Figure 3.7 shows the BLI intensity after normalization where the same increasing trend was observed for both conditions. Next to the BLI signal, the tumor volume was monitored by MRI showing the same increasing trend as the BLI measurements, by tripling the size of volume after 13 days.

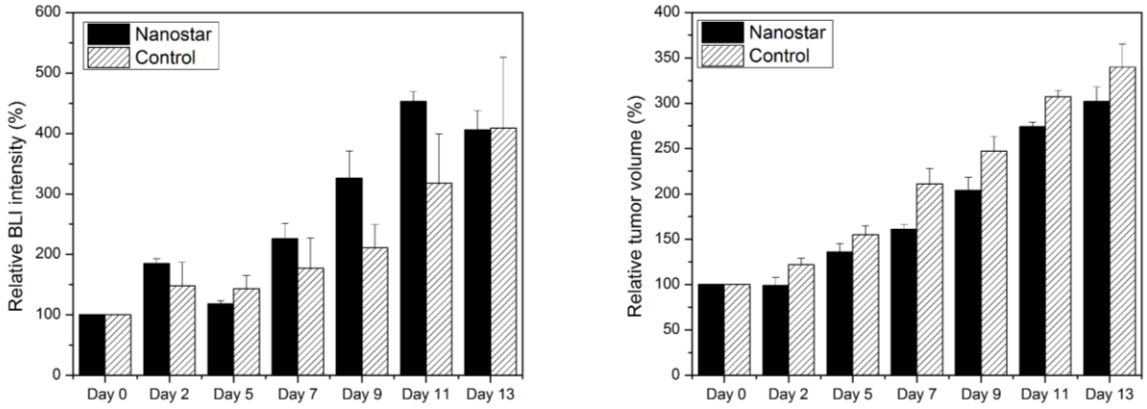

Figure 3.7. Relative BLI intensity (left) and tumor volumes (right) of the tumors after PTT for either i.v. injected nanostars or PBS mice. Treatment was executed at day 1 where no significance was shown over time for the nanostar and PBS administered mice (ANOVA; $p \leq 0.05$)

For evaluating the possible toxic effect of the nanostars, the bodyweight of the mice was monitored during the follow up after PTT (Figure 3.8). No significant difference between the two groups was found over time where, both conditions started with almost the same weight 19.7 ±0.7 g for the nanostars injected animals and 20.7 ±1.6 g for the control mice. At the last end point, the toxicology was evaluated on tissue level using H&E staining looking at inflammation or other tissue damage. No visual differences were detected between the nanostars and PBS injected animals and for all organs, focusing at the cell morphology and possible nucleus degradation (Figure 3.9). Also the vascularization of the tumor has been histological examined using a marker target CD31 which is found on endothelial cells in vascularized tumors and αSMA found on smooth muscle cells in the tumor. Both markers were clearly visualized (brown color) on the tumor sections (Figure 3.9).

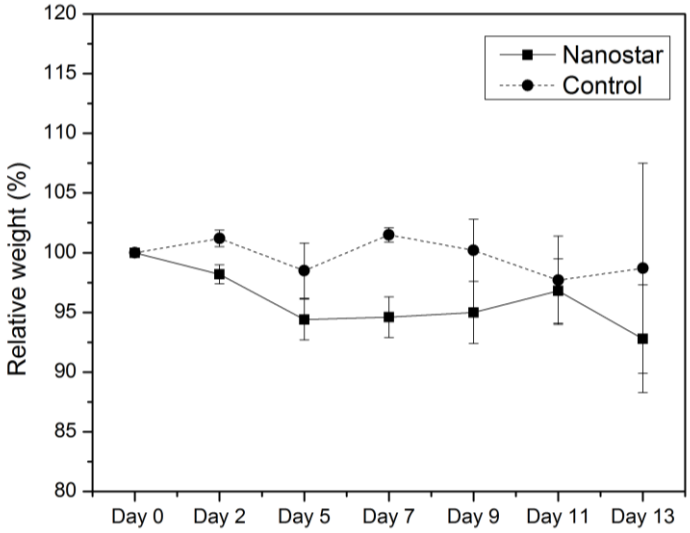

Figure 3.8 Mean weight of the mice in each group during the follow up after PTT. No significant decrease in weight was measured (ANOVA; $p \leq 0.05$)

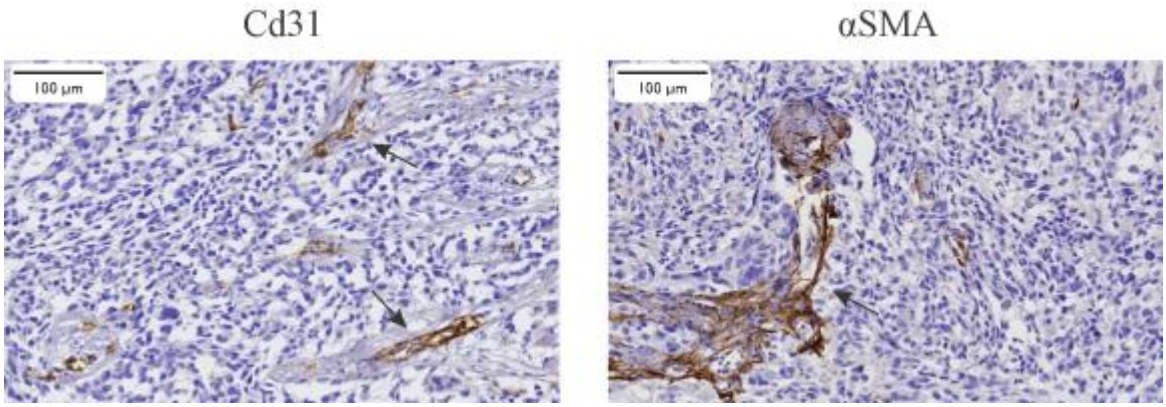

Figure 3.9 Histology images of SKOV3 tumors either stained targeting CD31 or aSMA

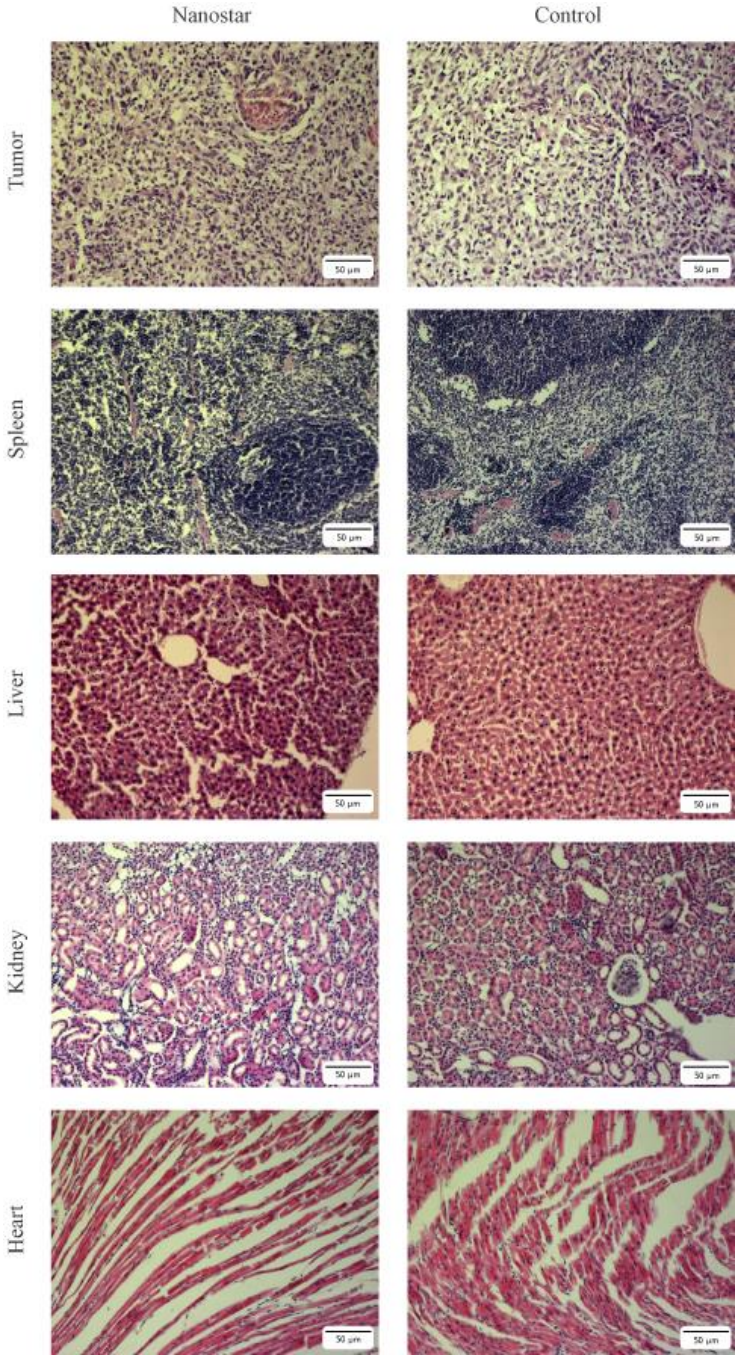

Figure 3.10. Histology images after H&E staining of the tumor, spleen, liver, kidney and heart after either i.v. injection of the nanostars SAM MAL or PBS.

3.4 Discussion

The nanoparticle characteristics have a huge influence on the intracellular uptake during passive tumor targeting. Hereby the size, shape and charge play a crucial role on this uptake but still big debates are ongoing about the efficacy of tumor targeting using anionic nanoparticles. To study this effect, we efficiently functionalized the nanostars with a SAM having different end groups (MAL, MALOH and COOH). We confirmed this by measuring a red shift of the LSPR band in the NIR region, due to a change in the refraction index, and a shift in hydrodynamic diameter since a SAM is formed on the nanostars' surface. After functionalization, the negative zetapotential showed small differences between the three types of nanostars due to these different end groups. The nanostars SAM COOH gives a slightly more negative zetapotential while the nanostars SAM MALOH is more positive compared to the SAM MAL due to the alcohol groups[159].

For the intracellular uptake of the nanostars, we noticed a huge effect of changing the SAM's chemical end group of the nanostar. While for the nanostars SAM MAL and MALOH a high intracellular uptake was visualized, almost no uptake was visualized using COOH SAM-functionalized nanostars. This finding is contrary to the higher accumulation that was expected for the nanostars SAM COOH since they have a more negative charged zetapotential favoring cellular interaction with the cationic places on the cell membrane. Nevertheless, such small changes in zetapotential could not be the only reason for this significant difference in cellular uptake that we observed.

To further explain the large difference in uptake among the tested nanostars, another effect must be taken into account, namely the creation of a protein corona around these nanostars in serum conditions[140]. The protein corona defines the adsorption of biological molecules on the nanoparticles, thereby changing the interface between the cells and the nanostars. We measured this effect by the difference in hydrodynamic diameter of the nanostars in cell culture medium with serum and water. While for nanostars with SAM MAL the largest protein corona is measured, this is lower for the nanostars with SAM MALOH and almost no protein corona for the nanostars SAM COOH. This protein corona formation could be due to the reactivity of the

maleimide end group which may bind to cysteine groups of proteins in the cell culture mediums as has been shown in literature[160].
Normally the protein corona reduces the uptake of the nanoparticles inside the tumor cells[161,162], while we noticed a favored uptake within this case. We hypothesize that by shielding the negative surface of the nanostars SAM MAL and SAM MALOH by the protein corona, a favored uptake is observed compared to nanostars SAM COOH. Hereby there could be a threshold point of this protein corona between the hydrodynamic diameter shift of 13.1 nm for the nanostars SAM MALOH and 4.5 nm for the nanostars SAM COOH. Also the protein corona could change composition by using different end groups, which may have an effect on cellular uptake[163]. Another effect could be the reactivity of maleimide to thiols, which are abundant on cell receptors in contrary to carboxyl groups which are mild reactive to proteins[164]. In general, this protein corona changes the identity of the nanostars and must be taken into account to predict the intracellular uptake of the nanostars.

The high accumulation of negatively charged nanostars in the tumor cells that we observed *in vitro*, does not guarantees good accumulation inside the tumor. Therefore, we studied the *in vivo* passive targeting capabilities of both the nanostars SAM MAL and SAM COOH, taking into account the effect of the presence of a protein corona around the nanostars in serum conditions. For both conditions no accumulation was observed 1h and 24h after i.v. injection of the nanostars. Several reasons could be considered regarding the unsuccessful accumulation of the nanostars inside the tumor. For instance this could be dependent on the tumor vasculature or the nanoparticle uptake by the RES[19,130]. Not all tumors have are well vascularized favoring the passive accumulation of the nanostars in the tumor by the EPR effect as has been shown for some tumor types. SKOV3 tumors with a vascularization have been observed and we visualized this by histology marking the cluster of differentiation 31 and alpha smooth muscle actin[165]. While CD31is a histological marker for vascularized tumors, αSMA is a marker for smooth muscles inside the tumor. As a consequence the failure of nanostars accumulation is not caused by a non-vascularized tumor. Since our SKOV3 tumors showed clear visualization of these markers, we can conclude that the tumors are well vascularized, meaning that the passive targeting failure is not caused by the tumor vasculature. Another reasoning is the involvement of the RES which responsibility is filtration and phagocytosis of xenobiotic material such as the nanostars. The result of the RES function of liver and spleen is decreasing the blood retention time, resulting in

a limitation of the nanoparticles that pass through the tumor. Due to this RES recognition the nanostars accumulated inside the liver and spleen. We indeed observed that within the liver the nanostars are located in the Kupffer cells between the bigger hepatocytes not showing any nanostar uptake. In the spleen the nanostars are more distributed over the whole organ. Next to the RES uptake, these organs are also characterized by fenestrae, where nanoparticles up to 100 nm can pass through, such as our nanostars.

The uptake of the RES system is dependent on different factor including the size, shape and charge of the nanoparticles. The RES will easily recognize bigger and spherical particles compared to smaller or more discoidal/nanorod shaped nanoparticles[52,166]. Since our nanostars can be described as a sphere with nanorods as branches, they may have a longer blood retention time.

A last factor is the charge by the nanoparticle where the blood retention time decreases from cationic, anionic to neutral nanoparticles[47]. Hereby the opsonization process plays a crucial role where plasma proteins adsorb on the nanoparticle surface, facilitating the phagocytosis by the macrophages in the RES[167]. This protein corona was mimicked using the cell culture medium with serum where the nanostars SAM MAL show a clear formation of the protein corona. As a consequence these nanostars are immediately recognized by the RES resulting in low tumor uptake and high liver and spleen uptake which is confirmed by ICP-OES and darkfield microscopy. For the nanostars SAM COOH this situation is different where almost no protein corona is noticed after incubating in cell culture medium conditions, resulting in probable longer blood retention time.

This difference in protein corona could explain the subtle differences in the biodistribution of these nanostars having a different end group. The main difference was the small accumulation of the nanostars SAM COOH in the kidney and heart, which could be explained by a longer retention time in the blood. This was confirmed by the lower uptake in the liver due to a lower recognition of the nanostars SAM COOH by the RES system, while the nanostars SAM MAL are immediately recognized by the RES system due to the presence of a protein corona. Moreover macrophages are characterized with scavenger receptors which are loaded with cysteines, recognizing negatively charged molecules[52]. Since maleimide groups are reactive with thiols on these cysteine

groups, the nanostars SAM MAL could increase the recognition of these nanostars by the macrophages.

Still, given the high concentration of nanostars inside the liver and spleen for the nanostars SAM MAL, no acute toxicity is noticed. This is an encouraging observation, as it is an indication that systemic nanostar administration would not have harmful side effects for the mouse, and by extension, the patient. This non acute toxicity is supported by the weight of the animals that stays normal 13 days after nanostars administration and PTT. Also, detailed histological evaluation of the tissues showed no nucleus degradation or cell morphology changes. Nonetheless, some studies have evaluated the possible long term toxicity of gold nanoparticles and observed a change in the upregulation of genes and the increase in volume of the Kupffer cells[168]. Aiming at the evaluation of the clinical applicability of NPs, the assessment of NP toxicity will remain a very important aspect in future in vivo studies.

Given the inefficient nanostar uptake by the tumors upon passive delivery, it is not to our surprise that PTT performed 24h after i.v. nanostars-SAM-MAL injection remained ineffective. This was indicated by the non-significant temperature increase during PTT compared to the temperature rise observed during PTT of tumors that were directly injected with nanostars. That we could not observe any tumor viability and size decrease quantified by BLI and MRI was consistent with these results.

This PTT effectiveness could be increased by a better tumor uptake where the nanostars have a decreased recognition by the RES system and potentially by actively target the nanostars using a biological ligand[169,170]. Hereby several biological ligands as antibodies, proteins, nanobodies have been used as an effective ligand to target overexpressed receptors on tumor cells.

3.5 Conclusion

In this chapter we examined the potential of passive targeting of tumors after systemic nanostars delivery. We revealed the inefficiency of this approach and investigated possible reasons of the observed inefficiency of tumor targeting using a passive strategy with anionic charged nanostars.

A huge difference in intracellular uptake of the nanostars is shown related to the reduction of the protein corona by changing the end group of the SAM on the nanostars. A marginal uptake in the tumor is shown for both types of nanostars where they tend to accumulate in the spleen and liver. To increase possible tumor accumulation the nanostars, we propose that nanostars may be biofunctionalized for active targeting the tumor cells. This strategy we investigate in the next chapter.

4 LIMITING THE PROTEIN CORONA: A SUCCESSFUL STRATEGY FOR *IN VIVO* ACTIVE TARGETING OF ANTI-HER2 NANOBODY-FUNCTIONALIZED NANOSTARS.

4.1 Introduction

Finding an effective way to target tumors by using a theranostic nanoparticles is a big challenge up to now[22]. Hereby two targeting strategies, either passive or active, have been intensively studied[171]. While passive targeting is based on the diffusion of the nanoparticles into the tumor tissue by the enhanced permeability and retention effect, active targeting makes use of biological ligands coupled onto the nanoparticles to recognize overexpressed receptors of tumor cells. However, these targeting approaches have had different outcomes due to several reasons ranging from the inappropriate tumor models to nanoparticle properties like their geometry, chemistry and many others[57,95].

During the last decade, many efforts have been made to optimize nanoparticle properties to succeed in targeting tumors[172]. Several criteria, such as size and charge, have been intensely discussed to enhance *in vivo* tumor uptake[47]. In essence, a poly-ethylene glycol (PEG) layer, a neutral charge and a nanoparticle diameter around 50 nm were found to be crucial[53]. Next to a

better tumor retention due to the EPR effect, these conditions are also linked to a longer blood retention time and by decreasing the recognition of the nanoparticle by the immune system[56,173].
The characteristics of the nanoparticles in water are completely different than the ones under *in vivo* conditions, which will determine the efficient targeting of the tumor cells by the nanoparticles[15]. Indeed, *in vivo* effects have to be taken into account when studying targeting efficiency such as the protein corona. This is generated on the nanoparticle surface in the presence of serum and consists in essence of different proteins where its composition is constantly changing over time[10,11]. The protein corona is composed of a 'hard' corona, consisting of tightly bound proteins, and a 'soft' corona of loosely bound interchangeable proteins[12]. The composition of the protein corona is also influenced by several factors that are unique for each type of nanoparticle, where surface charge and hydrophobicity are the most determining ones [13,14]. As a consequence, efforts have been made during the last years to visualize and biologically validate the protein corona demonstrating important differences between *in vitro* and *in vivo* conditions.
To maximize tumor targeting it is crucial to study the influence of the protein corona on the targeting efficiency of the tumor cells by the nanoparticles and how to manipulate this corona to achieve an efficient targeting. While specific, active targeting of tumor cells by nanoparticles may be shown under conditions without serum, the outcome could be completely changed by the formation of a protein corona in the presence of serum. It may even change over time such as in late-stage versus early-stage of disease[16]. Moreover, the protein corona also plays an important role for cell recognition during nanoparticle endocytosis, affecting the intracellular fate of nanoparticles[17]. As a consequence, the protein corona shows a crucial influence on the passive and active cell targeting and may lead to a complete loss of targeting capabilities [18,19]. By using mathematical models to predict the protein corona composition and by tailoring the protein corona, first steps were taken to overcome this problem in order to generate active targeting compounds[20–22].
Here, we present a methodology to reduce the formation of a protein corona on gold nanostars that are functionalized with a self-assembled monolayer containing maleimide end groups. To prove the active targeting concept, the cancer cell receptor human epidermal growth factor 2 (HER2), targeted by camel-derived nanobodies is used as a model[23,24]. The HER2-receptor was chosen because up to 30% of breast cancers show an overexpression of this receptor, while expression levels in normal tissues are close to absent, making it an interesting target for anti-

cancer therapy[25]. Targeting has been optimized by using anti-HER2 nanobodies. Nanobodies consist of the antigen-binding domain of a heavy chain-only camelid antibody and bear intrinsic properties such as smaller size and higher stability than anti-HER2 monoclonal antibodies like Herceptin[23]. These nanobodies are covalently bound the gold nanostars with a self-assembled monolayer as the interface. Nanostars are chosen since they a promising type of gold nanoparticles due to their higher absorption coefficient crucial for photoacoustic imaging (PAI) and photothermal therapy (PTT) compared to other shaped nanoparticles [26,27].

To test our approach under *in vitro* and *in vivo* conditions in a mouse model, two different cell lines were used throughout this study, an ovarian cancer cell line (SKOV3) showing high expression of HER2 receptors and a hamster ovarian cancer cell line (CHO) as a negative control. By using these two cell lines and three different types of nanoparticles (non-biofunctionalized or biofunctionalized with either anti-HER2 or control nanobodies, the specificity of active targeting was studied, both under non-serum and serum conditions.

4.2 Material and Methods

4.2.1 Nanostar synthesis, functionalization and characterization.

Nanostar synthesis and functionalization with the SAM molecule (1.2mM, (HS–(CH2)11–(O–CH2–CH2)6–O–CH2–MAL)2), have been previously described in chapter 2 resulting in batch of SAM functionalized nanostars solved in HEPES buffer (pH=7, 10 mM). Nanobodies (2Rb17c and cAbcII10) were synthesized with an end standing cysteine group as published by Massa et al. 182. To attach these nanobodies onto the maleimide end group of the SAM-coated nanostars, the nanostar suspension was mixed with an identical volume of nanobodies dissolved in HEPES buffer. A range of nanobody concentration has been added to the nanostar suspension to define an optimal concentration (monomer: 0; 0;25;0;5;1;2;5;5;10 µg/mL and reduced dimer: 0;0;01; 0,05; 0,1; 0,5; 1;2 µg/mL). After overnight shaking, the suspension was centrifuged at 4000 rpm for 60 minutes. Subsequently, the supernatant was discarded and the pellet resuspended in the desired buffer. After each functionalization step, the absorbance, hence shift in plasmon resonance band of the nanostars was measured using UV-Vis absorption spectroscopy (Shimadzu UV-1601PC, Brussels, Belgium). Their hydrodynamic diameter as well as zeta-potential was determined using dynamic light scattering (DLS; Malvern Nanosizer, WR, United Kingdom).

These nanoparticles are also examined on their stability in the respective cell culture mediums (with and without serum) for the SKOV3 and CHO cells using the same characterization techniques. All chemical compounds were purchased from Sigma Aldrich (Diegem, Belgium)

For blocking experiments of the maleimide end groups, the same protocol was used for the biofunctionalized and non-biofunctionalized nanostars. Five different blocking agents were tested three different short molecules, namely 3-mercaptopropionic acid ('SHCOOH'), 2-mercaptoethylamine ('SHNH') and 2-mercaptoethanol ('SHOH') and two molecules containing a poly-ethylene glycol (PEG) chain, namely O-(2-Mercaptoethyl)-O′-(2-carboxyethy)heptaethylene glycol ('PEGCOOH') and O-(2-Mercaptoethyl)-O′-methyl-hexa(ethylene glycol) ('PEGCH'). For functionalizing the nanostars with these blocking agents, 3 mL of the nanostars (6.9 10^{11} nanostars/mL) were mixed with 300 µL of the blocking agents at different concentrations (1.2, 2.4 and 12 mM). After 60 minutes of centrifugation at 4000 rpm, the nanostars were re-suspended in either MES buffer or cell culture medium either with or without serum to characterize this suspension by UV-Vis absorption spectroscopy and DLS. All chemical compounds were purchased from Sigma Aldrich (Diegem, Belgium).

4.2.2 Cell culture.

Both, SKOV3 and CHO cells (ATCC® HTB77, Cedex, France) were maintained at 37 °C and 5% CO_2 in 75 cm^2 cell culture flasks. SKOV3 cells were cultured in a RPMI1640 medium and the CHO cells in DMEM medium both supplemented with 10% Fetal Bovine Serum, 1% Penicillin Streptomycin and 1% L-glutamine. All cell culture reagents were purchased from Invitrogen Life Technologies Life Sciences (Gent, Belgium). Darkfield microscopy for in vitro active targeting.

4.2.3 Darkfield microscopy

Tumor cells were seeded at a density of 150.000 cells/well in a 12 well plate and incubated overnight. Nanostars (5.7x10^9 nanostars/mL) were added to the suspension. After 6h of incubation, they were washed twice with cell culture medium. After an overnight incubation with fresh medium, tumor cells were trypsinized and seeded onto a coverslip. After another overnight incubation, the cells were fixed with 4% paraformaldehyde and washed three times with PBS.

After mounting the coverslip on a glass slice, the tumor cells were visualized using darkfield microscopy. The dark field measurements were performed using an Olympus BX51 microscope (Olympus, Berchem, Belgium) equipped with a dark field condenser and an objective (10×). The microscope was fitted with Soft Imaging System's Colorview III camera and AnalySIS Life Sciences software (Olympus, Berchem, Belgium).

Darkfield microscopy images were quantified using CoralPaint Software where the yellow pixels (nanostars) and green pixels (tumor cells) were deducted from the images and converted into white pixels. The number of white pixels was calculated for both conditions. The number of nanostars pixels was divided by the number of cell pixels to result in the nanostars/cell mean signal intensity

4.2.4 In vivo tumor model and photoacoustic imaging of the nanostars in vivo.

Female athymic nude mice (8 weeks, Harlan, Host, The Netherlands) were used during these experiments. All animal experiments were approved by the local animal ethics committee of the KULeuven and were performed according to the national and European Regulations. Animals were kept in individually ventilated cages with food and water *ad libidum*. A total number of 1 x 10^7 SKOV3 tumor cells suspended in 100 µL cell culture medium were injected into each hind limb of the mice and left for two weeks to grow into solid tumors.

After tumor formation (size > 200 mm^3), 200 µL of nanostars (2.7 10^{12} nanostars/mL) were intravenously (i.v.) injected into animals (n=3). Three hours after nanostar injection, tumors were imaged by photoacoustic imaging (PAI) using a multi-wavelength approach. Hereby, a VevoLazer 2001 (Visualsonics, Amsterdam, The Netherlands) was used with the following parameters: 10 ns pulsed laser with a power of 20 mJ/cm^2 and a 200 mHz frequency. To spectrally unmix the gold nanostar signal from the hemoglobine's photoacoustic signal, the tumors were irradiated at different wavelengths (680, 700, 720, 750, 800, 850 nm). During *in vivo* PA imaging, ultrasound imaging was used to determine the tumor location. The PA signal intensity was measured over the complete region of interest (ROI), defined as the tumor volume, before and after nanostar administration.

4.2.5 Histopathology

To confirm the location of the nanostars, animals were sacrificed and perfused with 4% PFA after the PAI experiments. The following tissues were removed: kidney, liver, tumor, heart and spleen. After embedding in paraffin and sectioning in slices of 7 µm width, the sections were de-paraffinized before visualizing them with darkfield microscopy.

4.2.6 Statistical analysis

For quantification of the darkfield data, nanostars/cell mean signal intensity was calculated. Statistical analyses were executed on the quantitative data using a paired t-test where the degree of significance is indicated with *: $p < 0.05$; **: $p < 0.01$; ***: $p < 0.001$.

4.3 Results

4.3.1 Nanostar biofunctionalization

Nanostars are synthesized and maleimide functionalized having their plasmon band maximum at 674.5 ± 10.7 nm and an average hydrodynamic diameter of 75.0 ± 5.6 nm as previously described[26,29]. Nanobodies (2Rb17c and cAbBcII10) with an end-standing cysteine group were chemically bound onto the maleimide end group of the nanostar's coating by nucleophilic addition. As it was described by Massa et al. a spontaneous dimerization can occur during the nanobody's synthesis (with Cysteine at C-terminal end), resulting in fractions of monomers and dimers of nanobodies[24]. To reduce the cystins and to avoid the formation of dimers, a mild reduction with 2-mercaptoethylamine was performed to have only monomers with an end-standing cysteine group that can then react with the maleimide group. A difference in maximum nanobody concentration was measured for the monomer fraction (1 µg/mL) compared to the reduced dimer fraction (0.05 µg/mL). For both fractions, the nanostars were unstable at higher nanobody concentrations as shown by the broadening or disappearance of the plasmon band (Figure 4.1). At the optimal nanobody concentrations a non-significant plasmon band shift was noticed compared to the non-biofunctionalized nanostars. Using DLS, the same trend of increased hydrodynamic diameter was observed with a non-significant increase after biofunctionalization. For the determination of zetapotential, a less negative potential was measured for biofunctionalized compared to non-biofunctionalized nanostars (Table 4.1). This trend was

observed for all batches of nanobodies. As a consequence in the continuing text no differences will be made between the reduced dimer or monomer fraction.

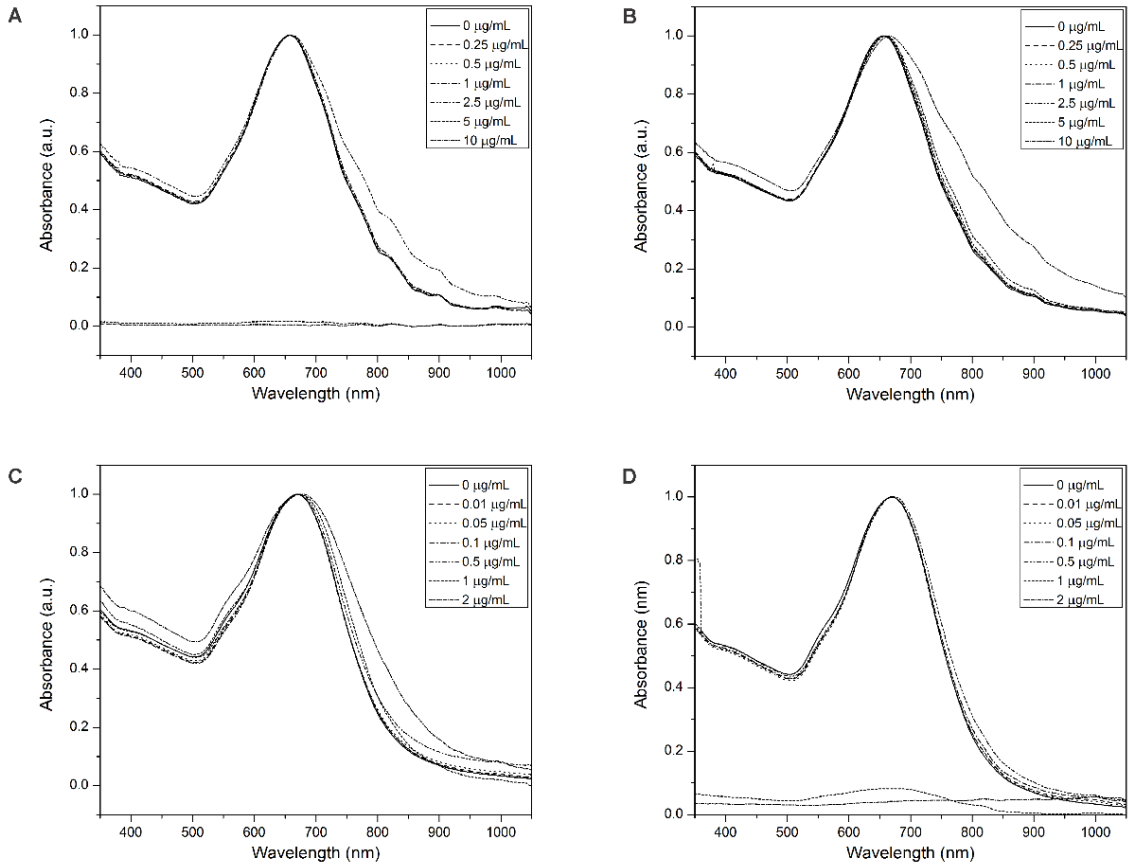

Figure 4.1 UV-Vis absorption spectroscopy for nanostars functionalized with various concentrations of either monomer 2Rb17c (A), monomer cAbcII10 (monomer), reduced dimer 2Rb17c (C), reduced dimer cAbcII10 (C)

Table 4.1 For the different sets of nanostars functionalized with nanobodies, the LSPR band shift, hydrodynamic diameters and zetapotential are reported. Data represent mean values ± standard deviations for three independent experiments.

	2Rb17c monomer	**cAbcII10 monomer**	**2Rb17c reduced dimer**	**cAbcII10 reduced dimer**
LSPR band shift (nm)	1.5 ± 1.0	1.0 ± 1.0	1.5 ± 0.5	2.0 ± 1.0
Hydrodynamic diameter increase (nm)	5.3 ± 3.7	6.2 ± 4.2	4.8 ± 2.9	5.3 ± 3.9
Zetapotential (mV)	-36.3 ± 3.5	-37.2 ± 2.9	-37.6 ± 2.6	-35.8 ± 3.2

Since the gold nanostars will ultimately be used under physiological conditions, their stability was examined in different cell culture media (with and without serum) and characterized by using UV-Vis absorption spectroscopy (data not shown). All bio-functionalized nanostars were stable in these different media as indicated by the absence of LSPR band broadening. Still, these characteristics only suggest a successful biofunctionalization, while we do not know if the nanobody concentration on the nanostars is high enough to succeed in active targeting and if the nanobodies are accessible to target the HER2 receptor once bound onto the nanostars.

Since the gold nanostars are to be used under physiological conditions, their stability was examined in different cell culture media (with and without serum) and characterized by using UV-Vis absorption spectroscopy and dynamic light scattering (Figure 4.2). All bio-functionalized nanostars were stable in these different media as indicated by the absence of localized surface plasmon resonance (LSPR) band broadening. Still, an increase of the hydrodynamic diameter was observed when nanoparticles were exposed to standard SKOV3 cell culture medium. For the non-biofunctionalized nanostars a hydrodynamic diameter of 27.3 ± 2.4 nm was noted, whereas the 2Rb17c- and cAbBcII10-functionalized nanostars had a hydrodynamic diameter of 26.8 ± 3.2 nm and 25.4 ± 2.7 nm, respectively (Figure S7). In CHO cell culture medium with serum, the formation of a protein corona increased the hydrodynamic diameter to 20.4 ± 2.1 nm, 20.8 ± 3.9 nm and 16.9 ± 3.1 nm for the non-biofunctionalized nanostars, the 2R17c and the cAbBcII10 functionalized nanostars, respectively. These expansions are due to the formation of the protein

corona, which did not have an effect on the nanoparticle stabilities as no broadening of the plasmon band was measured compared to the plasmon band in water. Furthermore, these characteristics are only suggestive for a successful biofunctionalization, since at this stage we do not know if the nanobody concentration on the nanostars is sufficient to provoke an active targeting and if the nanobodies onto the nanostars are available for HER2 receptor recognition.

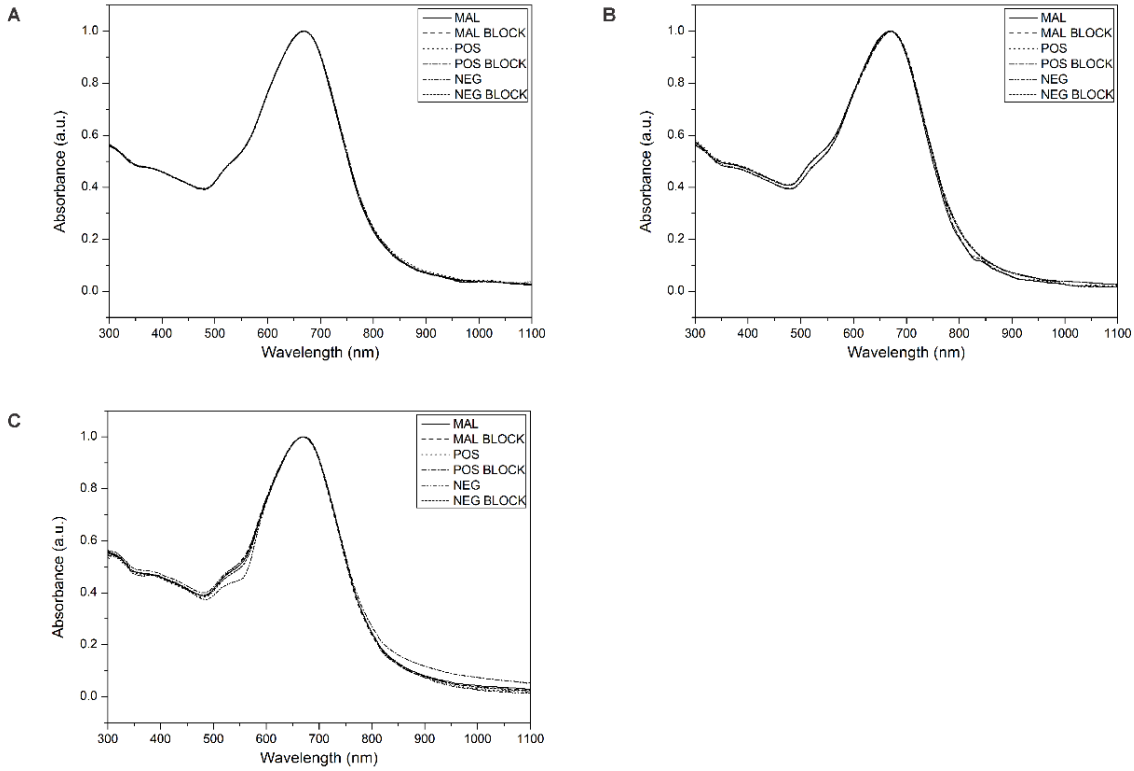

Figure 4.2 UV-Vis absorption spectroscopy of the nanostars – biofunctionalized and/or blocked with SHOH - in HEPES buffer (A), cell culture medium with serum (B) and cell culture medium without serum (C).

4.3.2 In vitro visualization of active targeting using biofunctionalized nanostars.

To verify if the 2Rb17c nanobody actively recognizes the HER2 receptor on the SKOV3 tumor cells, nanostars were incubated in medium not containing serum at a temperature of 4 °C. In general, under this non-physiological condition no protein corona is generated and passive targeting is inhibited since the receptor-mediated endocytosis pathway is blocked at this low

temperature[30,31]. First, darkfield microscopy was used to image the interaction of the nanostars with the HER2-positive SKOV3 cells. As shown in Figure 4.3, , the nanostars functionalized with 2Rb17c (POS) showed high accumulation in the SKOV3 cells while the other two control nanostars, the non-biofunctionalized nanostars (MAL) and nanostars functionalized with a non-targeting control nanobody cAbBcII10 (NEG), showed minimal accumulation inside the tumor cells. (Figure 4.4). No statistically significant differences in uptake were noticed between the three types of nanostars for CHO cell labelling. Using quantitative darkfield microscopy data, the same trends were quantitatively confirmed with a higher uptake for the 2Rb17c functionalized nanostars (POS) under these non-serum containing culturing conditions (Figure 4.5)

Exertion of these experiments at a temperature of 37 °C resulted in a different outcome (Figure 3). No difference in targeting was observed between the three types of particles due to a higher passive uptake of the two control nanoparticles. Similarly, incubation of the nanostars with the tumor cells in standard medium (with serum) at 4 °C resulted in a diminished specific accumulation in HER-2 expressing SKOV3 cells compared to the conditions without serum: the 2Rb17c functionalized nanostars showed similar uptake by the HER2 expressing tumor cells when compared with the control nanoparticles, which resulted in a slightly decreased intracellular nanostar concentration when compared to the uptake without serum, for both SKOV3 and CHO tumor cells (Figure 4.4). Also, at a temperature of 37^{o}C, no active targeting was observed where a similar decreased uptake was observed as for non-serum containing conditions. Comparing the different conditions for the CHO cells, no significant difference in nanostar uptake was seen, indicated by the absence of the yellow colored nanostars. These trends are quantitatively shown in Figure 4.5.

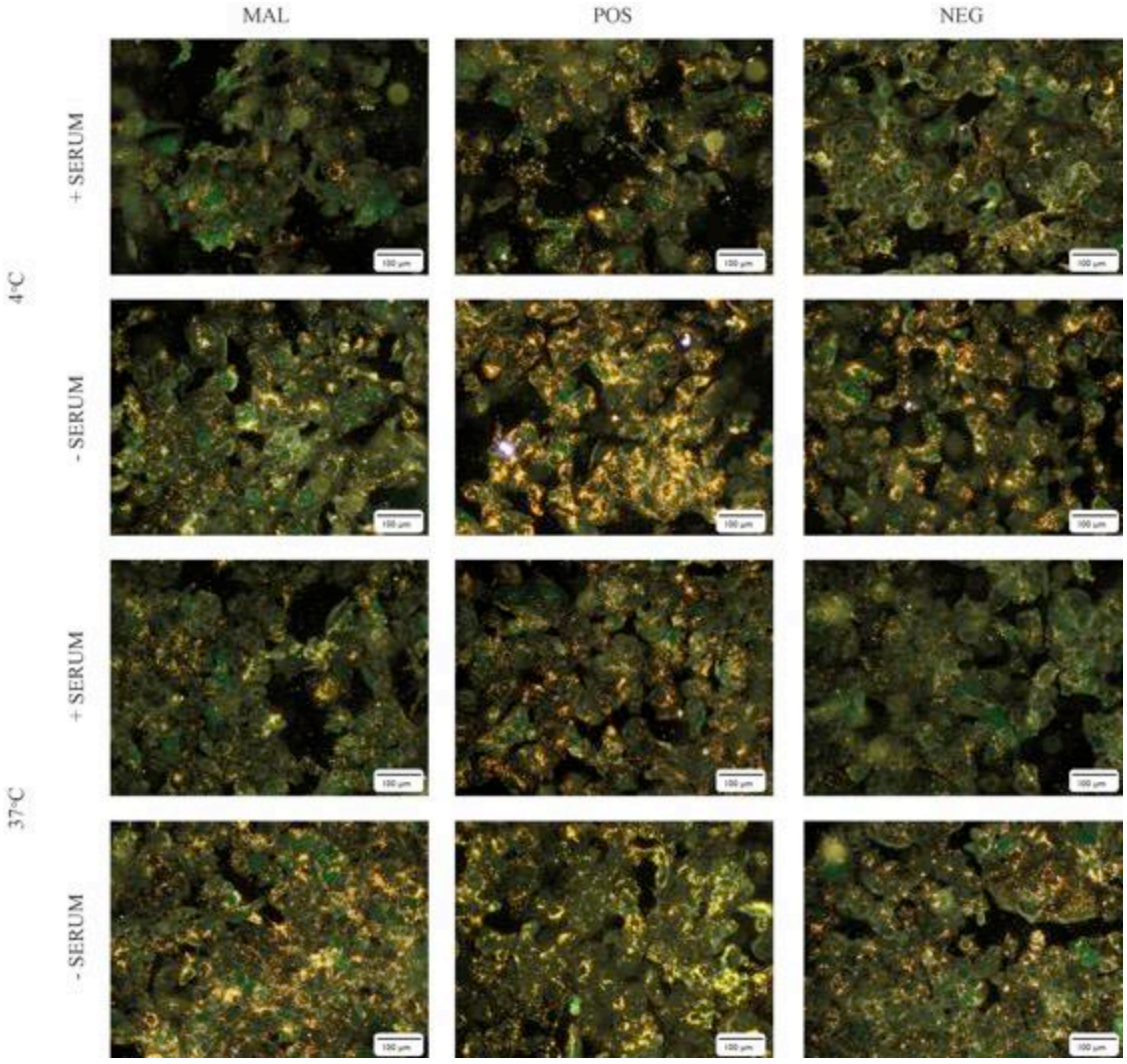

Figure 4.3 Darkfield microscopy images of SKOV3 cells (green) incubated with either non-biofunctionalized nanostars (MAL), biofunctionalized with 2Rb17c (POS) and cAbcII10 (NEG) for different incubation conditions visualized by the yellow spots.

..

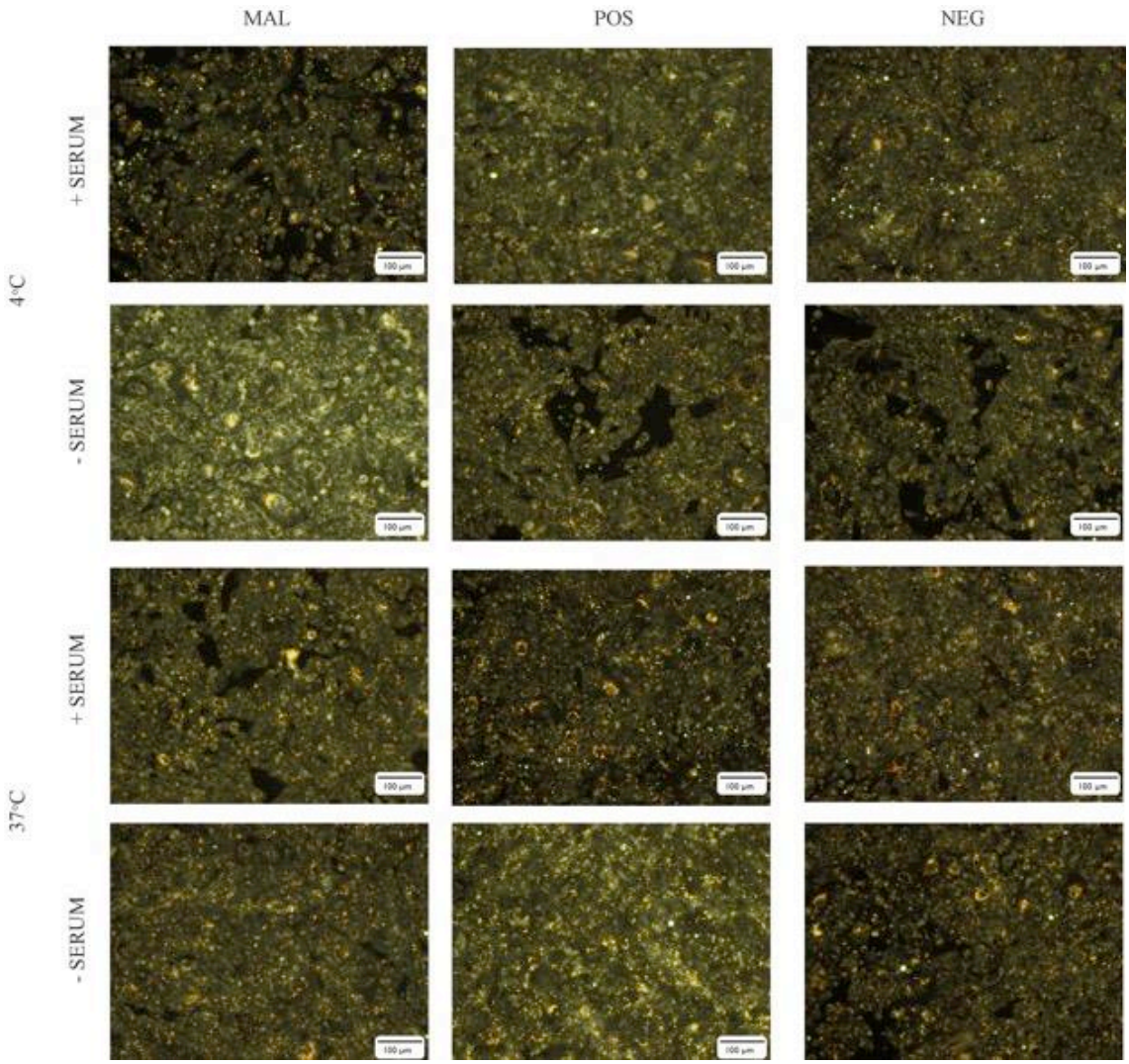

Figure 4.4 Darkfield microscopy images of CHO cells incubated with either non-biofunctionalized nanostars (MAL), biofunctionalized with 2Rb17c (POS) and cAbcII10 (NEG) for different incubation conditions.

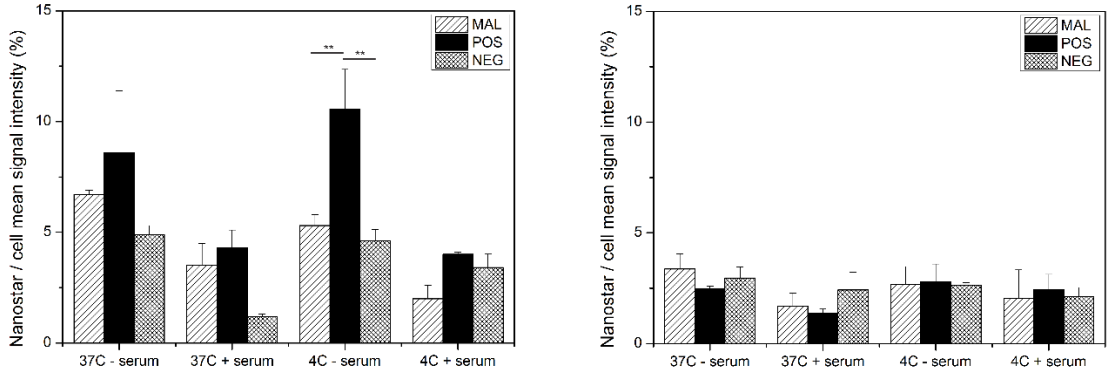

Figure 4.5 Nanostar/ cell intensity for SKOV3 cells (A) or CHO cells (B) incubated with either non-biofunctionalized nanostars (MAL), biofunctionalized with 2Rb17c (POS) and cAbcII10 (NEG) for different incubation conditions.

4.3.3 Reducing the size of the protein corona reduces passive targeting

It was shown that nanoparticles with a functional maleimide end group have failed in active targeting due to the generation of a protein corona[18]. To overcome this problem, various compounds have been tested to block the maleimide serum interactions on nanoparticle surfaces[32]. We have examined three different short molecules (SHCOOH, SHNH and SHOH) and two molecules containing a PEG chain (PEGCOOH, PEGCH) to block the maleimide end groups. Each of these molecules has an end-standing thiol group, which will covalently bind to the maleimide group. In a first set of experiments, the blocking capabilities were examined on the non-biofunctionalized nanostars, while in a second step, nanostars functionalized with nanobodies were used.

Three concentrations of the various blocking agent were tested in the same order as the SAM functionalization (1.2 & 2.4 mM) and an up to ten-time higher concentration (12 mM). Looking at the LSPR band shift for the concentrations of 1.2 and 2.4 mM, only a small red-shift of the LSPR band was measured for all blocking agents. For the highest concentrations (12 mM), a.blue shift of the LSPR band was detected for the small molecules (SHOH, SHCOOH and SHNH), while a red shift was noticed for the larger PEG molecules (Figure 4.6; Appendix 1). In addition,

a significant decrease of the hydrodynamic diameters in MES buffer was observed for all concentrations, when compared to the non-blocked nanostars.

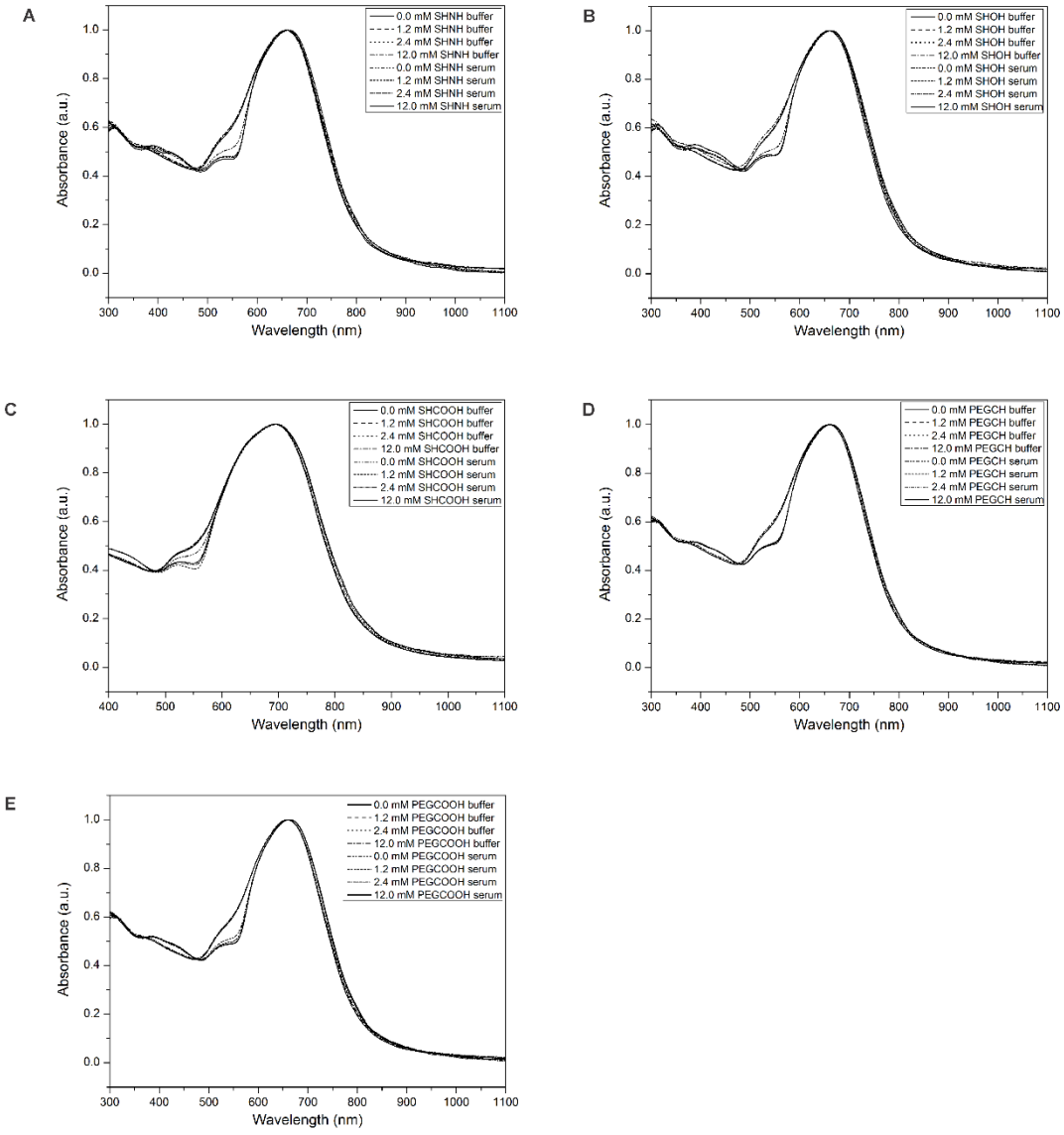

Figure 4.6 Normalized absorbance of the nanostars that are functionalized with the blocking agents SHNH (A), SHOH (B), SHCOOH (C), PEGCH (D) and PEHCOOH (E) for different concentrations (1,2 mM; 2,4 mM and 12 mM) in either MES-buffer or cell culture medium with serum.

Based on these initial finding, we chose to use a concentration of 2.4 mM for all subsequent experiments. At this functionalization concentration, the zetapotential showed either an increase or decrease when compared to the non-blocked, functionalized nanostars, depending on the end group of the agent (Table 4.2). While for positive and neutral groups (-OH, CH_3 and NH_2) a less anionic zetapotential was measured, the nanostars were slightly more anionic for carboxyl end groups of the blocking agents.

Table 4.2 Zetapotential given for the nanostars either non-blocked (MAL) or blocked with different types of molecules

	Zetapotential (mV)
MAL	-41.23 ± 2.13
SHNH	-34.92 ± 3.52
SHOH	- 37.37 ± 1.73
SHCOOH	-41.53 ± 1.53
PEGCOOH	- 40.67 ± 0.97
PEGCH	- 42.27 ± 1.25

Figure 4.7 shows the increase of hydrodynamic diameter when these nanostars are dissolved in cell culture medium with serum. The nanostars blocked with a PEG-containing blocking agent did not show any significant reduction of the protein corona as compared to the non-blocked nanostars (control). On the other hand, the nanostars that were blocked with the shorter molecules showed significantly reduced hydrodynamic diameters. The most pronounced effect was seen for the nanostars blocked with SHOH, showing only a hydrodynamic diameter increase of around 9 nm when comparing serum with non-serum containing medium

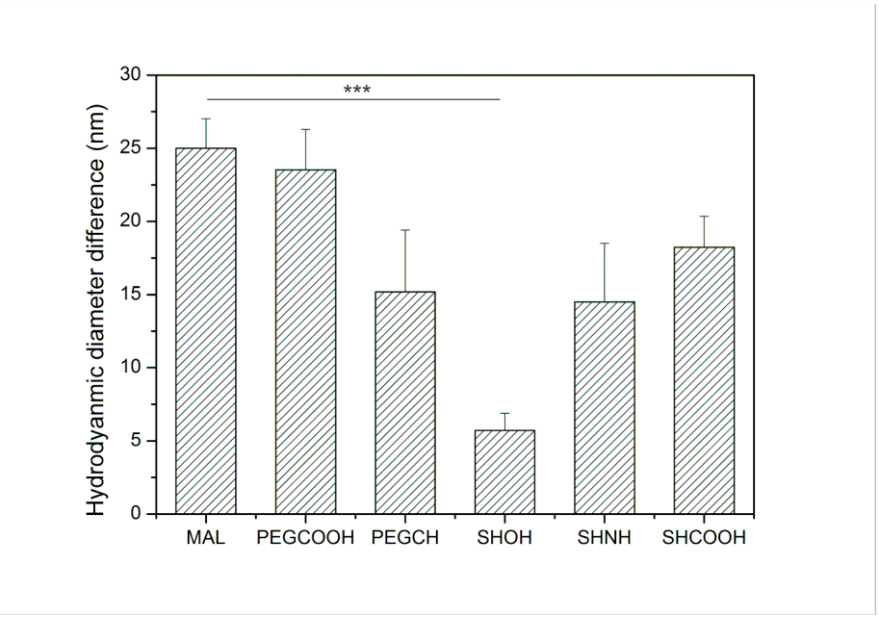

Figure 4.7 Hydrodynamic diameter difference shown for the difference nanostars - non-blocked or blocked – under serum-containing conditions compared to their hydrodynamic diameter in water (control)

4.3.4 In vitro visualization of active targeting using biofunctionalized nanostars.

To examine the effect of this blocking agent on the nanostar-cell interaction, the nanostars were incubated for 6 and 24h with the SKOV3 cells in medium containing serum. The darkfield images showed a reduced passive uptake for all blocked nanostars with subtle differences between the different blocking agents (Figure 4.8). The nanostars functionalized with SHCOOH or PEGCOOH showed the smallest reduction in uptake on the darkfield microscopy images, while SHOH showed the highest reduction in uptake after both 6 and 24h incubation (Figure 4.8). Using darkfield quantification, only a nanostar/cell mean signal intensity of 3.2 ± 1.2 % was measured for the SHOH functionalized nanostars compared to 8.8 ± 0.9 % for the non-blocked nanostars (Figure 4.9).

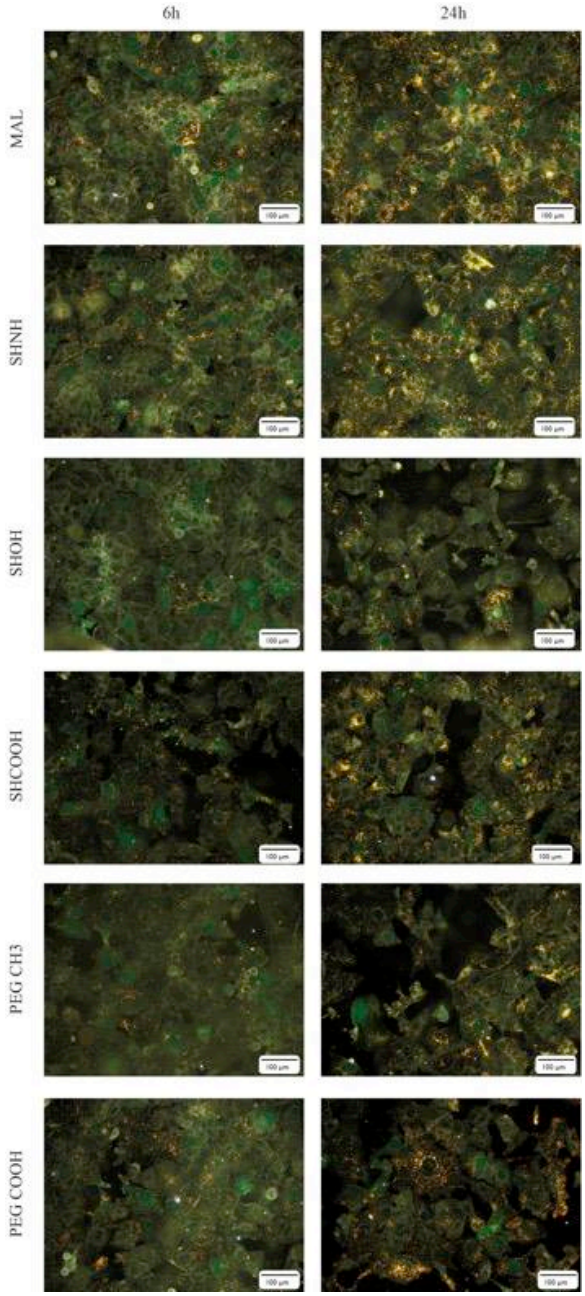

Figure 4.8 Darkfield images of SKOV3 cells incubated with the different (non-)blocked nanostars during 6 or 24 h of incubation

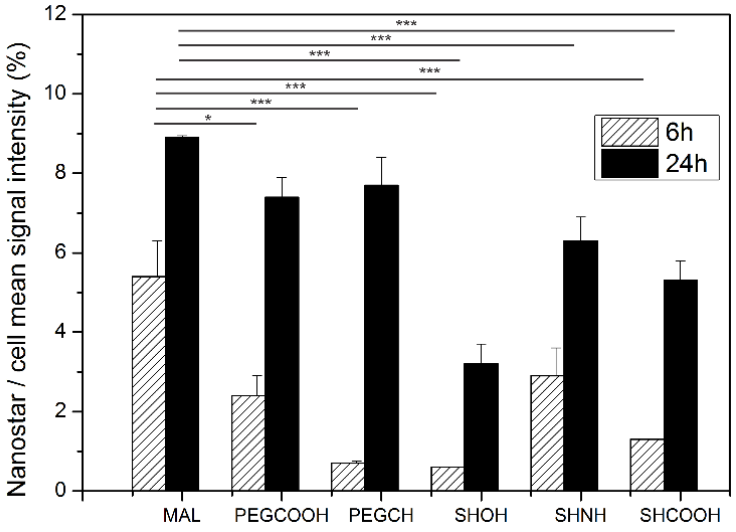

Figure 4.9 Nanostar/cell intensity plotted for different SKOV3 cells incubated with non-biofunctionalized nanostars either non-blocked or in the presence of a blocking agent.

4.3.5 In vitro visualization of active targeting using biofunctionalized nanostars.

Since blocking the nanostars with SHOH resulted in reduced hydrodynamic diameters, mainly due to a reduced protein corona, the next step was to examine the active targeting properties of the biofunctionalized nanostars blocked with this molecule. Nanobody-functionalized nanostars blocked with SHOH remained stable in water and in medium containing serum, as no broadening or diminishing of the LSPR band was seen (Figure 4.2). Also further functionalization with nanobodies did not influence the inhibition of protein corona by SHOH in cell culture media for both the SKOV3 and CHO tumor cells (Figure 4.10). Overall, the thickness of the protein corona was significantly reduced to a maximum size of 9 nm.

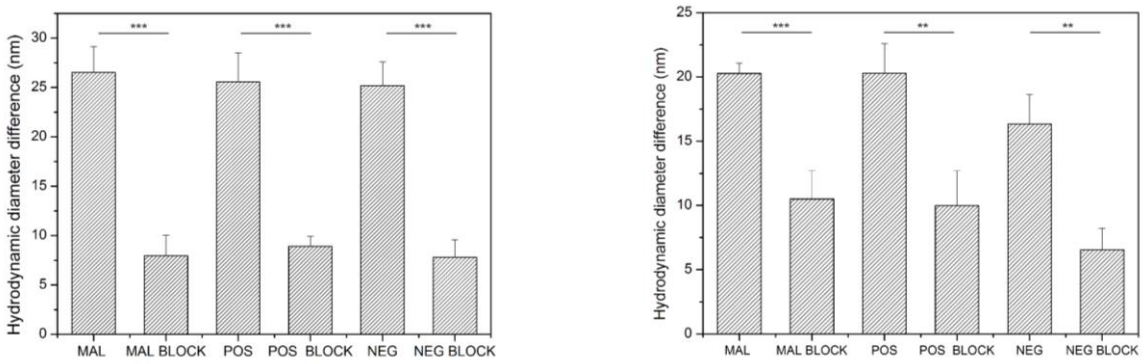

Figure 4.10 Differences in hydrodynamic diameters measured for the nanostars – biofunctionalized and/or blocked with SHOH - in cell culture medium containing serum compared to the hydrodynamic diameter measured in water. Data is shown for SKOV3 cell

When incubating tumor cells with these nanostars under serum-free conditions at a temperature of 4 °C, specific accumulation was seen using darkfield microscopy where a significant decrease of uptake was noticed for both the non-biofunctionalized and cAbBcII10 functionalized nanostars but not for the 2Rb17c functionalized nanostars (Figure 4.11). After incubating at a temperature of 37 °C in the absence of serum, the same specific intracellular uptake in the SKOV3 cells was observed for the 2Rb17-blocked nanostars. For the other two types of nanostars, almost no intracellular nanostar accumulation was observed. Performing the same experiments in medium containing serum, a specific accumulation of the 2Rb17c functionalized nanostars was seen inside the cells for both temperatures. The other two types of nanostars showed no accumulation inside the tumor cells, indicating a blocking of the formation of a protein corona which results in a successful active targeting. . As seen in Figure 4.12 almost no nanostar accumulation was detected in the CHO cells under none of the conditions tested (serum versus non-serum at a temperature of 4 and 37°C)., These results were confirmed after quantifying the intensities in the darkfield microscopy images (Figure 4.13).

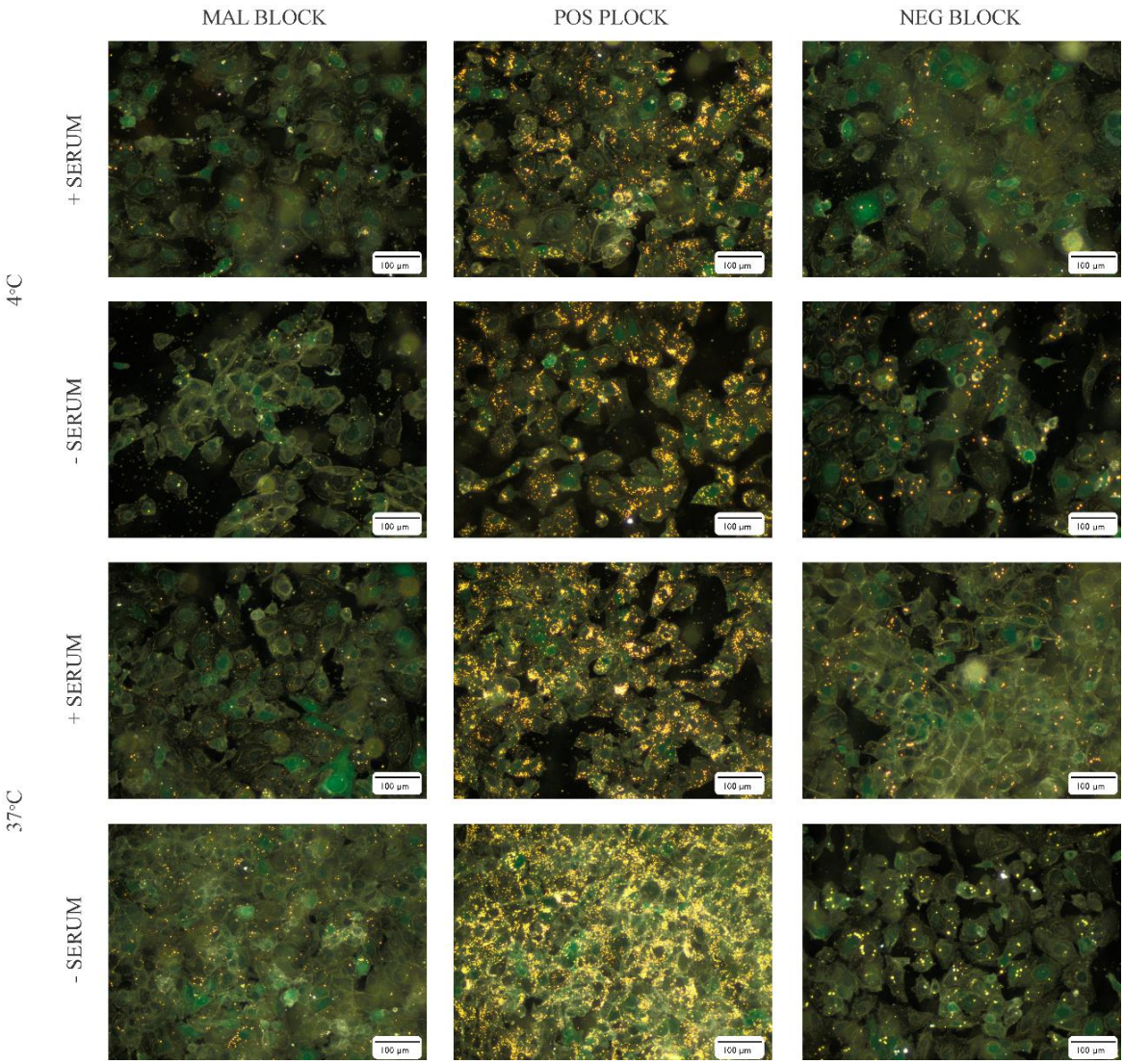

Figure 4.11 Darkfield microscopy images of SKOV3 cells incubated with either non-biofunctionalized nanostars (MAL), biofunctionalized with 2Rb17c (POS) or cAbcII10 (NEG). All nanostars were functionalized with the blocking agent SHOH.

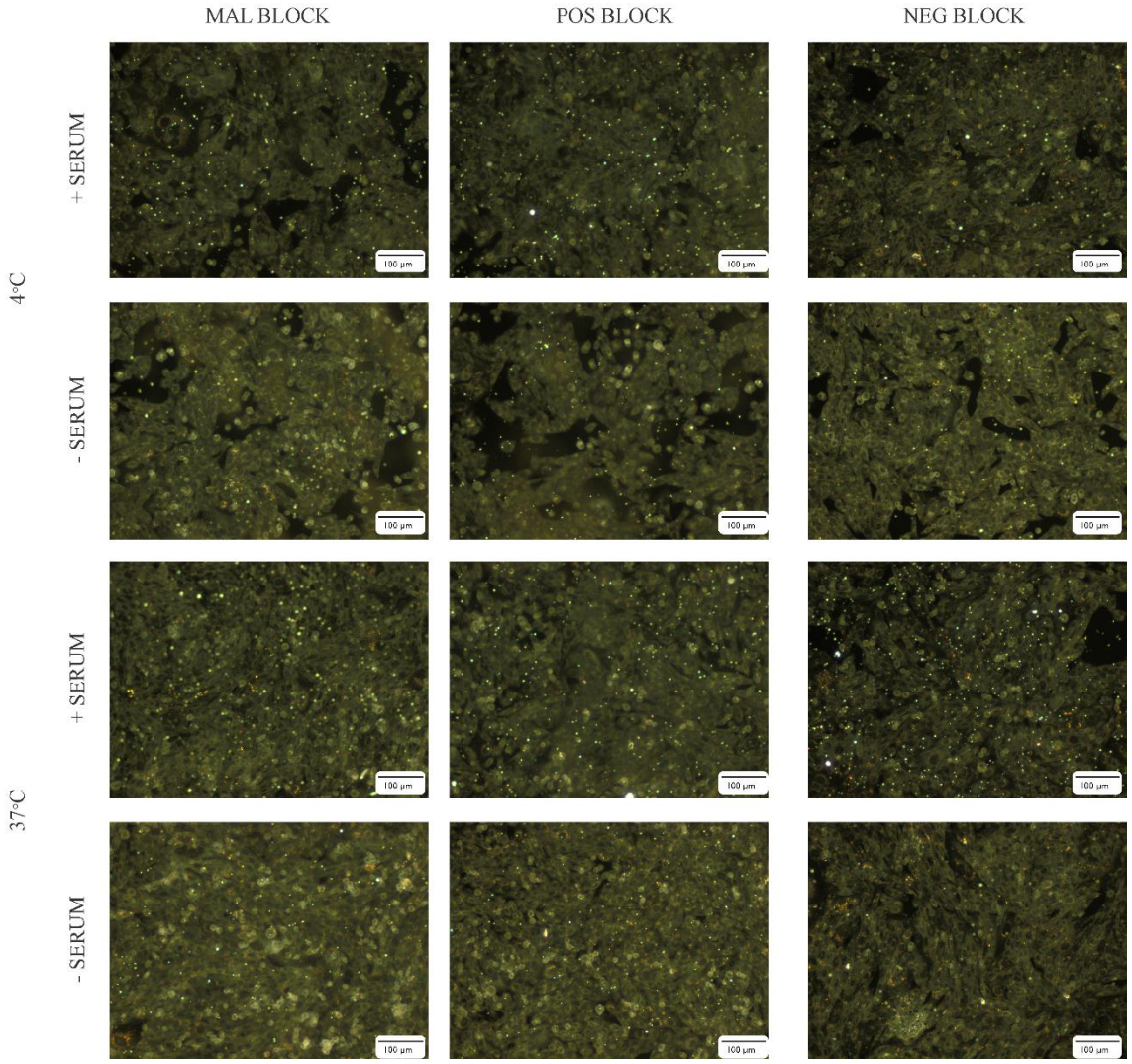

Figure 4.12 Darkfield microscopy images of CHO cells incubated with either non-biofunctionalized nanostars (MAL), biofunctionalized with 2Rb17c (POS) or cAbcII10 (NEG). All nanostars were functionalized with the blocking agent SHOH.

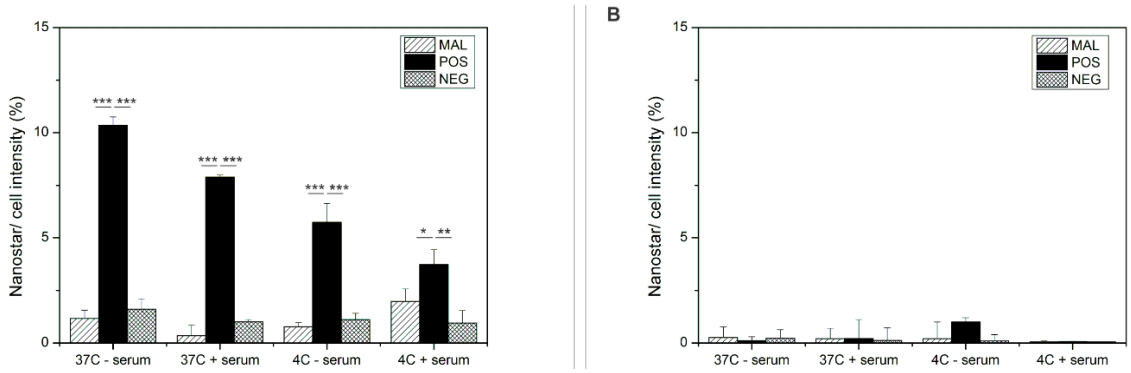

Figure 4.13 Nanostar/ cell intensity for SKOV3 cells (A) or CHO cells (B) incubated with either non-biofunctionalized nanostars (MAL), biofunctionalized with 2Rb17c (POS) and cAbcII10 (NEG) but all functionalized with blocking agent SHOH for different incubation conditions

4.3.6 In vivo imaging of biofunctionalized nanostars.

To verify the targeting capabilities *in vivo*, animals with a SKOV3 cell xenograft were intravenously injected with the blocked nanostars either biofunctionalized with 2Rb17c, cAbBcII10 or non-biofunctionalized as shown in Figure 4.14. By using PAI, the intratumoral accumulation of the nanostars (color coded in Figure 4.14 ; green pixels) was monitored and overlaid over the anatomical ultrasound image. Three hours after i.v. injection, some accumulation of the non-biofunctionalized nanostars (signal intensity: 0.042 ± 0.012 a.u.) was observed at the tumor border using PAI (Figure 4.14 . Top: Photoacoustic images overlaid on ultrasound images are shown for SKOV3 tumors before and after systemic injection (i.v.) of non-biofunctionalized nanostars (MAL) or biofunctionalized with either 2Rb17c (POS) or cAbcII10 (NEG). All nanostars were also blocked with SHOH. The PA signal of the nanostars is shown in green pixels. Bottom: Quantification of the PA signals. A much higher and also intratumoral accumulation was noticed for the 2Rb17c functionalized nanostars (signal intensity: 0.088 ± 0.023 a.u.) showing the *in vivo* targeting capabilities of these nanostars. The cAbBcII10 biofunctionalized nanostar showed almost no accumulation inside the tumor, even not around the tumor vasculature (0.006 ± 0.005 a.u.). As well some spatial overlap was noticed when distinguishing the overlapping nanostar and the oxyhemoglobin signal (Figure 4.15).

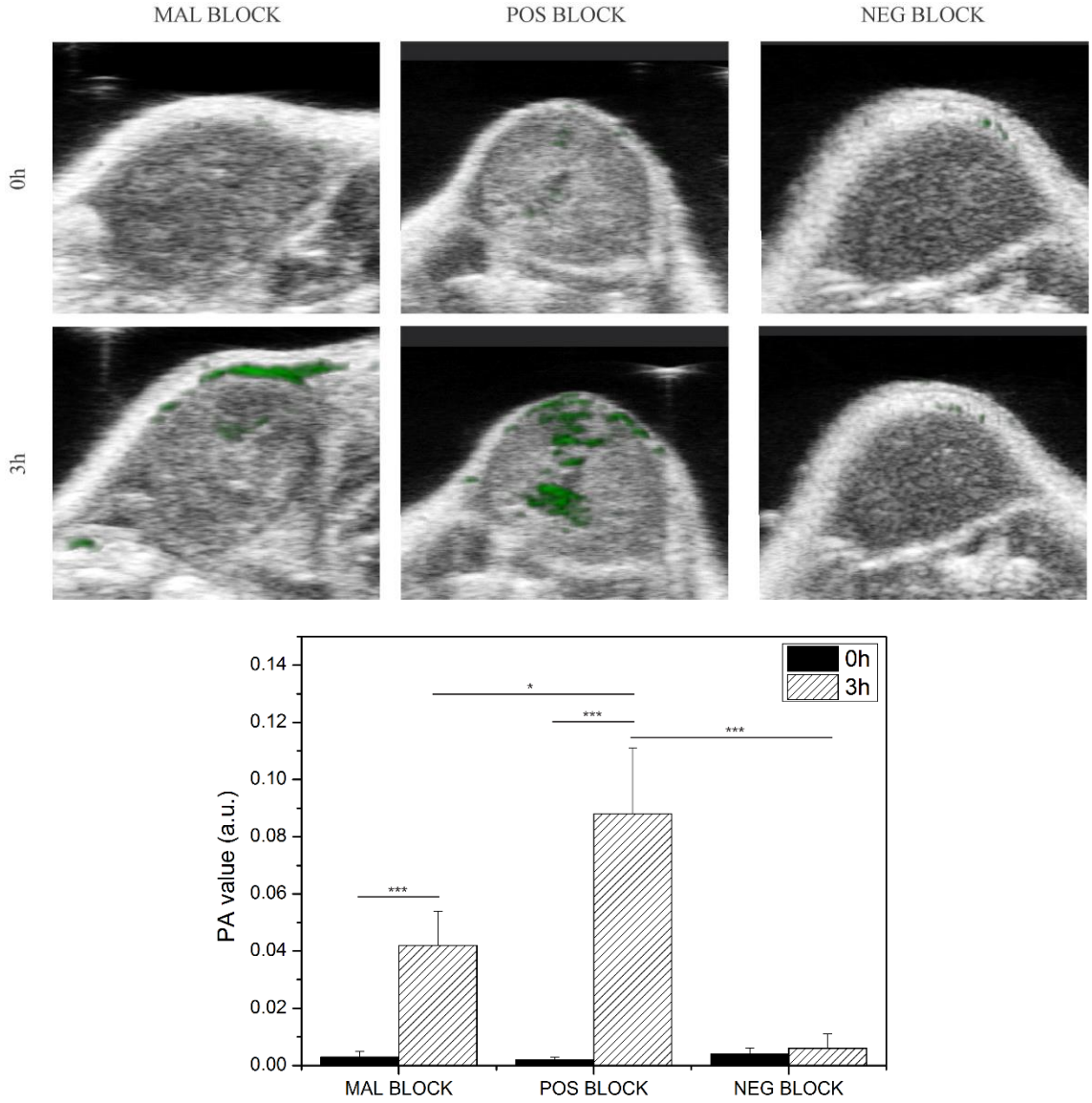

Figure 4.14 . Top: Photoacoustic images overlaid on ultrasound images are shown for SKOV3 tumors before and after systemic injection (i.v.) of non-biofunctionalized nanostars (MAL) or biofunctionalized with either 2Rb17c (POS) or cAbcII10 (NEG). All nanostars were also blocked with SHOH. The PA signal of the nanostars is shown in green pixels. Bottom: Quantification of the PA signals.

To cross-validate the photoacoustic imaging results, the tumors and other organs (liver, spleen, heart and kidney) were isolated immediately after PAI. Organs were fixed and sectioned for darkfield microscopy. As depicted in Figure 4.16, no nanostars were detectable in the tumor after

systematic injection of cAbBcII10 functionalized nanostars. For the non-biofunctionalized nanostars, some nanostars could be visualized at the tumor border. For the 2Rb17c functionalized nanostars, some nanostars were present at the tumor border and even more were found in and around vesicular structures within the tumor. For the other studied tissues, no differences were observed in nanostar accumulation between the specifically labeled versus control nanostars (Figure 4.17). As expected, the liver and spleen showed high accumulation of nanostars, whereas almost no nanostars were detectable in the heart and kidney.

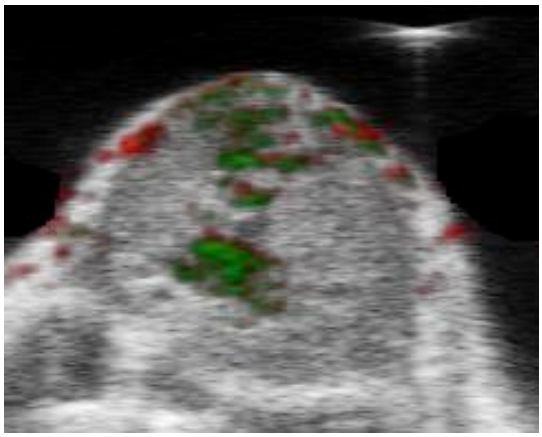

Figure 4.15 Photoacoustic image of the SKOV3 tumor after spectral unmixing to visualize oxyhemoglobine (red) and the 2Rb17c functionalized nanostars, blocked with SHOH (green). By spectral unmixing, a distinction between the oxyhemoglobine and nanostars signal was made

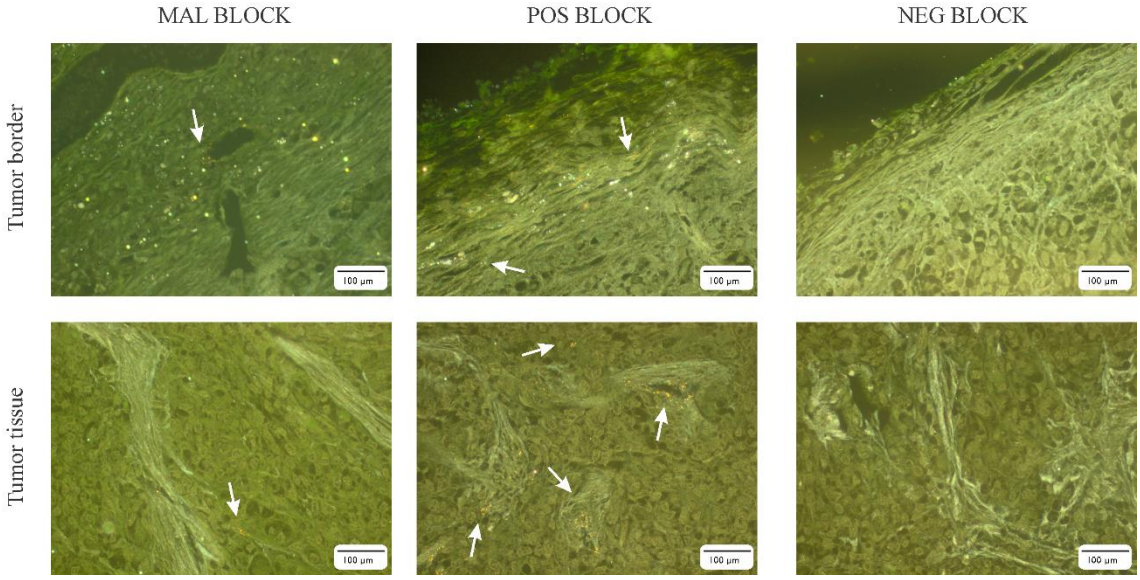

Figure 4.16 Representative *ex vivo* darkfield images of the tumor tissue section after systemic injection of the 2Rb17c functionalized nanostars (POS), cAbcII10 functionalized nanostars (NEG) and non-biofunctionalized nanostars (all functionalized with the blocking agent SHOH). The nanostars are visualized as yellow spots inside the tumor tissue

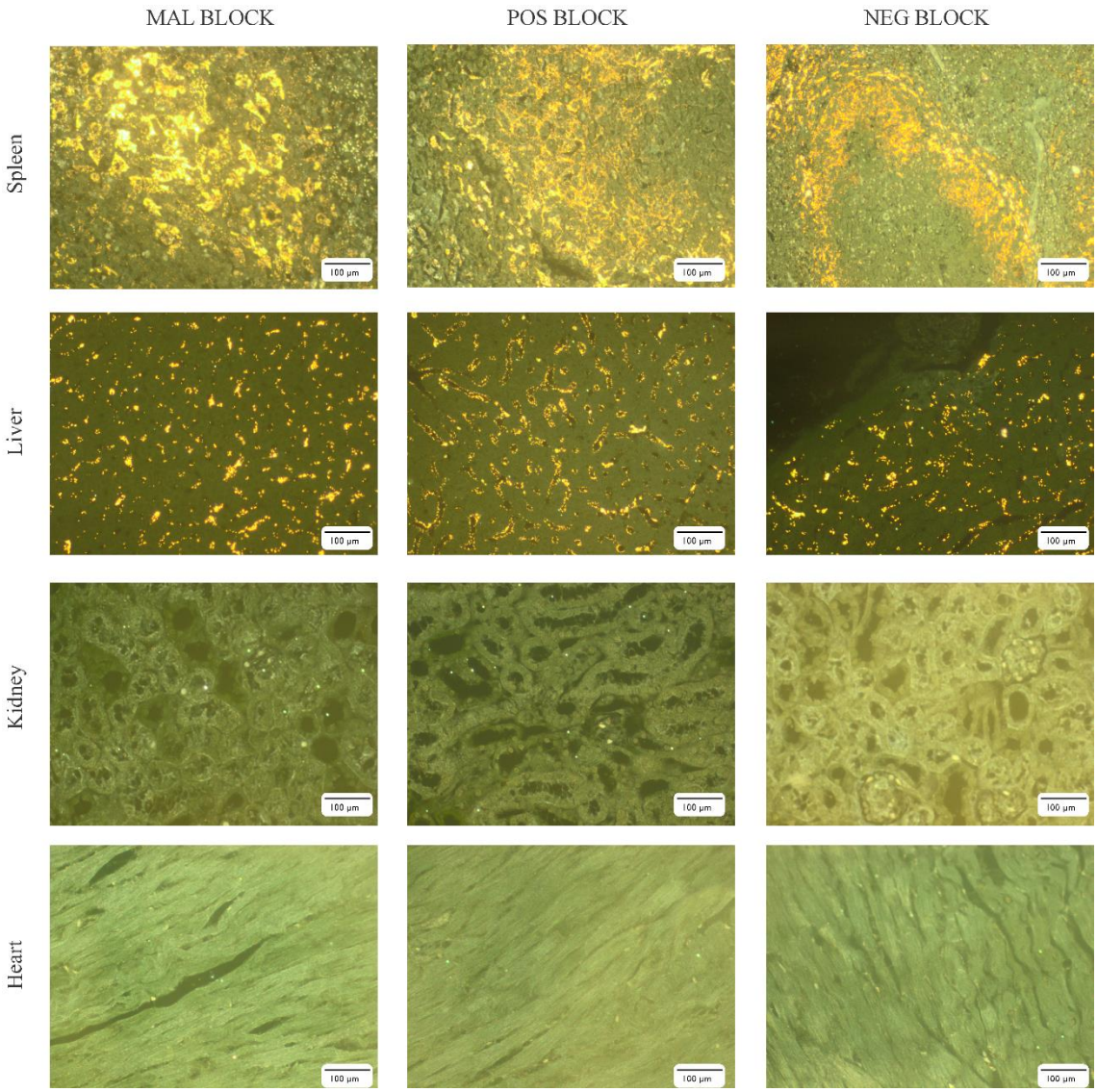

Figure 4.17 *Ex vivo* darkfield images of sections of different organs of mice that were systemically injected with the 2Rb17c functionalized nanostars (POS), cAbcII10 functionalized nanostars (NEG) and non-biofunctionalized nanostars (all were functionalized with the blocking agent SHOH). The nanostars are visualized as yellow spots inside the tumor tissue.

4.4 Discussion

For future clinical applications in oncology with gold and other nanoparticles it will be crucial to demonstrate under *in vivo* conditions their ability of an effective tumor targeting. This remains still a huge hurdle in nanoparticle research where variable success for active targeting has been indicated[3,9,18,33]. While many properties of nanoparticles have been optimized over the years, 'the biggest hurdle in the next years' that has been identified is the formation of a protein corona *in vivo*[19]. We have developed here a viable strategy to decrease the thickness of the protein corona to overcome steric hindrance and to improve the active targeting.

In this study, two different types of nanobodies, either 2Rb17c, targeting the HER2 receptor on the ovarian cancer cell line SKOV3, or cAbBcII10 as a control nanobody were used. For both, a maximum optimal biofunctionalization concentration was deducted where at higher concentrations the nanostars aggregated due to the osmotion depletion effect[34]. This effect describes that the nanostars exert a repellent force on the charged nanobodies in suspension due to the presence of the PEG units in the coating layer. Above a critical nanobody concentration, the nanostars will aggregate since the repellent force is too large, which induces attraction forces between the nanostars.

Either the fraction of the monomer or the dimer nanobodies were used for nanostar biofunctionalization. Between these two different formats of nanobodies, a difference in maximum optimal biofunctionalization concentration was observed. With the monomer fraction, a higher biofunctionalization concentration could be added to the nanostar's suspension compared to the reduced dimer fraction. This was probably due to the previously described capping of the monomer's reactive thiol group during the nanobody synthesis, which resulted in less reactive monomers that could bind to the nanostars[24]. Since similar trends in the LSPR shift, hydrodynamic diameter changes and zetapotential were seen for the two different kinds of batches, we can assume that there was no difference between the nanostars that have been coupled either by the monomer or the reduced dimer nanobody coupling on these nanostars. The successful coupling of the nanobodies was confirmed by active targeting under serum-free conditions for the nanostars that were functionalized with 2Rb17c nanobodies.

For *in vivo* applications, it is crucial that the nanostars are able to specifically target HER2-expressing tumor cells in the presence of serum. When incubating the nanostars in serum containing medium even at a low temperatures, which will block passive targeting, no active uptake could be detected in the tumor cells. This absence of active targeting in serum conditions has been attributed to the formation of a protein corona around these nanostars as seen by the hydrodynamic diameter increase. The biological ligands on the nanostars are believe to be completely capped by serum proteins, inhibiting the possibility to bind with receptors on tumor cells[19].

It has been shown that the maleimide end is responsible of the formation of a protein corona around the nanoparticles[18]. Maleimide end groups are highly reactive at neutral pH. By blocking the maleimide end groups using compounds with an end-standing thiol group, the formation of a protein corona could potentially be reduced. Different molecules were evaluated for their capacity to affect the thickness of the protein corona by changing the charge of the end group or the build-in of a PEG-chain in the molecule[13]. SHOH (2-mercaptoethanol) showed the strongest decrease in the hydrodynamic diameter of the gold nanostars, most likely due to their neutral end group and small size[10]. Compared to these neutral end groups, charged groups show a less significant decrease in protein corona thickness likely due to an electrostatic interactions with biomolecules present in serum[35]. However, compared to the non-blocked nanostars with a maleimide end group, a decrease in the protein corona is still visible due to a lower reactivity of these charged end groups. Unexpectedly, blocking ligands with a PEGylated back-chain showed less protein corona reduction compared to the shorter molecules. This could possibly be caused by the steric hindrance during functionalizing the nanostars with the PEGylated blocking agents where less blocking molecules may have reacted with the maleimide end groups. As a result, there could still be reactive maleimide end-groups on these nanostars.

In vitro evaluation in SKOV3 cell culture allowed verifying whether the changed thickness of the protein corona had an effect on passive uptake. Indeed, uptake of nanostars blocked with the short molecules was lowest for the SHOH functionalized nanostars confirming the effect of a reduced protein corona [13,36] Similarly, the PEGylated molecules showed less reduction of uptake, probably due to the non-significant decrease of the protein corona. The optimal thickness may be subtle as

the total absence of a protein corona was reported to again increase the nanoparticle uptake[16]. Overall, the size of the protein corona may define the degree of passive uptake by tumor cells, which could also have an influence on the recognition by the reticuloendothelial system[37].

When using the optimal SHOH blocking strategy on the biofunctionalized nanostars, nanobody-specific uptake was realized in both non-serum and serum conditions at both low and high temperatures. The successful active targeting is most likely due to combined effect of decreased passive targeting and a decreased protein corona thickness[18]. The latter avoids sterically hindrance of the nanobodies enabling receptor recognition on the tumor cells. Although the increase of the hydrodynamic diameter may predict failure of active targeting under *in vitro* conditions, the situation could be completely different *in vivo* where the reticuloendothelial system other serum proteins and the EPR effect must be taken into account[30].

We could demonstrate that reducing the size of the protein corona size and increasing *in vitro* targeting capabilities are indeed good predictors for active targeting of nanostars under *in vivo* conditions. PAI and *ex vivo* darkfield microscopy confirmed intratumoral accumulation of 2Rb17c-functionalized nanostars, both inside the tumor and on the tumor periphery. The tumor periphery is characterized by high vascular density and lower intratumoral pressure, resulting in higher nanostars accumulation[38]. However, nanostars always accumulated near blood vessels due to the low penetration of these nanostars inside the tumor tissue. This is mainly caused by the relatively large size and anionic charges of the nanostars[39]. The non-biofunctionalized nanostars showed also a significant but lower uptake in the tumor periphery. Due to the blocking of the protein corona formation, nanostars are less recognized by the RES[36], resulting in a longer blood retention time, which increases the possibility that nanoparticles accumulate into the tumor. The active targeting was further confirmed by cAbBcII10-functionalized nanostars that did not show any uptake inside the tumor.

Several hurdles have yet to be overcome to improve active targeting and intratumoral accumulation compared to a passive targeting strategy. It has to be kept in mind that active targeting still depends on the EPR effect for the nanoparticles to diffuse into the tumor[2]. This also applies to the HER2 receptor targeted in this study. Only due to the EPR effect nanostars can reach the SKOV3 tumor cells. By targeting a receptor on the vasculature like the vascular

epidermal growth factor (VEGFR), an enhanced uptake of the nanoparticles inside the tumor is possible since the EPR effect is no requirement[40]. Another important factor for a successful therapy is to minimize the nanoparticle uptake by the RES, which resulted in high concentrations of gold nanostars inside the liver and spleen as also seen in our study[41]. This could potentially have a long-term toxic effect on these tissues, such as by changing the cell morphology or genetic alterations[42,43].

4.5 Conclusion

Taken together, we show the specificity of the 2Rb17c-functionalized nanostars to HER2 expressing tumor cells by decreasing the size of the protein corona using 2-mercaptoethanol as a blocking agent. Hereby, the biological identity of the nanostars was tailored so that active targeting could be achieved in vitro and in vivo making them an ideal candidate for later theranostic applications. Further research, including a better understanding of the nanoparticle-RES interaction may help to transfer these nanostars to a clinical theranostic application in the future

5 DEVELOPMENT OF RAMAN-LABELED NANOSTARS AS A BIOCOMPATIBLE TUMOR CONTRAST AGENT FOR *IN VIVO* SERS IMAGING.

5.1 Introduction

Diagnosing cancer at an early stage by improving imaging approaches is key to increase the survival of cancer patients. Optical imaging techniques such as SERS have gained interest in this field where the optical selectivity is used for better tumor tissue discrimination. SERS exploits the enhanced Raman scattering by bringing a Raman molecule close to a metal surface such as on gold nanoparticles. Hereby an enhancement by $10^{10\text{-}12}$ of the Raman signal could be realized. As a consequence, SERS has made its introduction into the biomedical field since the technique enables the very sensitive detection of molecules and easy discrimination based on a fingerprint spectrum.

On one hand, SERS has been introduced for the detection of analytes in a label-free manner where they interact with the metal surface. On the other hand, SERS-active structures that have the Raman label is already coupled to the surface, are used to follow the interaction of these structures up to the level of single molecule detection. Examples of the successful use of the Raman labeling approach are the discrimination of different cell types, viruses and other lab-on-a-chip applications**.** Also *in vivo,* these SERS-active structures, such as nanorods or nanospheres have shown his potential to discriminate these labels inside different tissues[119,193–19776,95].

Aiming at cancer diagnosis with the aid of SERS, gold nanoparticles have been extensively studied as potential ideal SERS contrast agents [76,95,96,99,195,198–200]. The criteria for an ideal SERS contrast agent is to have a high enhancement factor of the Raman signal by creating locally high electric fields. Hereby several shapes have been introduced ranging from nanorods, nanostars, dimers etc[76]. All these nanoparticles are equipped with sharp tips generating these high electric fields upon irradiation[201]. In particular, nanostars have several sharp tips, and are as a consequence efficient surfaces / carriers for SERS labels which enables detection down to the pM level[202,203]. *In vitro* applications of sensitive SERS imaging using nanostars have been demonstrated for the study of cellular pathways, intracellular pH sensing or the detection of specific cells in histology sections[93,94,98]. Despite their high potential, nanostars have not been used as an *in vivo* SERS contrast agent despite their higher sensitivity compared to nanorods or nanospheres.

In our approach, we aim to use the high sensitivity of these nanostars as an *in vivo* cancer diagnostic agent. Hereto, the nanostars have to be decorated with SERS reporters. This is not straightforward since changing the stabilizing coating of the nanostars may affect their stability in physiological conditions. Using *in vitro* experiments, we evaluate the properties and the potential of SERS-labeled nanostars to passively target tumor cells as described in chapter 2. By an *in vivo* passive targeting strategy blocking the protein corona with 2-mercapto ethanol as in chapter 4, SERS used to evaluate tthe nanostars will end up in the tumor by the EPR effect[19,153]. Using SERS, the passive uptake of nanostars in the tumor and biodistribution is evaluated which is crucial for later theranostic purposes.

5.2 Materials and methods

5.2.1 Nanostars synthesis and functionalization

Nanostars synthesis has been executed as explained in chapter 2. After synthesis the nanostars were suspended in 10 mL and functionalized with 1 mL of the desiring DTNB concentration after adding 100 µL NaOH (0.5 M). After 1,5h of shaking, the nanostars suspension was centrifuged for 60 min at 4500 rpm, the supernatans discarded and the nanostars pellet resuspended in water. Then the nanostars were functionalized with the SAM ($HS–(CH_2)_{11}–(O–CH_2–CH_2)_6–O–CH_2–MAL)_2$ according to the protocol in chapter 2. After functionalization, the nanostars were characterized using UV-Vis absorption spectroscopy, DLS and Zetapotential measurement, in water. To evaluate their SERS imaging capabilities, the nanostars were either dried on a silica wafer overnight or loaded into an agar phantom (as described in chapter 2).

5.2.2 Darkfield microscopy analysis of cell- nanostar interaction.

As in chapter 2, tumor cells (SKOV3) were seeded by 150 000 cells per well in a 12-well plate to study the cell-nanostars interaction. After 24h, nanostars with different SAMs ($2.3x10^{10}$ particles in 1 mL) were added to the cells and incubated for 3h, 6h and 24h. After washing with PBS, these cells were again incubated overnight with fresh medium. After trypsinization, 300 µL of the cell suspension were either acid digested for ICP-OES or plated on a coverslip in 1 mL of fresh medium in a 12 well plate and incubated overnight. After fixation with 4% paraformaldehyde in PBS (4% PFA), these coverslips were mounted on a glass slide and visualized with darkfield microscopy or the Raman microscope type alpha 300R, WITec, Ulm, Germany**).** Darkfield microscopy images were quantified by using CoralPaint software where yellow pixels (nanostars) and green pixels (tumor cells) were detected from the images and converted into white pixels (Figure M1). The amount of white pixels was calculated for both conditions where afterwards the amount of nanostars pixels was divided by the amount of cell pixels to result in the nanostars/cell density. These glass slides were also imaged using the Raman microscope (785 nm, 40mW, 5 sec integration time, raster of 40x40 µm).

5.2.3 Evaluation of in vivo biodistribution using ICP-OES and darkfield microscopy.

Athymic nude mice were, as in chapter 2, injected subcutaneously with tumor cells. We let the tumors grow for 2-3 weeks. Afterwards, nanostars (200 µl, 2,3 mg Au/ml) were injected via the tail vein (n = 4 for each condition). After 24h the mice were imaged with Raman microscopy. After this imaging slot the animals were sacrificed, transcardially perfused with 4%PFA and the heart, the liver, the spleen, the kidneys and the tumors were dissected and stored in PBS with 0,1% sodiumazide (Sigma). These organs and tumors were ex vivo visualized using the Raman Witeq microscope using the same settings as *in vivo*. For darkfield microscopy, the dissected organs were embedded in paraffin to make sections of 7 µm thickness with a microtome (HM360, Prosan). The sections were placed on microscope slides and deparaffinized before darkfield microscopy.

5.3 Results

5.3.1 Nanostar synthesis and functionalization with SERS label

The nanostars are designed as described previously in chapter 2, resulting in nanostars absorbing the light in the NIR region. As a SERS label, DTNB was chosen, since it has a high Raman cross section and is used extensively in literature[204–208]. To find the optimal DTNB concentration for functionalizing the nanostars with this label, a concentration range (10 mM; 1 mM; 0.1 mM; 0.01 mM and 0.001mM) was added on these nanostars. An optimal concentration of 0.1 mM was chosen since it did not affect the stability of the nanostars and it showed a stable LSPR peak shift and hydrodynamic diameter increase. A broadening and decrease of intensity of the LSPR band occurred at higher concentrations, indicating instability of the nanostars (Figure 5.1). This instability was confirmed by a too large hydrodynamic diameter increase of 21.04 ± 0.84 nm when functionalizing the nanostars with 10 mM DTNB (Table 5.1). Moreover starting at a functionalization concentration of 0.1 mM a second band appeared in the absorption spectrum around 412 nm due to the creation of 3-thio-6-nitrobenzoate (TNB^-) molecules in the solution. The successful functionalization of these nanostars with the DTNB molecule was confirmed by a

red shift of this absorption band and increase in the hydrodynamic diameter by 8.14 ± 0.63 nm. With only the DTNB label on the nanostar surface, the nanostars are only stable in salt concentrations up to 0.03 M NaCl.

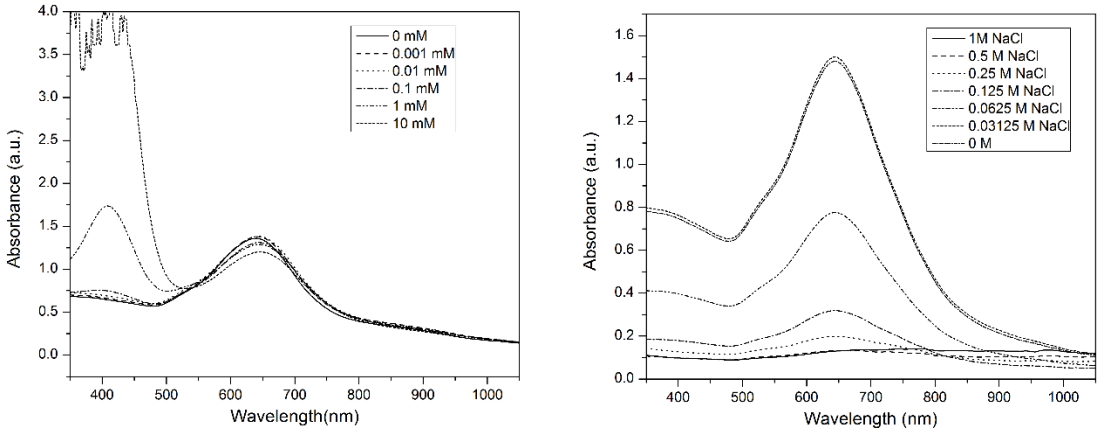

Figure 5.1 Left: UV-Vis of the nanostars functionalized with a concentration range of DTNB. A second band is appearing due to the formation of TNB-. Right: LSPR band of the nanostars functionalized with 0.1 mM DTNB for different salt concentrations, showing the nanostar instability by a decrease in intensity.

Table 5.1. For a given set of DTNB concentration the LSPR band shift, hydrodynamic diameter increase is reported together with the maximum salt concentration where the nanostars remain in suspension.

DTNB (mM)	LSPR peak shift	Hydrodynamic diameter increase (nm)	Maximum salt concentration (M)
0.001	1.33 ± 0.58	6.35 ± 1.77	0.06 M
0.01	2.33 ± 0.59	9.39 ± 1.49	0.06 M
0.1	3.67 ± 1.15	8.14 ± 0.63	0.03 M
1	4.33 ± 1.53	7.04 ± 0.61	0.03 M
10	4.67 ± 1.53	21.04 ± 0.84	0.03 M

For increasing the stability in physiological conditions, the nanostars were afterwards functionalized with the SAM as described in chapter 2. As with the DTNB functionalization, a red-shift in the LSPR band (5.30 ± 1.66 nm) and increase in hydrodynamic diameter (6.12 ± 1.57 nm) was measured after SAM functionalization (Figure 5.2). These nanostars with a SAM molecule, the nanostars are stable up to a concentration of 1M NaCl (Figure 5.2). After functionalization the nanostars had an anionic zetapotential of -33.3 ± 3.4 mV.

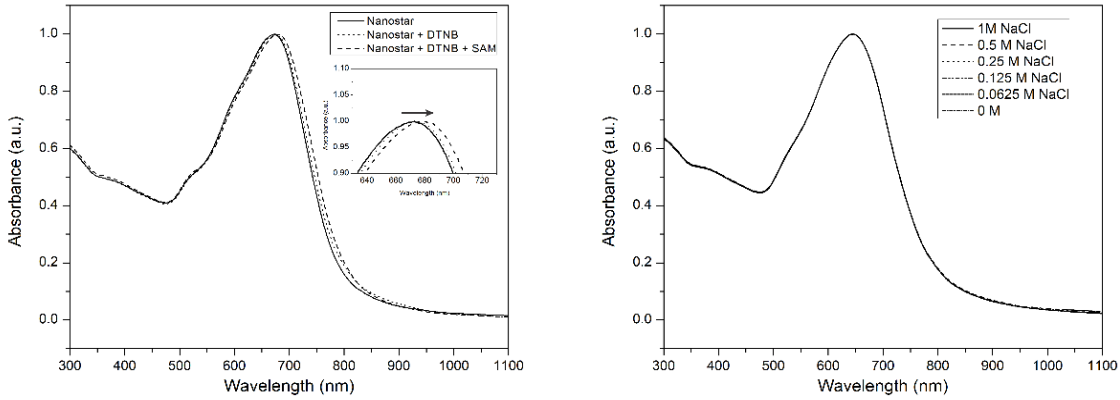

Figure 5.2 Left: UV-Vis spectrum of the 'naked' nanostars, nanostars functionalized with 0.1 mM DTNB and with a SAM. As inset the LSPR band shift to the NIR region due to the binding of these molecules to the nanostar surface. Right: LSPR band of the nanostars functionalized with DTNB and SAM for different salt concentrations showing no instability.

Due to the SAM functionalization, the SAM's molecules could replace the Raman labels on the nanostars. Therefore the SERS contrast generation (785 nm, 40 mW and 10 sec integration time) was measured of dried nanostars on a silica wafer using either nanostars functionalized with DTNB and SAM or nanostars only functionalized with the SAM. As shown in Figure 5.3, a clear DTNB spectrum could be deducted from the nanostars functionalized with DTNB and SAM with the highest intensity at 1333 cm^{-1}. This confirms that the SAM molecule has not replaced all the DTNB molecules on the nanostars. Conversely, for the nanostars SAM no SERS signal could be measured.

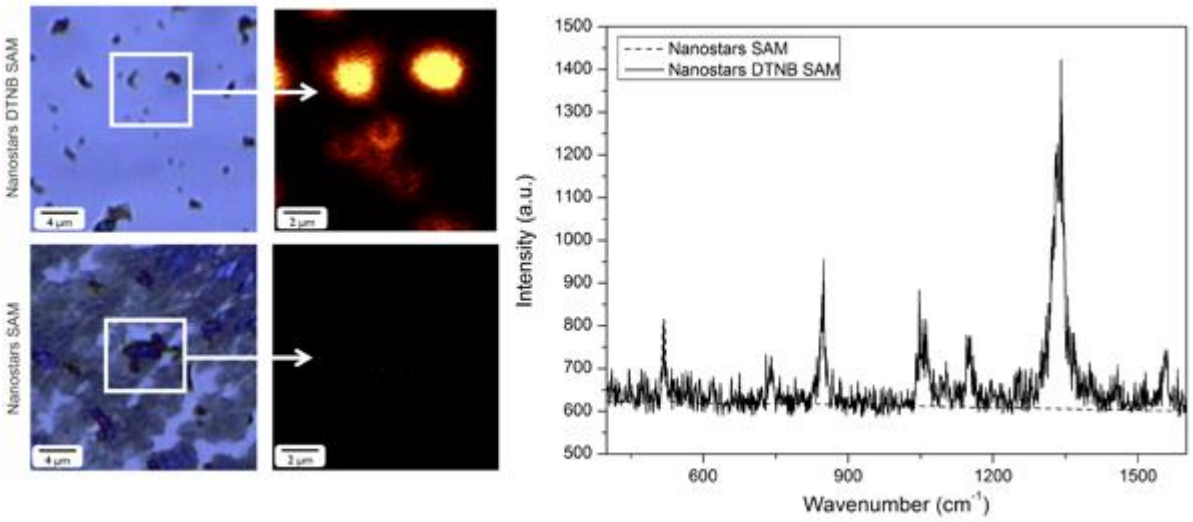

Figure 5.3 Left: Brightfield microscopy images of the nanostars dried on a silica wafer where the SERS signal intensity at 1333 cm^{-1} is visualized in the zoom picture. Right: SERS spectrum of the corresponding nanostars either labeled with DTNB and SAM or only functionalized with the SAM molecule.

To evaluate the SERS capabilities of the nanostars for later *in vivo* applications, the sensitivity of SERS detection for the different nanostars concentrations (250, 125, 62.5, 31.3, 15.7 µM Au*)* has been evaluated after loading them into an agar phantom. During SERS imaging they are irradiated with a continuous laser (785 nm, 40 mW and 60 sec integration time). Within the phantom, for all nanostar concentrations, a detectable DTNB spectrum was measured with the maximum intensity at 1333 cm^{-1} (Figure 5.4). When plotting the intensity at 1333 cm^{-1} for the different gold concentrations, a LOD a linear relation was deducted between the Raman intensity and gold concentration. Using a linear fit, a LOD of 13 µM was calculated.

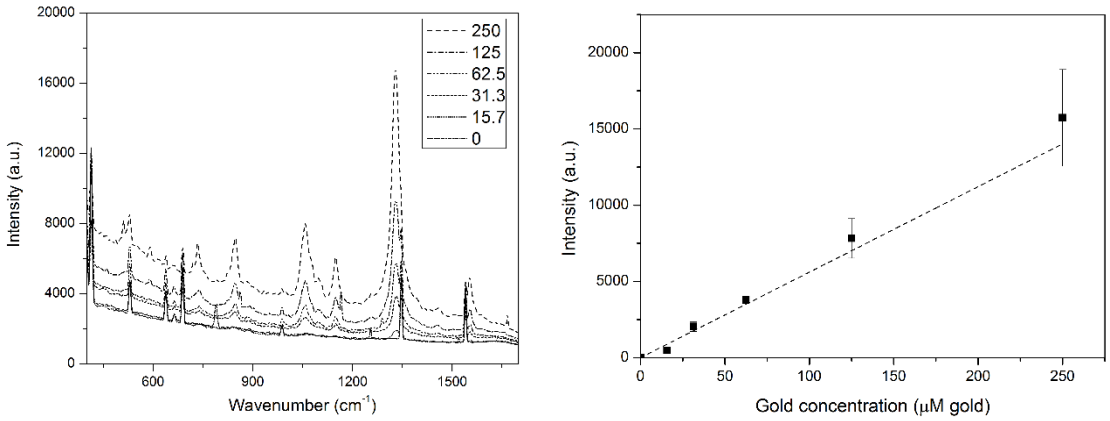

Figure 4. SERS spectrum for different concentration (*μ*M Au) of the SERS labeled nanostars embedded 2mm deep in in an agar phantom. As inset the intensity at 1333 cm-1 plotted for the different concentrations.

5.3.2 SERS to visualize the in vitro uptake in tumor cells

Prior to using these nanostars *in vivo*, the *in vitro* uptake by the tumor cells was studied. After 3, 6 and 24h incubation, the increase in intracellular uptake of the nanostars was visualized by dark-field microscopy and quantified by ICP-OES. The gold quantification increased over time, going from 0.3 ± 0.9 pg Au/cell after 3h, 4.4 ± 0.68 pg Au/cell after 6h, up to 8.05 ± 1.1 pg Au/cell measured after 24h, 2, compared to 0.1 ± 0.05 pg Au/cell for the control cells using ICP-OES. Darkfield microscopy confirmed the intracellular uptake of nanostars, by visualizing nanostars inside the cells (Figure 5.4).

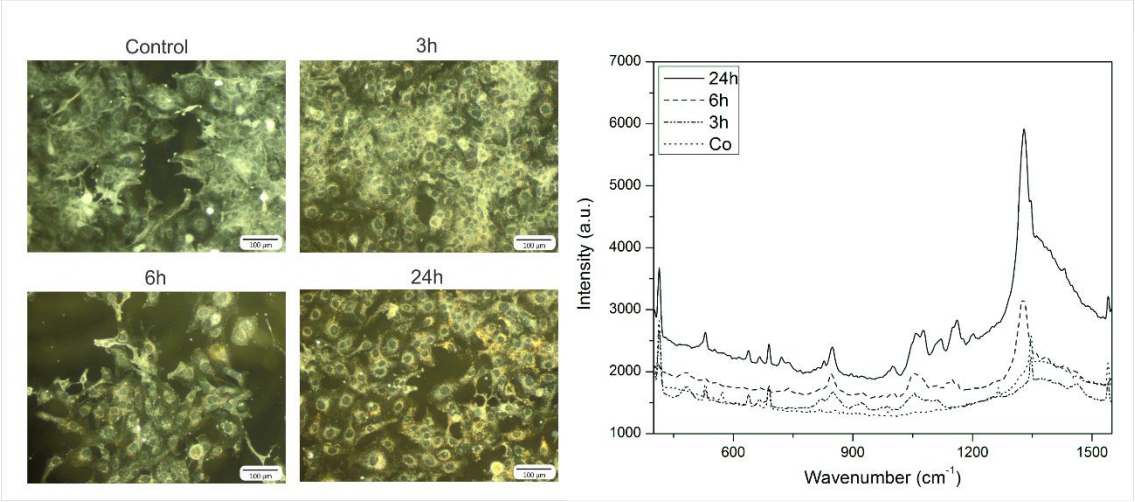

Figure 5.4 Left: Darkfield microscopy pictures where an increase of gold nanostars inside the tumor cells is visualized over time Right: SERS spectrum of the corresponding cells labeled with nanostars, showing the highest intensity peak at 1333 cm^{-1}

On these time points, we collected the SERS spectra of the cultured cells by a raster scan with a resolution of 1 µm. At these conditions only SERS spectrums were measured since no normal Raman spectrum was measured with the control cells. When acquiring the SERS spectra of the cells labeled for 6 and 24h with the nanostars, a clear SERS signal was measured (Figure 5.4). For these two a distinct peak at 1333 cm^{-1} was detected that was absent for the control spectrum. After 24h labeling, the highest SERS peak was observed. Together with the higher Au concentration measured after 24h of incubation, this indicates that the SERS label did not detach from the nanostars after intracellular uptake. After 3h, no distinct Raman peak was measured, however having some nanostars inside the tumor cells as indicated by the dark field microscopy picture. Moreover, for all conditions a significant background signal is observed between 1300-1400 cm^{-1} that can be contributed to the glass coverslip. This background signal could be reduced by using quartz coverslips, thereby increasing the potential *in vitro* sensitivity. Since the nanostars

are located in specific endosomes as shown in chapter 2, these spots of the nanostars could be mapped inside the cells, confirming the intracellular uptake (Figure 5.5).

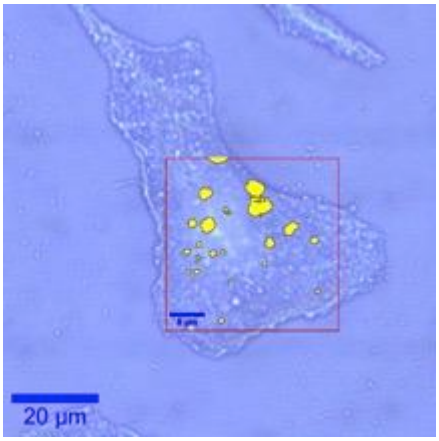

Figure 5.5 Brightfield image of a tumor cell overlaid by a SERS intensity image where at high intensities at the wavenumber of 1333 cm^{-1} yellow spots are visualized.

5.3.3 SERS as an in vivo imaging tool using nanostars as contrast agents

To validate the *in vivo* SERS imaging capabilities of these nanostars as a cancer diagnostic agent, the Raman labeled nanostars were i.v. injected to passively target the tumor. 3h after i.v. injection of these nanostars, the SERS spectrum of the tumor, liver and control tissue were deducted with the Witec microscope. Both the SERS spectrum of the liver and tumor are shown after background and control tissue deduction in Figure 5.6. For both of them a clear SERS band at 1333 cm^{-1} was visualized showing the accumulation of these nanostars in the respective organs. Due to the recognition of the nanostars by the RES a high SERS signal was observed in liver with an intense peak at 1333 cm^{-1}. Next to the liver, some of the nanostars accumulated in the tumor with a corresponding DTNB SERS spectrum. However due to the inhomogeneous accumulation of the nanostars inside the tumor, not at all points a detectable SERS spectrum was observed.

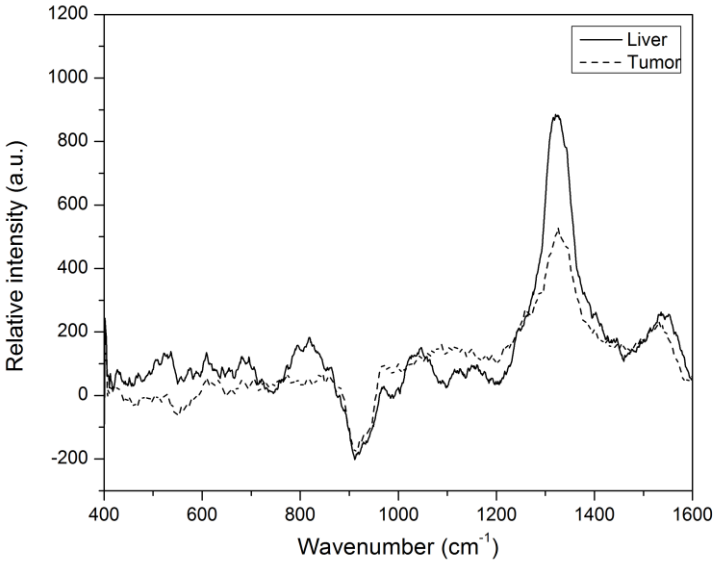

Figure 5.6 SERS spectrum of the liver and tumor 3 hours after i.v. injection of the nanostar where the background and control tissue have been subtracted. For both a clear peak at 1333 cm^{-1} was visible.

After sacrificing the animals, several organs were examined to evaluate their nanostar accumulation and corresponding SERS signal *ex vivo* (Figure 5.7). By ex vivo darkfield imaging of the organs, a clear nanostar accumulation was observed in the liver, spleen and tumor confirming the *ex vivo* SERS signal observations (Figure 5.7). No nanostars were visualized in the kidney and heart, corresponding to a background SERS spectrum. Regarding the tumor, the nanostars seem to preferentially accumulate in its periphery due to a higher vascular density. As a consequence, only at these locations a SERS signal was measured while in the tumor mass itself almost no SERS signal was measured.

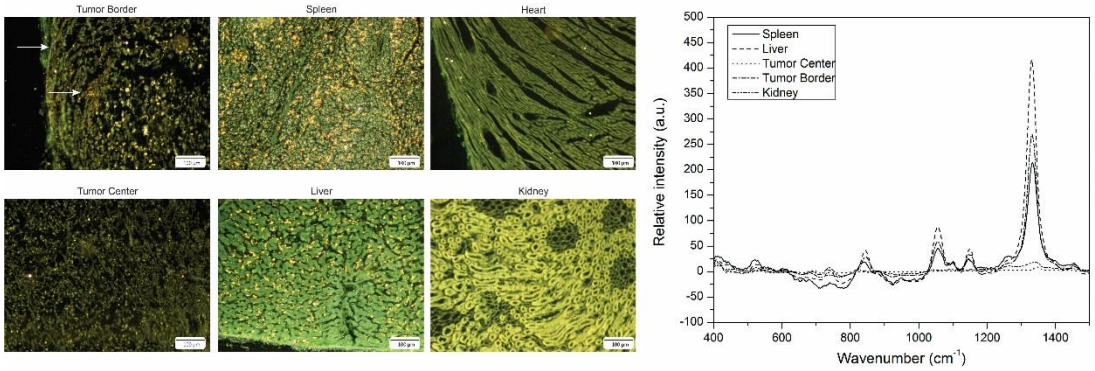

Figure 5.7 Left: Darkfield images of the different tissues where nanostars (gold spots) were clearly visualized inside the liver, spleen and in less amount at the tumor border. Right: SERS spectra of the different tissues where a DTNB spectrum was observed for the spleen, liver and tumor border.

5.3.4 Discussion

Due to its unique fingerprint Raman spectra, SERS is recently emerging as one of the most promising tools for *in vivo* biosensing and imaging. By changing the shape, different types of SERS labeled gold structures have been introduced and described in the literature. However the focus for *in vivo* use has been mainly on the use of nanorods and nanospheres. To the best of our knowledge, the use of gold nanostars as an *in vivo* diagnostic agent for cancer have never been addressed before. In this manuscript we proved applicability of these nanostars as an *in vivo* diagnostic agent using SERS. By functionalizing the nanostars with the DTNB label, these nanostars could be followed intracellular *in vitro* and on tissue level *in vivo*.

Realizing this opportunity of SERS imaging using nanostars, the functionalization condition of the nanostars with the Raman label must be examined. An important criteria is the maximum DTNB concentration of 0.1 mM where we proved that at higher concentrations the nanostars became unstable due to the osmotion depletion effect ref. Starting from this functionalization concentration we believe that the nanostars are fully covered with DTNB, resulting in negative charged 3-thio-6-nitrobenzoate (TNB^-) in the solution. As has been discussed in chapter 4, these negative molecules in the suspension will induce osmotic depletion inducing the instability of the nanostars. The creation of TNB^- molecules is confirmed by an absorbance band around 412 nm

that we measured starting from a concentration of 0.1 mM. An extra SAM functionalization step made this nanostars applicable for SERS detection in physiological conditions.

A crucial parameter for high sensitive imaging is the LOD of these nanostars in phantom conditions. Hereby they showed a LOD of 13 µM which is higher compared to previous reported LODs[64,209,210]. Several reasons must be taking into account fort his higher concentration such as the embedding under an agar phantom layer of 2 mm agar layer mimicking the *in vivo* conditions, which decreases the irradiation effectiveness. Another reason is the mismatch between the laser wavelength and the plasmon absorption band (785 vs 680 nm). In this way the field at the tips of the nanostars is not the strongest resulting in a smaller enhancement of the DTNB Raman signal. Moreover, this sensitivity could be increased by incorporating the SERS label itself into the molecule of the SAM, covering the complete nanoparticle with this Raman label[205]. Another strategy is to have built-in hot spots in the particle itself, which can increase the SERS signal by $10^{3\text{-}4}$ [211–213].

However, with this LOD, the nanostars could be easily intracellularly visualized using SERS as confirmed by ICP-OES and darkfield microscopy. Hereby we established that a minimum concentration of 4.4 pg Au/cell is necessary to visualize the nanostars inside the cells. At higher concentrations a non-linear relation was noticed between the gold concentration and SERS signal intensity. While for ICP-OES an increase of 82 % gold per cell was measured between 6 and 24h, a higher SERS signal increase of 135 % was measured. As the nanostars concentrations show a linear relationship with the Raman signal, this non-linear relation is due to the creation of hot spots of the nanostars[194]. The nanostars will aggregate inside the acidic endosomal structures inside the cells, which will create these hot-spots structures. Looking at the nanostars accumulation itself a lower intracellular nanostars concentration was measured compared to the results in chapter 1 and 2. Hereby the less anionic zetapotential could have an influence on this decrease in intracellular uptake.

The use of nanostars has been shown as an *in vivo* diagnostic agent for cancer. Still, not at all locations of the tumor, a detectable SERS signal was measured due to a low extravasation of these nanostars inside the tumor. Hereby the anionic charges and size decreases the penetration of these

nanostars inside the tumor tissues. By functionalizing these nanostars with a biological ligand as in chapter 4, their tumor accumulation could be enhanced inside the tumor.

Since SERS is limited by a light penetration depth of only 1-2 cm, this imaging modality can be used for tumor detection after i.v. injection[76,100,118]. SERS can be combined with CT or PAI in a multimodal imaging approach. By using these other techniques a full body and 3D image of the tumor with the nanoparticle signal could be provided, which is not possible with SERS alone. Still new techniques are envisioned to use SERS as a 2D imaging tool having fast scanning times by using a Raman microscope. For theranostic purposes these nanostars could be used as a therapeutic agent for either PTT, by increasing the tumor temperature to a lethal level for the tumor, or photodynamic therapy, by creating singlet oxygen atoms which are toxic for tumor cells [92,99,100,212,214]. SERS may Even be used as an aid for surgical removal benefitting from the high Raman contrast imaging capabilities. SERS shows a high potential for applicability during surgery to define the tumor boundary, which is perfectly feasible within the 1-2 cm light penetration limits of SERS imaging[124]. Moreover, nanostars will accumulate preferentially at the tumor periphery delineating the tumor border during imaging as we showed.

Conclusion

In summary, physiological stable SERS-labeled nanostars show stable SERS signal in agar phantoms down to a concentration of 12 μM. *In vitro* these nanostars are easily taken up by tumor cells where they end up intracellularly in endosomal structures. SERS imaging confirms this intracellular specific uptake inside cells where a minimum concentration of 4.4 pg Au/cell could be detected. Using these unique properties, SERS signal from the nanostars could be detected in the liver and tumor after simple i.v. injection. The presence of the nanostars has been confirmed by *ex vivo* SERS measurements combined with darkfield imaging. Taken together, based on our first *in vivo* results, we demonstrate that nanostars can be used as a diagnostic agent for cancer using SERS as a cheap optical imaging technique, with future applications in guidance for surgical removal.

6 CONCLUSION

For the development of new therapeutic and diagnostic techniques of tumor masses, bionanotechnology and more specifically the novel nanoparticles is rapidly evolving as a promising technique[169]. One of the driving forces towards nanoparticles is the possibility to combine imaging and therapeutic capabilities on one specific nanoparticle[3]. Although many hurdles still have to be overcome before these nanoparticles may be used as a clinical agent in oncology.

A huge variety of nanoparticles is currently studied with a focus on a better theranostic agent against cancer. A well-known class of nanoparticles are gold nanoparticles with their specific plasmonic properties[29]. These local plasmonic capacities are the basis for their theranostic potential. Dependent on the shape of gold nanoparticles, the plasmonic capacity changes as for nanorods, nanostars or nanocages compared to nanospheres[74,201]. While nanocages and nanorods are well described in literature, nanostars as a theranostic agent against cancer are still not fully developed. However, these nanostars shows a much more intense plasmonic effect compared to other particles, resulting in better imaging and therapeutic capabilities[209].

Within the field of gold nanoparticles, some are already in the clinical trial phase, but still many questions remain unanswered to predict the success of these nanoparticles as a theranostic agent[3].

One of the main hurdles is the cell/ receptor-specific targeting efficiency of the nanoparticles due to the formation of a protein corona *in vivo*.

The goal of this work was to establish a nanobody-functionalized gold nanostar targeting HER2-positive tumor cells to overcome the protein corona problem. Using the intense plasmonic properties of nanostars, this could result in an effective theranostic agent for CT, PAI and SERS imaging as well as for PTT. In a first part of this work, it was our goal to study the effectiveness of the nanostars as a theranostic agent using CT, PAI, SERS and PTT (Chapter 2 and 5). In a second part, we studied the passive and active targeting capabilities of these nanostars *in vitro* and *in vivo* (Chapter 3 and 4). Here, we showed that the interaction of the nanostars with surrounding proteins to form a protein corona plays a crucial role for targeting efficiency.

In Chapter 2, gold nanostars were successfully synthesized and functionalized with a stabilizing SAM layer. Crucial is that these nanostars fulfill the *in vivo* requirements as their plasmon band must be in the NIR region, their hydrodynamic diameter size has to be below 100 nm and they must maintain their stability under physiological conditions. It was shown by reducing the gold salt addition rate to 12.5 µL/min, that synthesized nanostars fulfilled these first requirements (plasmon band around 674.3 ± 8.3 nm and hydrodynamic diameter of 75.0 ± 5.6 nm). After functionalization with the SAM molecules, these nanostars had an increased stability under physiological conditions.

The imaging capabilities and therapeutic effectiveness of nanoparticles depends on their interactions with the targeted cells. In chapter 2, we showed that the gold nanostars showed a linear intracellular uptake by time, reaching to a plateau phase after 12h. After 24h, an intracellular gold concentration of 11.28 ± 0.82 pg Au/cell was measured, with particles ending up in vesicular structures, which was visualized by TEM. These results clearly demonstrate that anionic charged nanostars with a hydrodynamic diameter below 100 nm are easily taken up by the targeted tumor cells.

Due to this high cellular uptake, the nanostars can be used as a contrast agent using CT or PAI and as a photothermal therapeutic agent as demonstrated in chapter 2. Their capabilities to generate contrast in CT and PAI correlated exponentially with the intracellular gold concentration

where a higher LOD was calculated for PAI then for CT. This exponential growth in contrast-to-background is not only due to a higher intracellular gold concentration but also due to the aggregation of the nanostars inside the tumor cells. For therapy, the IC_{50} value is the most sensitive parameter to determine the therapeutic effectiveness. Our gold nanostars showed an IC_{50} of 5.8 pg Au/cell, which corresponds to 150 k nanostars/cells. Another parameter to determine the therapeutic effectiveness is the laser power used to induce specific PTT. Here our power of 2 W/cm^2 is slightly lower than those determined for nanorods, or nanocages, again demonstrating the effectiveness of gold nanostars[105,115]. As a consequence, we can propose that nanostars shows slightly better theranostic capabilities. Still this also depends on the cellular interaction, combination with different therapeutic techniques etc.

The ultimate test of theranostic properties of nanoparticles has to be performed *in vivo* since the situation from a physiological and cellular point is completely different compared to *in vitro* validations. This was performed by a proof of concept study where the nanostars were intratumoral injected. After injection, the nanostars showed an intense contrast in the tumor using both PAI and CT. Still a higher CNR was measured for PAI compared to CT, showing the higher sensitivity of this imaging method. For *in vivo* PTT, the laser conditions were optimized where a maximum laser power of 3.14 W/cm^2 and a minimum gold concentration of 2.5 µM was necessary to result in an effective PTT. Using BLI, MRI and histology, a significant PTT was confirmed but regrowth of the tumor occurred after several days. This indicates that combination with other therapeutic approaches might be necessary.

In the last chapter, the SERS imaging capabilities of the nanostars were studied using DTNB-labeled nanostars. SERS is based on the enhanced inelastic scattering by a Raman-active label close to the gold surface[88]. As a consequence, this technique could be used as a new optical imaging technique for monitoring the formation and therapy of tumors using gold nanoparticles. Compared to PA and CT, no LOD could be calculated due to the imaging set-up. Still, SERS can be used as an imaging tool to visualize the location of the nanostars with high precision inside the cells, showing the specificity of this imaging technique. After i.v. injection of nanostars, SERS signal was measured in the liver and tumor region, confirming the location of the nanostars. Since the technique is based on optical imaging with a low penetration depth, it will have potential for translation into the clinic mainly as an imaging tool for tumor resection during surgery[76].

Having the imaging and therapeutic properties optimized and quantified, a next step was to determine the targeting efficiency of functionalized gold nanostars *in vitro* and *in vivo*. Two targeting strategies have been described in the literature, either passive targeting using the inherent characteristics of the tumor, or active targeting. In Chapter 3, passive targeting has been studied using anionic nanostars with a different end group (MAL, MALOH or COOH). Using these nanostars under physiological conditions, an increase in hydrodynamic diameter was measured due to the formation of a protein corona on the nanostar's surface. The protein corona is composed of several biological molecules dependent on the serum and nanoparticle characteristics as described before[215]. Moreover, we measured a difference in the thickness of the protein corona with the largest corona formed for nanostars with a maleimide end group and the lowest for nanostars with a COOH end group. This further supports the hypothesis that the thickness of protein corona depends on the reactivity of the end group. In contrary to literature, we see the highest uptake for nanostars with a thick protein corona compared to the nanostars with almost no protein corona[161]. The reason for this is still unclear to us, indicating the need for a more into detail research on the protein corona. The difference in the end group of the SAM layer has also an effect on the *in vivo* biodistribution of the gold nanostars. Due to the protein corona, the nanostars SAM MAL were immediately taken up by the RES and ended up in the liver and spleen, whereas the nanostars SAM COOH showed a lower uptake in the liver/spleen. Almost no nanostars were observed in the tumor, showing a non-effective PTT after i.v. administration.

In Chapter 4, the active targeting of tumor cells with nanobody functionalized nanostars was studied. After biofunctionalization, these nanostars showed no specific cell uptake *in vitro* where the protein corona inhibited the interaction of the nanobodies with the HER2 receptors on the tumor cells. We believe this protein corona was generated due to the free maleimide end groups on the nanoparticles. Different agents were studied to chemically block the free maleimide groups where 2-mercaptoethanol showed the best inhibition on the formation of a protein corona. These nanostars showed less passive uptake by tumor cells, proving our theory that the protein corona may induce an inhibition of cell specific uptake. Also due this reduced protein corona, these nanostars are also less anionic resulting in a less favored cell uptake. Using 2-mercaptoethanol to block the free maleimide groups after biofunctionalization, a specific uptake inside the tumor

cells expressing HER2 receptors was noticed. No specific uptake was noticed when the nanostars were biofunctionalized with the control nanobody or on a negative cell line with no HER2 receptors. As a consequence, the protein corona is the limiting factor for active targeting of nanostars to tumor cells. This theory was also tested *in vivo*. Using PAI, specific active targeting was confirmed, where HER2-targeting nanostars are located close to the vasculature of the tumor. As a consequence, these nanostars may be used as a specific theranostic agent for HER2 expressing tumor masses.

7 FUTURE PERSPECTIVES.

With this multidisciplinary research, we aimed to improve the potential of gold nanostars as a theranostic agent for HER2 expressing tumor masses. Although, substantial progress has been made, there are still some remaining hurdles in order to implement this technique as a standard of care technique for cancer diagnosis and treatment.

The synthesis of the nanostars is still batch dependent where several factors like time procedure to the compound masses play a big role on the resulted synthesized nanostars. Taken together with the functionalization, it takes approximately three days to produce a biofunctionalized nanobody where the free maleimide groups are blocked with 2-mercaptoethanol. Changing the synthesis set-up by using a flow reactor could result in a higher production yield and better defined batches. Also the follow-up of functionalization could be done in a different order by adding extra molecules one by one on the nanostar surface. By linking the nanobody, the SAM molecule and 2-mercaptoethanol beforehand could increase the functionalization efficiency due to a higher nanobody loading on the nanostar surface. Before clinical testing, an automated synthesis and functionalization of the nanostar production under possibly GMP conditions must be realized, resulting in nanostars with less variability on size.

As stated in this thesis, the biggest hurdle is to optimize the right targeting strategies of the nanoparticles to the tumor. As have shown in the thesis, these targeting capabilities are dependent on so many factors as the nanoparticles characteristics (diameter, charge and material), to the set-up of the experiment. These nanoparticle can show *in vitro* high tumor accumulation where this situation can be completely different *in vivo* with almost no tumor uptake after i.v. administration. . Here the biological identity in serum, due to the protein corona, have a huge influence on targeting efficiency[140]. Several strategies have been studied to overcome this problem. While we developed a way to inhibit the formation of a protein corona, other studies showed that tailoring the protein corona may result in a better nanoparticle uptake by the tumor cells[179]. By studying the effect of the nanoparticle characteristics on the protein corona and the cellular uptake, a strategy per particle could be defined to overcome this problem. In addition to experimental data, the focus is changing to also include results from modelling the protein corona[178]. This could potentially result to a simulation method to design the most optimal nanoparticle. After the assessment of targeting strategies in xenograft models, it will also be necessary to validate them in allograft models to better simulate the situation in patients and hereby better predict outcome once moving to clinical trials

By overcoming the blockage of targeting ligands by the protein corona, the active targeting capacities also depends on the right choice of targeting molecule for active targeting. We have chosen the well characterized HER2 receptor of tumor cells. However, this receptor has the disadvantage that the particles still need to pass the blood barrier to reach the tumor cells. Here, the possibility of finding other target molecules should be considered in future studies. By choosing a vascular target as the vascular epidermal growth factor, the targeting efficiency could potentially be improved[57]. Still this targeting efficiency is dependent on the vascularization of the tumor. By promoting the vascular growth within the tumor, this targeting efficiency could be improved as has been showed for other drug molecules[216]. Not only reaching the target/ tumor should be taken into account, also the intratumoral distribution is an important criteria[217]. Here, the nanoparticle dimension and charge will play an important role. The mechanisms of intratumoral distribution of nanoparticles are not well understood and need to be evaluated further, as they will have an effect on the imaging and therapeutic effectiveness. The distribution of nanoparticles within a tumor is of some importance for tumor diagnosis but even more important for potential applications as theranostic agents. Crucial is to choose the right

combination of therapy and imaging technique for the specific tumor types. Among others, this will depend on the LOD and the depth penetration of an imaging or therapy technique. For example, the low depth penetration of SERS will only permit clinical applications like the intra-operative use during tumor resection. On the other hand, imaging sensitivity and contrast could be further increased by changing the design of the gold nanoparticles. Here, combining different materials on one nanoparticle could potentially increase the range of imaging techniques. For example, an iron nanoparticle with a gold layer could be potentially also used as a MRI contrast agent. On the therapeutic side, we are limited to tumors located under the skin or exposed during surgery due to the low laser penetration depth. To increase the therapeutic effectiveness, photodynamic therapy could still be combine with other therapies, such as temperature sensitive drug release[14,17].

Next to studying the targeting and theranostic capabilities, two important criteria's have not been touched in this thesis, namely possible long term toxicity and possible excretion of nanoparticles. As these nanoparticles are not biodegradable, they will stay in the tumor site. As a consequence, gold nanoparticles are to single time point applications. While the properties of nanoparticles used in this thesis have the right diameter for targeting and theranostic applications, they are less favorable to avoid excretion. Nanoparticles with a diameter larger than 10nm will not be excreted by the kidneys, but will mainly accumulate inside the liver and spleen[48]. Within the liver, they are taken up by the Kupffer cells, where most studies showed no short term toxicity within these cells. Still on long-term toxicity, more studies were generated that showed alteration in the genotype expression of these Kupffer cells loaded with gold nanoparticles[218]. As a consequence, these nanoparticles should be further intensively studied for long-term effects on different cell morphologic and gene expression parameters before clinical studies can be considered. The outcome of these studies will have a huge influence on the optimal nanoparticle characteristics for tumor targeting and therapy.

In conclusion, this PhD study emphasized on the theranostic capabilities of the gold nanostars and tried to overcome problems associated with the protein corona to achieve active targeting of tumor cells. More in depth research is needed on toxicity and long term distribution and stability to evaluate if these nanostars could be used as a theranostic agent in the clinic. Looking at the bigger

picture, more coordinated research is needed between centers to study the potential of (gold) nanoparticles as a theranostic agent. Every research center is trying to develop their own 'optimal' nanoparticle while huge questions about metal nanoparticles still need to be solved before developing a new theranostic agent. The next years will be crucial for nanoparticle research if they will have a potential as a standard of care technique for cancer diagnosis and treatment.

APPENDIX 1

	SHNH			SHOH			SHCOOH			PEGCOOH			PEGCH		
	1.2 mM	**2.4 mM**	**12 mM**	**1.2 mM**	**2.4 mM**	**12 mM**	**1.2 mM**	**2.4 mM**	**12 mM**	**1.2 mM**	**2.4 mM**	**12 mM**	**1.2 mM**	**2.4 mM**	**12 mM**
LSPR band shift (nm)	2.33 ± 0.29	2.67 ± 0.76	-0.50 ± 0.50	1.17 ± 0.29	2.00 ± 0.50	-0.83 ± 0.28	1.50 ± 0.50	1.67 ± 0.29	-0.17 ± 0.76	1.83 ± 0.29	2.00 ± 0.50	3.17 ± 0.76	1.67 ± 0.29	2.17 ± 0.29	1.67 ± 0.29
Hydrodynamic diameter change (nm)	-3.75 ± 0.86	-4.06 ± 1.09	-4.75 ± 0.54	-4.19 ± 1.50	- 3.85 ± 1.50	-4.04 ± 2.26	-3.45 ± 1.24	-4.05 ± 2.24	- 4.43 ± 2.02	-3.32 ± 1.15	-3.07 ± 0.87	-2.16 ± 2.60	-2.89 ± 1.17	-3.70 ± 1.07	-3.57 ± 1.81

BIBLIOGRAPHY

1. Ferlay, J. *et al*. Cancer incidence and mortality patterns in Europe: estimates for 40 countries in 2012. *Eur*. *J*. *Cancer* **49,** 1374–403 (2013).

2. Pysz, M. a, Gambhir, S. S. & Willmann, J. K. Molecular imaging: current status and emerging strategies. *Clin*. *Radiol*. **65,** 500–16 (2010).

3. Jokerst, J. V & Gambhir, S. S. Molecular imaging with theranostic nanoparticles. *Acc*. *Chem*. *Res*. **44,** 1050–60 (2011).

4. Hanahan, D., Weinberg, R. A. & Francisco, S. The Hallmarks of Cancer Review University of California at San Francisco. *Cell* **100,** 57–70 (2000).

5. Hanahan, D. & Weinberg, R. a. Hallmarks of cancer: the next generation. *Cell* **144,** 646–74 (2011).

6. Yarden, Y. Biology of HER2 and Its Importance in Breast Cancer. *Oncology* **61,** 1–13 (2001).

7. James, M. L. & Gambhir, S. S. A molecular imaging primer: modalities, imaging agents, and applications. *Physiol*. *Rev*. **92,** 897–965 (2012).

8. Frangioni, J. V. New technologies for human cancer imaging. *J*. *Clin*. *Oncol*. **26,** 4012–4021 (2008).

9. Janib, S. M., Moses, A. S. & MacKay, J. A. Imaging and drug delivery using theranostic nanoparticles. *Adv*. *Drug Deliv*. *Rev*. **62,** 1052–63 (2010).

10. Kelly, K. M., Dean, J., Comulada, W. S. & Lee, S. J. Breast cancer detection using automated whole breast ultrasound and mammography in radiographically dense breasts. *Eur*. *Radiol*. **20,** 734–742 (2010).

11. Kircher, M. F., Gambhir, S. S. & Grimm, J. Noninvasive cell-tracking methods. *Nat*. *Rev*. *Clin*. *Oncol*. **8,** 677–88 (2011).

12. Nagahara, L. A., Ferrari, M. & Grodzinski, P. Nanofunctional Materials in Cancer Research: Challenges, Novel Methods, and Emerging Applications. *MRS Bulletin* **34,** 406–414 (2009).

13. Hirsch, L. R. *et al*. Nanoshell-mediated near-infrared thermal therapy of tumors under magnetic resonance guidance. *Proc*. *Natl*. *Acad*. *Sci*. *U*. *S*. *A*. **100,** 13549–54 (2003).

14. Chen, W. & Zhang, J. Using nanoparticles to enable simultaneous radiation and photodynamic therapies for cancer treatment. *J. Nanosci. Nanotechnol.* **6,** 1159–1166 (2006).

15. Schnell, F. M. Chemotherapy-induced nausea and vomiting: the importance of acute antiemetic control. *Oncologist* **8,** 187–198 (2003).

16. Lepock, J. R. Cellular effects of hyperthermia: relevance to the minimum dose for thermal damage. *Int. J. Hyperthermia* **19,** 252–66 (2003).

17. You, J., Zhang, G. & C., L. Exceptionally High Payload of doxorubicin in hollow gold nanospheres for near-infrared light-triggered drug release. *ACS Nano* **4,** 1033–1041 (2010).

18. Xie, J., Lee, S. & Chen, X. Nanoparticle-based theranostic agents. *Adv. Drug Deliv. Rev.* **62,** 1064–79 (2010).

19. Bertrand, N., Wu, J., Xu, X., Kamaly, N. & Farokhzad, O. C. Cancer nanotechnology: The impact of passive and active targeting in the era of modern cancer biology. *Adv. Drug Deliv. Rev.* **66C,** 2–25 (2014).

20. Srivatsan, A. *et al*. Gold nanocage-photosensitizer conjugates for dual-modal image-guided enhanced photodynamic therapy. *Theranostics* **4,** 163–74 (2014).

21. Chen, H. *et al*. Multifunctional gold nanostar conjugates for tumor imaging and combined photothermal and chemo-therapy. *Theranostics* **3,** 633–49 (2013).

22. Thakor, A. S. & Gambhir, S. S. Nanooncology: the future of cancer diagnosis and therapy. *CA. Cancer J. Clin.* **63,** 395–418 (2013).

23. Warheit, D. B., Sayes, C. M., Reed, K. L. & Swain, K. A. Health effects related to nanoparticle exposures: Environmental, health and safety considerations for assessing hazards and risks. *Pharmacology and Therapeutics* **120,** 35–42 (2008).

24. Neouze, M.-A. Nanoparticle assemblies: main synthesis pathways and brief overview on some important applications. *J. Mater. Sci.* **48,** 7321–7349 (2013).

25. Pitkethly, M. J. Nanomaterials – the driving force. *Mater. Today* **7,** 20–29 (2004).

26. Haley, B. & Frenkel, E. Nanoparticles for drug delivery in cancer treatment. *Urol. Oncol.* **26,** 57–64 (2008).

27. Cho, E. C., Glaus, C., Chen, J., Welch, M. J. & Xia, Y. Inorganic nanoparticle-based contrast agents for molecular imaging. *Trends Mol. Med.* **16,** 561–73 (2010).

28. Eustis, S. & el-Sayed, M. a. Why gold nanoparticles are more precious than pretty gold: noble metal surface plasmon resonance and its enhancement of the radiative and nonradiative properties of nanocrystals of different shapes. *Chem. Soc. Rev.* **35,** 209–17 (2006).

29. Jain, P., El-Sayed, I. & El-Sayed, M. Au nanoparticles target cancer. *Nano Today* **2,** 18–29 (2007).

30. Mie, G. Beitrzur Optik trMedien, speziell kolloidaler Metall"osungen. *Ann. Phys.* **330,** 377–445 (1908).

31. Jain, P. K., Huang, X., El-Sayed, I. H. & El-Sayed, M. a. Noble metals on the nanoscale: optical and photothermal properties and some applications in imaging, sensing, biology, and medicine. *Acc. Chem. Res.* **41,** 1578–86 (2008).

32. Liz-Marzán, L. M. Tailoring Surface Plasmons trought the Morphology and Assembly of Metal Nanoparticles. *Langmuir* 32–41 (2006).

33. Wang, H., Tam, F., Grady, N. K. & Halas, N. J. Cu nanoshells: effects of interband transitions on the nanoparticle plasmon resonance. *J. Phys. Chem. B* **109,** 18218–22 (2005).

34. Connor, E. E., Mwamuka, J., Gole, A., Murphy, C. J. & Wyatt, M. D. Gold nanoparticles are taken up by human cells but do not cause acute cytotoxicity. *Small* **1,** 325–327 (2005).

35. Jain, P. K., Lee, K. S., El-Sayed, I. H. & El-Sayed, M. a. Calculated absorption and scattering properties of gold nanoparticles of different size, shape, and composition: applications in biological imaging and biomedicine. *J. Phys. Chem. B* **110,** 7238–48 (2006).

36. Miller, M. M., Lazarides, A. A. & Carolina, N. Sensitivity of Metal Nanoparticle Surface Plasmon Resonance to the Dielectric Environment. *J. Phys. Chem.* **109,** 21556–21565 (2005).

37. Link, S. & El-sayed, M. A. Spectral Properties and Relaxation Dynamics of Surface Plasmon Electronic Oscillations in silver nanodots. *J. Phys. Chem.* **103,** 8410–8426 (1999).

38. Thakor, a S., Jokerst, J., Zavaleta, C., Massoud, T. F. & Gambhir, S. S. Gold nanoparticles: a revival in precious metal administration to patients. *Nano Lett.* **11,** 4029–36 (2011).

39. Pérez-Juste, J., Liz-Marzán, L. M., Carnie, S., Chan, D. Y. C. & Mulvaney, P. Electric-Field-Directed Growth of Gold Nanorods in Aqueous Surfactant Solutions. *Adv. Funct. Mater.* **14,** 571–579 (2004).

40. Skrabalak, S. E. *et al*. Gold Nanocages: Synthesis, Properties, and Applications. *Accouints Chem. Res.* **41,** 1587–1595 (2008).

41. Xia, X. & Xia, Y. Gold nanocages as multifunctional materials for nanomedicine. *Front. Phys.* **9,** 378–384 (2013).

42. Yuan, H. *et al*. Gold nanostars: surfactant-free synthesis, 3D modelling, and two-photon photoluminescence imaging. *Nanotechnology* **23,** 075102 (2012).

43. Barbosa, S. *et al*. Tuning size and sensing properties in colloidal gold nanostars. *Langmuir* **26,** 14943–50 (2010).

44. Weissleder, R. A clearer vision for in vivo imaging. *Nat*. *Biotechnol*. **19,** 316–317 (2001).

45. Iyer, A. K., Khaled, G., Fang, J. & Maeda, H. Exploiting the enhanced permeability and retention effect for tumor targeting. *Drug Discov*. *Today* **11,** 812–8 (2006).

46. Danhier, F., Feron, O. & Préat, V. To exploit the tumor microenvironment: Passive and active tumor targeting of nanocarriers for anti-cancer drug delivery. *J*. *Control*. *Release* **148,** 135–46 (2010).

47. Hirn, S. *et al*. Particle size-dependent and surface charge-dependent biodistribution of gold nanoparticles after intravenous administration. *Eur*. *J*. *Pharm*. *Biopharm*. **77,** 407–16 (2011).

48. Moghimi, S. M., Hunter, a C. & Andresen, T. L. Factors controlling nanoparticle pharmacokinetics: an integrated analysis and perspective. *Annu*. *Rev*. *Pharmacol*. *Toxicol*. **52,** 481–503 (2012).

49. Owens, D. E. & Peppas, N. a. Opsonization, biodistribution, and pharmacokinetics of polymeric nanoparticles. *Int*. *J*. *Pharm*. **307,** 93–102 (2006).

50. Cho, W.-S. *et al*. Size-dependent tissue kinetics of PEG-coated gold nanoparticles. *Toxicol*. *Appl*. *Pharmacol*. **245,** 116–23 (2010).

51. Decuzzi, P. *et al*. Size and shape effects in the biodistribution of intravascularly injected particles. *J*. *Control*. *Release* **141,** 320–7 (2010).

52. Arnida, Janát-Amsbury, M. M., Ray, a, Peterson, C. M. & Ghandehari, H. Geometry and surface characteristics of gold nanoparticles influence their biodistribution and uptake by macrophages. *Eur*. *J*. *Pharm*. *Biopharm*. **77,** 417–23 (2011).

53. He, C., Hu, Y., Yin, L., Tang, C. & Yin, C. Effects of particle size and surface charge on cellular uptake and biodistribution of polymeric nanoparticles. *Biomaterials* **31,** 3657–66 (2010).

54. Schleh, C. *et al*. Size and surface charge of gold nanoparticles determine absorption across intestinal barriers and accumulation in secondary target organs after oral administration. *Nanotoxicology* **6,** 36–46 (2012).

55. Bartneck, M. *et al*. Effects of nanoparticle surface-coupled peptides, functional endgroups, and charge on intracellular distribution and functionality of human primary reticuloendothelial cells. *Nanomedicine* **8,** 1282–92 (2012).

56. Akiyama, Y., Mori, T., Katayama, Y. & Niidome, T. The effects of PEG grafting level and injection dose on gold nanorod biodistribution in the tumor-bearing mice. *J*. *Control*. *Release* **139,** 81–4 (2009).

57. Kunjachan, S. *et al*. Passive versus active tumor targeting using RGD- and NGR-modified polymeric nanomedicines. *Nano Lett*. **14,** 972–81 (2014).

58. Nanocrystals, G. *et al*. A Reexamination of Active and Passive Tumor Targeting by Using Rod-Shaped. *ACS Nano* **4,** 5887–5896 (2010).

59. Kolkman, J. a. & Law, D. a. Nanobodies - From llamas to therapeutic proteins. *Drug Discov*. *Today Technol*. **7,** e139–e146 (2010).

60. Vanlandschoot, P. *et al*. Nanobodies®: New ammunition to battle viruses. *Antiviral Res*. **92,** 389–407 (2011).

61. Muyldermans, S. Nanobodies: Natural Single-Domain Antibodies. *Annu*. *Rev*. *Biochem*. **82,** 775–797 (2013).

62. Kimling, J. *et al*. Turkevich Method for Gold Nanoparticle Synthesis Revisited. *J*. *Phys*. *Chem*. **110,** 15700–15707 (2006).

63. Van Roosbroeck, R. *et al*. Synthetic Antiferromagnetic Nanoparticles as Potential Contrast Agents in MRI. *ACS Nano* (2014). doi:10.1021/nn406158h

64. Khoury, C. G. & Vo-Dinh, T. Gold Nanostars For Surface-Enhanced Raman Scattering: Synthesis, Characterization and Optimization. *J*. *Phys*. *Chem*. *C*. *Nanomater*. *Interfaces* **2008,** 18849–18859 (2008).

65. Van de Broek, B. *et al*. Shape-controlled synthesis of NIR absorbing branched gold nanoparticles and morphology stabilization with alkanethiols. *Nanotechnology* **22,** 015601 (2011).

66. Wang, Z. *et al*. One-step functionalized gold nanorods as intracellular probe with improved SERS performance and reduced cytotoxicity. *Biosens*. *Bioelectron*. **26,** 241–7 (2010).

67. Srisombat, L., Park, J., Zhang, S. & Lee, T. R. Preparation , Characterization , and Chemical Stability of Gold Nanoparticles Coated with Mono- , Bis- , and Tris-Chelating Alkanethiols. *Langmuir* 7750–7754 (2008).

68. Liu, R., Kay, B. K., Jiang, S. & Chen, S. Nanoparticle Delivery: Targeting and Nonspecific Binding. *MRS Bulletin* **34,** 432–440 (2009).

69. Mornet, S., Vasseur, S., Grasset, F. & Duguet, E. Magnetic nanoparticle design for medical diagnosis and therapy. *Journal of Materials Chemistry* **14,** 2161 (2004).

70. Xu, M. & Wang, L. V. Photoacoustic imaging in biomedicine. *Rev*. *Sci*. *Instrum*. **77,** 041101 (2006).

71. Wang, L. V. Multiscale photoacoustic microscopy and computed tomography. *Nat*. *Photonics* **3,** 503–509 (2010).

72. Li, C. & Wang, L. V. Photoacoustic tomography and sensing in biomedicine. *Phys*. *Med*. *Biol*. **54,** R59–97 (2009).

73. Manohar, S. *et al*. Initial results of in vivo non-invasive cancer imaging in the human breast using near-infrared photoacoustics. *Opt*. *Express* **15,** 12277–12285 (2007).

74. Yang, X., Stein, E. W., Ashkenazi, S. & Wang, L. V. Nanoparticles for photoacoustic imaging. *Wiley Interdiscip*. *Rev*. *Nanomedicine Nanobiotechnology* **1,** 360–368 (2009).

75. Hu, M. *et al*. Gold nanostructures: engineering their plasmonic properties for biomedical applications. *Chem*. *Soc*. *Rev*. **35,** 1084–94 (2006).

76. Jokerst, J. V, Cole, A. J., Van de Sompel, D. & Gambhir, S. S. Gold nanorods for ovarian cancer detection with photoacoustic imaging and resection guidance via Raman imaging in living mice. *ACS Nano* **6,** 10366–77 (2012).

77. Agarwal, a. *et al*. Targeted gold nanorod contrast agent for prostate cancer detection by photoacoustic imaging. *J*. *Appl*. *Phys*. **102,** 064701 (2007).

78. Li, P.-C. *et al*. In vivo photoacoustic molecular imaging with simultaneous multiple selective targeting using antibody-conjugated gold nanorods. *Opt*. *Express* **16,** 18605–15 (2008).

79. Joshi, P. P., Yoon, S. J., Hardin, W. G., Emelianov, S. & Sokolov, K. V. Conjugation of antibodies to gold nanorods through Fc portion: synthesis and molecular specific imaging. *Bioconjug*. *Chem*. **24,** 878–88 (2013).

80. Chen, Y.-S. *et al*. Enhanced thermal stability of silica-coated gold nanorods for photoacoustic imaging and image-guided therapy. *Opt*. *Express* **18,** 8867–78 (2010).

81. Chen, Y.-S. *et al*. Silica-coated gold nanorods as photoacoustic signal nanoamplifiers. *Nano Lett*. **11,** 348–54 (2011).

82. Bayer, C. L. *et al*. Multiplex photoacoustic molecular imaging using targeted silica-coated gold nanorods. *Biomed*. *Opt*. *Express* **2,** 1828–35 (2011).

83. Kim, S., Chen, Y.-S., Luke, G. P. & Emelianov, S. Y. In-vivo ultrasound and photoacoustic image- guided photothermal cancer therapy using silica-coated gold nanorods. *IEEE Trans. Ultrason. Ferroelectr. Freq. Control* **61,** 891–7 (2014).

84. Song, K. H., Kim, C., Cobley, C. M., Xia, Y. & Wang, L. V. Near-infrared gold nanocages as a new class of tracers for photoacoustic sentinel lymph node mapping on a rat model. *Nano Lett.* **9,** 183–8 (2009).

85. Kim, C. *et al*. In vivo photoacoustic mapping of lymphatic systems with plasmon-resonant nanostars. *J. Mater. Chem.* **21,** 2841–2844 (2011).

86. Schlücker, S. SERS microscopy: nanoparticle probes and biomedical applications. *Chemphyschem* **10,** 1344–54 (2009).

87. Sharma, B., Frontiera, R. R., Henry, A.-I., Ringe, E. & Van Duyne, R. P. SERS: Materials, applications, and the future. *Mater. Today* **15,** 16–25 (2012).

88. Kneipp, J., Kneipp, H. & Kneipp, K. SERS--a single-molecule and nanoscale tool for bioanalytics. *Chem. Soc. Rev.* **37,** 1052–60 (2008).

89. Joo, S.-W. Surface-enhanced Raman scattering of 4,4′-bipyridine on gold nanoparticle surfaces. *Vib. Spectrosc.* **34,** 269–272 (2004).

90. Kneipp, J., Kneipp, H., Wittig, B. & Kneipp, K. Novel optical nanosensors for probing and imaging live cells. *Nanomedicine* **6,** 214–26 (2010).

91. Lutz, B. R. *et al*. Spectral Analysis of Multiplex Raman Probe Signatures. *ACS Nano* **2,** 2306–2314 (2009).

92. Maltzahn, G. Von *et al*. SERS-Coded Gold Nanorods as a Multifunctional Platform for Densely Multiplexed Near-Infrared Imaging and Photothermal Heating. *Adv. Mater.* **21,** 3175–3180 (2010).

93. Schütz, M., Steinigeweg, D., Salehi, M., Kömpe, K. & Schlücker, S. Hydrophilically stabilized gold nanostars as SERS labels for tissue imaging of the tumor suppressor p63 by immuno-SERS microscopy. *Chem. Commun. (Camb).* **47,** 4216–8 (2011).

94. Liu, Y., Yuan, H., Fales, A. M. & Vo-Dinh, T. pH-sensing nanostar probe using surface-enhanced Raman scattering (SERS): theoretical and experimental studies. *J. Raman Spectrosc.* **44,** 980–986 (2013).

95. Qian, X. *et al*. In vivo tumor targeting and spectroscopic detection with surface-enhanced Raman nanoparticle tags. *Nat. Biotechnol.* **26,** 83–90 (2008).

96. Park, H. *et al*. SERS imaging of HER2-overexpressed MCF7 cells using antibody-conjugated gold nanorods. *Phys. Chem. Chem. Phys.* **11,** 7444–9 (2009).

97. Vokerst, J. V., Miao, Z., Zavalate, C., Cheng, Z. & Gambhir, S. S. Affibody-functionalized gold-silica nanoparticles for Raman Molecular Imaging of the Epidermal Growth Factor Receptor. *Small* **7,** 625–633 (2012).

98. Rodríguez-Lorenzo, L. *et al*. Intracellular mapping with SERS-encoded gold nanostars. *Integr*. *Biol*. *(Camb)*. **3,** 922–6 (2011).

99. Fales, A. M., Yuan, H. & Vo-Dinh, T. Silica-coated gold nanostars for combined surface-enhanced Raman scattering (SERS) detection and singlet-oxygen generation: a potential nanoplatform for theranostics. *Langmuir* **27,** 12186–90 (2011).

100. Liu, Y., Chang, Z., Yuan, H., Fales, A. M. & Vo-Dinh, T. Quintuple-modality (SERS-MRI-CT-TPL-PTT) plasmonic nanoprobe for theranostics. *Nanoscale* **5,** 12126–31 (2013).

101. Yuan, H. *et al*. Quantitative SERRS Multiplexing of Biocompatible Gold Nanostars for in vitro and ex vivo detection. *Anal*. *Chem*. **85,** 208–212 (2014).

102. Lee, N., Choi, S. H. & Hyeon, T. Nano-sized CT contrast agents. *Adv*. *Mater*. **25,** 2641–60 (2013).

103. Hainfeld, J. F. *et al*. Micro-CT enables microlocalisation and quantification of Her2-targeted gold nanoparticles within tumour regions. *Br*. *J*. *Radiol*. **84,** 526–33 (2011).

104. Hainfeld, J. F., Smilowitz, H. M., Connor, M. J. O., Avraham, F. & Slatkin, D. N. Gold Nanoparticle Imaging and Radiotherapy of Brain Tumors in Mice. *Nanomedicine* **8,** 1601–1609 (2013).

105. Von Maltzahn, G. *et al*. Computationally guided photothermal tumor therapy using long-circulating gold nanorod antennas. *Cancer Res*. **69,** 3892–900 (2009).

106. Luo, T. *et al*. Mesoporous silica-coated gold nanorods with embedded indocyanine green for dual mode X-ray CT and NIR fluorescence imaging. *Opt*. *Express* **19,** 17030–9 (2011).

107. Huang, G., Yang, S., Yuan, Y. & Xing, D. Combining x-ray and photoacoustics for in vivo tumor imaging with gold nanorods. *Appl*. *Phys*. *Lett*. **99,** 123701 (2011).

108. Au, J. T. *et al*. Gold nanoparticles provide bright long-lasting vascular contrast for CT imaging. *AJR*. *Am*. *J*. *Roentgenol*. **200,** 1347–51 (2013).

109. Thiesen, B. & Jordan, A. Clinical applications of magnetic nanoparticles for hyperthermia. *Int*. *J*. *Hyperthermia* **24,** 467–74 (2008).

110. Dewhirst, M. W., Viglianti, B. L., Lora-Michiels, M., Hanson, M. & Hoopes, P. J. Basic principles of thermal dosimetry and thermal thresholds for tissue damage from hyperthermia. *Int*. *J*. *Hyperthermia* **19,** 267–94 (2003).

111. Song, C. W. Effect of Local Hyperthermia on Blood Flow and Microenvironment : A Review Effect of Local Hyperthermiaon BloodFlow and Microenvironment : *Cancer Res*. **44,** 4721–4730 (1984).

112. Dickerson, E. B. *et al*. Gold nanorod assisted near-infrared plasmonic photothermal therapy (PPTT) of squamous cell carcinoma in mice. *Cancer Lett*. **269,** 57–66 (2008).

113. Mackey, M. a, Ali, M. R. K., Austin, L. a, Near, R. D. & El-Sayed, M. a. The most effective gold nanorod size for plasmonic photothermal therapy: theory and in vitro experiments. *J*. *Phys*. *Chem*. *B* **118,** 1319–26 (2014).

114. Study, Q., Effect, P., Gold, I., Targeted, N. & Cells, B. C. A Quantitative Study on the Photothermal Effect of Immuno Gold Nanocages Targeted to Breast Cancer. *ACS Nano* **2,** 1645–1652 (2008).

115. Chen, J. *et al*. Immuno gold nanocages with tailored optical properties for targeted photothermal destruction of cancer cells. *Nano Lett*. **7,** 1318–22 (2007).

116. Van de Broek, B. *et al*. Specific cell targeting with nanobody conjugated branched gold nanoparticles for photothermal therapy. *ACS Nano* **5,** 4319–28 (2011).

117. Yuan, H. *et al*. In vivo particle tracking and photothermal ablation using plasmon-resonant gold nanostars. *Nanomedicine* 1–9 (2012). doi:10.1016/j.nano.2012.02.005

118. Xiao, M. *et al*. Gold nanotags for combined multi-colored Raman spectroscopy and x-ray computed tomography. *Nanotechnology* **21,** 035101 (2010).

119. Zhang, Y., Qian, J., Wang, D., Wang, Y. & He, S. Multifunctional gold nanorods with ultrahigh stability and tunability for in vivo fluorescence imaging, SERS detection, and photodynamic therapy. *Angew*. *Chem*. *Int*. *Ed*. *Engl*. **52,** 1148–51 (2013).

120. Lu, W. *et al*. Effects of photoacoustic imaging and photothermal ablation therapy mediated by targeted hollow gold nanospheres in an orthotopic mouse xenograft model of glioma. *Cancer Res*. **71,** 6116–21 (2011).

121. Curry, T., Kopelman, R., Shilo, M. & Popovtzer, R. Multifunctional theranostic gold nanoparticles for targeted CT imaging and photothermal therapy. *Contrast Media Mol*. *Imaging* **9,** 53–61 (2014).

122. Narayanan, S. *et al*. Biocompatible magnetite/gold nanohybrid contrast agents via green chemistry for MRI and CT bioimaging. *ACS Appl*. *Mater*. *Interfaces* **4,** 251–60 (2012).

123. Huang, P. *et al*. Folic acid-conjugated silica-modified gold nanorods for X-ray/CT imaging-guided dual-mode radiation and photo-thermal therapy. *Biomaterials* **32,** 9796–809 (2011).

124. Kircher, M. F. *et al*. A brain tumor molecular imaging strategy using a new triple-modality MRI-photoacoustic-Raman nanoparticle. *Nat*. *Med*. **18,** 829–34 (2012).

125. Sheng, Y., De Liao, L., Thakor, N. V. & Tan, M. C. Nanoparticles for Molecular Imaging. *J*. *Biomed*. *Nanotechnol*. **10,** 2641–2676 (2014).

126. Hainfeld, J. F., Slatkin, D. N., Focella, T. M. & Smilowitz, H. M. Gold nanoparticles: a new X-ray contrast agent. *Br*. *J*. *Radiol*. **79,** 248–53 (2006).

127. Xiao, M. *et al*. Gold nanotags for combined multi-colored Raman spectroscopy and x-ray computed tomography. *Nanotechnology* **21,** 035101 (2010).

128. Reuveni, T., Motiei, M., Romman, Z., Popovtzer, A. & Popovtzer, R. Targeted gold nanoparticles enable molecular CT imaging of cancer: an in vivo study. *Int*. *J*. *Nanomedicine* **6,** 2859–64 (2011).

129. Maier-Hauff, K. *et al*. Efficacy and safety of intratumoral thermotherapy using magnetic iron-oxide nanoparticles combined with external beam radiotherapy on patients with recurrent glioblastoma multiforme. *J*. *Neurooncol*. **103,** 317–24 (2011).

130. Ernsting, M. J., Murakami, M., Roy, A. & Li, S.-D. Factors controlling the pharmacokinetics, biodistribution and intratumoral penetration of nanoparticles. *J*. *Control*. *Release* **172,** 782–94 (2013).

131. Nomura, T., Koreeda, N., Yamashita, F., Takakura, Y. & Hashida, M. Effect of particle size and charge on the disposition of lipid carriers after intratumoral injection in to tissue-isolated tumors. *Pharm*. *Res*. **15,** 128–132 (1998).

132. Hao, E., Bailey, R. C., Schatz, G. C., Hupp, J. T. & Li, S. Synthesis and Optical Properties of 'Branched' Gold Nanocrystals. *Nano Lett*. **4,** 327–330 (2004).

133. Lin, S.-Y., Tsai, Y.-T., Chen, C.-C., Lin, C.-M. & Chen, C. Two-Step Functionalization of Neutral and Positively Charged Thiols onto Citrate-Stabilized Au Nanoparticles. *J*. *Phys*. *Chem*. *B* **108,** 2134–2139 (2004).

134. Ketkar-Atre, A. *et al*. In vivo hepatocyte MR imaging using lactose functionalized magnetoliposomes. *Biomaterials* **35,** 1015–24 (2014).

135. Gijsbers, R. *et al*. LEDGF hybrids efficiently retarget lentiviral integration into heterochromatin. *Mol*. *Ther*. **18,** 552–60 (2010).

136. Ibrahimi, A. *et al*. Highly Efficient Multicistronic Lentiviral Vectors with peptide 2A sequencies. *Hum*. *Gene Ther*. **860,** 845–860 (2009).

137. Vande Velde, G., Kucharíková, S., Schrevens, S., Himmelreich, U. & Van Dijck, P. Towards non-invasive monitoring of pathogen-host interactions during Candida albicans

biofilm formation using in vivo bioluminescence. *Cell*. *Microbiol*. (2013). doi:10.1111/cmi.12184

138. Soenen, S. J. *et al*. MRI assessment of blood outgrowth endothelial cell homing using cationic magnetoliposomes. *Biomaterials* **32,** 4140–50 (2011).

139. Trekker, J. *et al*. Sensitive in vivo cell detection using size-optimized superparamagnetic nanoparticles. *Biomaterials* **35,** 1627–35 (2014).

140. Monopoli, M. P., Aberg, C., Salvati, A. & Dawson, K. A. Biomolecular coronas provide the biological identity of nanosized materials. *Nat*. *Nanotechnol*. **7,** 779–786 (2012).

141. Verma, A. & Stellacci, F. Effect of surface properties on nanoparticle-cell interactions. *Small* **6,** 12–21 (2010).

142. Nel, A. E. *et al*. Understanding biophysicochemical interactions at the nano-bio interface. *Nat*. *Mater*. **8,** 543–57 (2009).

143. Huang, X., El-Sayed, I. H., Qian, W. & El-Sayed, M. a. Cancer cell imaging and photothermal therapy in the near-infrared region by using gold nanorods. *J*. *Am*. *Chem*. *Soc*. **128,** 2115–20 (2006).

144. Huang, X., Jain, P. K., El-Sayed, I. H. & El-Sayed, M. a. Plasmonic photothermal therapy (PPTT) using gold nanoparticles. *Lasers Med*. *Sci*. **23,** 217–28 (2008).

145. American National Standard for Safe Use of Lasers. (2007).

146. Cho, S. K. *et al*. Functionalized Gold Nanorods for Thermal Ablation Treatment of Bladder Cancer. *J*. *Biomed*. *Nanotechnol*. **10,** 1267–1276 (2014).

147. Albanese, A., Tang, P. S. & Chan, W. C. W. The effect of nanoparticle size, shape, and surface chemistry on biological systems. *Annu*. *Rev*. *Biomed*. *Eng*. **14,** 1–16 (2012).

148. Chithrani, D. B. Optimization of Bio-Nano Interface Using Gold Nanostructures as a Model Nanoparticle System. *Insciences J*. **1,** 115–135 (2011).

149. Chithrani, B. D., Ghazani, A. a & Chan, W. C. W. Determining the size and shape dependence of gold nanoparticle uptake into mammalian cells. *Nano Lett*. **6,** 662–8 (2006).

150. Villanueva, A. *et al*. The influence of surface functionalization on the enhanced internalization of magnetic nanoparticles in cancer cells. *Nanotechnology* **20,** 115103 (2009).

151. Chithrani, B. D. & Chan, W. C. W. Elucidating the mechanism of cellular uptake and removal of protein-coated gold nanoparticles of different sizes and shapes. *Nano Lett*. **7,** 1542–50 (2007).

152. Walkey, C. D. & Chan, W. C. W. Understanding and controlling the interaction of nanomaterials with proteins in a physiological environment. *Chem*. *Soc*. *Rev*. **41,** 2780–99 (2012).

153. Prabhakar, U. *et al*. Challenges and key considerations of the enhanced permeability and retention effect for nanomedicine drug delivery in oncology. *Cancer Res*. **73,** 2412–7 (2013).

154. Zhang, G. *et al*. Influence of anchoring ligands and particle size on the colloidal stability and in vivo biodistribution of polyethylene glycol-coated gold nanoparticles in tumor-xenografted mice. *Biomaterials* **30,** 1928–36 (2009).

155. Cabral, H. *et al*. Accumulation of sub-100 nm polymeric micelles in poorly permeable tumours depends on size. *Nat*. *Nanotechnol*. **6,** 815–23 (2011).

156. Meng, H. *et al*. Use of Size and a Co-polymer Design Feature to Improve the Biodistribution and the Enhanced Permeability and Retention Effect of Doxorubicin-loaded Mesoporous Silica Nanoparticles in a Murine Xenograft Tumor Model. *ACS Nano* **5,** 4131–4144 (2014).

157. Ho, E. A. *et al*. Characterization of Cationic Liposome Formulations Designed to Exhibit Extended Plasma Residence Times and Tumor Vasculature Targeting Properties. *J*. *Pharm*. *siciences* **99,** 2839–2853 (2010).

158. O'Neal, D. P., Hirsch, L. R., Halas, N. J., Payne, J. D. & West, J. L. Photo-thermal tumor ablation in mice using near infrared-absorbing nanoparticles. *Cancer Lett*. **209,** 171–6 (2004).

159. Jans, H. *et al*. Increased stability of mercapto alkane functionalized Au nanoparticles towards DNA sensing. *Nanotechnology* **21,** 285608 (2010).

160. Salvati, A. *et al*. Transferrin-functionalized nanoparticles lose their targeting capabilities when a biomolecule corona adsorbs on the surface. *Nat*. *Nanotechnol*. **8,** 137–43 (2013).

161. Lesniak, A. *et al*. Effects of the presence or absence of a protein corona on silica nanoparticle uptake and impact on cells. *ACS Nano* **6,** 5845–57 (2012).

162. Lesniak, A. *et al*. Nanoparticle adhesion to the cell membrane and its effect on nanoparticle uptake efficiency. *J*. *Am*. *Chem*. *Soc*. **135,** 1438–44 (2013).

163. Walkey, C. D. *et al*. Protein Corona Fingerprinting Predicts the Cellular Interaction of Gold and Silver Nanoparticles. *ACS Nano* 2439–2455 (2014).

164. Jans, K. *et al*. Chemical and biological characterization of thiol SAMs for neuronal cell attachment. *Langmuir* **25,** 4564–70 (2009).

165. Huang, S. *et al*. Contributions of Stromal Metalloproteinase-9 to Angiogenesis and Growth of Human Ovarian Carcinoma in Mice. *J*. *Natl*. *Cancer Inst*. **94,** 1134–1142 (2002).

166. Walkey, C. D., Olsen, J. B., Guo, H., Emili, A. & Chan, C. W. Nanoparticle Size and Surface Chemistry Determine Serum Protein Adsoprtion and Macrophage uptake. *J*. *Am*. *Chem*. *Soc*. 2139–2147 (2011).

167. Jokerst, J. V, Lobovkina, T., Zare, R. N. & Gambhir, S. J. Nanoparticle PEGylation for imaging and therapy. *Nanomedicine* **6,** 715–728 (2012).

168. Cho, W.-S. *et al*. Acute toxicity and pharmacokinetics of 13 nm-sized PEG-coated gold nanoparticles. *Toxicol*. *Appl*. *Pharmacol*. **236,** 16–24 (2009).

169. Nazir, S., Hussain, T., Ayub, A., Rashid, U. & Macrobert, A. J. Nanomaterials in combating cancer: Therapeutic applications and developments. *Nanomedicine* **10,** 19–34 (2013).

170. Bazak, R., Houri, M., El Achy, S., Kamel, S. & Refaat, T. Cancer active targeting by nanoparticles: a comprehensive review of literature. *J*. *Cancer Res*. *Clin*. *Oncol*. (2014). doi:10.1007/s00432-014-1767-3

171. Bertrand, N., Wu, J., Xu, X., Kamaly, N. & Farokhzad, O. C. Cancer nanotechnology: the impact of passive and active targeting in the era of modern cancer biology. *Adv*. *Drug Deliv*. *Rev*. **66,** 2–25 (2014).

172. Petros, R. a & DeSimone, J. M. Strategies in the design of nanoparticles for therapeutic applications. *Nat*. *Rev*. *Drug Discov*. **9,** 615–27 (2010).

173. Nie, S. Understanding and overcoming major barriers in cancer nanomedicine. *Nanomedicine* **5,** 523–528 (2010).

174. Monopoli, M. P. *et al*. Physical - Chemical Aspects of Protein Corona : Relevance to in Vitro and in Vivo Biological Impacts of Nanoparticles. *J*. *Am*. *Chem*. *Soc*. **133,** 2525–2534 (2011).

175. Treuel, L. *et al*. Impact of Protein Modi fi cation on the Protein Corona on Nanoparticles and Nanoparticle - Cell Interactions. *ACS Nano* (2013).

176. Wang, F. *et al*. The biomolecular corona is retained during nanoparticle uptake and protects the cells from the damage induced by cationic nanoparticles until degraded in the lysosomes. *Nanomedicine* **9,** 1159–68 (2013).

177. Mirshafiee, V., Mahmoudi, M., Lou, K., Cheng, J. & Kraft, M. L. Protein corona significantly reduces active targeting yield. *Chem*. *Commun*. *(Camb)*. **49,** 2557–9 (2013).

178. Dell'Orco, D., Lundqvist, M., Oslakovic, C., Cedervall, T. & Linse, S. Modeling the time evolution of the nanoparticle-protein corona in a body fluid. *PLoS One* **5,** e10949 (2010).

179. Arvizo, R. R. *et al*. Identifying new therapeutic targets via modulation of protein corona formation by engineered nanoparticles. *PLoS One* **7,** e33650 (2012).

180. Lilia, A. *et al*. Time Evolution of Nanoparticle − Protein Corona in Human Plasma: Relevance for Targeted Drug Delivery. *Langmuir* 6485–6494 (2013).

181. Vaneycken, I. *et al*. Preclinical screening of anti-HER2 nanobodies for molecular imaging of breast cancer. *FASEB J*. **25,** 2433–46 (2011).

182. Massa, S. *et al*. Site-Speci fi c Labeling of Cysteine-Tagged Camelid Single-Domain Antibody-Fragments for Use in Molecular Imaging. *Bioconjug*. *Chem*. (2014).

183. Li, W. *et al*. In vivo quantitative photoacoustic microscopy of gold nanostar kinetics in mouse organs. *Biomed*. *Opt*. *Express* **5,** 2679–85 (2014).

184. Walkey, C. D. & Chan, W. C. W. Unterstanding and controlling the interaction of nanomaterials with proteins in a physiological environment. *Chem*. *Soc*. *Rev*. **41,** 2780–2799 (2014).

185. Iversen, T.-G., Skotland, T. & Sandvig, K. Endocytosis and intracellular transport of nanoparticles: Present knowledge and need for future studies. *Nano Today* **6,** 176–185 (2011).

186. Frederix, F. *et al*. Reduced nonspecific adsorption on covalently immobilized protein surfaces using poly(ethylene oxide) containing blocking agents. *J*. *Biochem*. *Biophys*. *Methods* **58,** 67–74 (2004).

187. Mahmoudi, M. *et al*. Protein À Nanoparticle Interactions : Opportunities and Challenges. *Chem*. *Rev*. **111,** 5610–5637 (2011).

188. Walkey, C. D., Olsen, J. B., Guo, H., Emili, A. & Chan, W. C. W. Nanoparticle size and surface chemistry determine serum protein adsorption and macrophage uptake. *J*. *Am*. *Chem*. *Soc*. **134,** 2139–47 (2012).

189. Walczyk, D., Bombelli, F. B., Monopoli, M. P., Lynch, I. & Dawson, K. A. What the Cell ' Sees ' in Bionanoscience. *J*. *Am*. *Chem*. *Soc*. **132,** 5761–5768 (2010).

190. Ruoslahti, E., Bhatia, S. N. & Sailor, M. J. Targeting of drugs and nanoparticles to tumors. *J*. *Cell Biol*. **188,** 759–68 (2010).

191. Manshian, B. B. *et al*. High-Content Imaging and Gene Expression Approaches To Unravel the Effect of Surface Functionality on Cellular Interactions of Silver Nanoparticles. *ACS Nano* **9,** 10431–44 (2015).

192. Manshian, B. B. *et al*. High-content imaging and gene expression analysis to study cell-nanomaterial interactions: the effect of surface hydrophobicity. *Biomaterials* **35,** 9941–50 (2014).

193. Kneipp, J., Kneipp, H., Rajadurai, A., Redmond, R. W. & Kneipp, K. Optical probing and imaging of live cells using SERS labels. *J*. *Raman Spectrosc*. **40,** 1–5 (2009).

194. Kneipp, J., Kneipp, H., McLaughlin, M., Brown, D. & Kneipp, K. In vivo molecular probing of cellular compartments with gold nanoparticles and nanoaggregates. *Nano Lett*. **6,** 2225–31 (2006).

195. Maiti, K. K. *et al*. Multiplex targeted in vivo cancer detection using sensitive near-infrared SERS nanotags. *Nano Today* **7,** 85–93 (2012).

196. Mcqueenie, R. *et al*. Detection of In fl ammation in Vivo by Surface-Enhanced Raman Scattering Provides Higher Sensitivity Than Conventional Fluorescence Imaging. *Anal*. *Bioanal*. *Chem*. **84,** 5968–5975 (2012).

197. Drescher, D., Büchner, T., McNaughton, D. & Kneipp, J. SERS reveals the specific interaction of silver and gold nanoparticles with hemoglobin and red blood cell components. *Phys*. *Chem*. *Chem*. *Phys*. **15,** 5364–73 (2013).

198. Maiti, K. K. *et al*. Development of biocompatible SERS nanotag with increased stability by chemisorption of reporter molecule for in vivo cancer detection. *Biosens*. *Bioelectron*. **26,** 398–403 (2010).

199. Dinish, U. S., Balasundaram, G., Chang, Y.-T. & Olivo, M. Actively targeted in vivo multiplex detection of intrinsic cancer biomarkers using biocompatible SERS nanotags. *Sci*. *Rep*. **4,** 4075 (2014).

200. Conde, J., Bao, C., Cui, D., Baptista, P. V & Tian, F. Antibody-drug gold nanoantennas with Raman spectroscopic fingerprints for in vivo tumour theranostics. *J*. *Control*. *Release* **183,** 87–93 (2014).

201. Hao, F., Nehl, C. L., Hafner, J. H. & Nordlander, P. Plasmon resonances of a gold nanostar. *Nano Lett*. **7,** 729–32 (2007).

202. Hrelescu, C., Sau, T. K., Rogach, A. L., Jäckel, F. & Feldmann, J. Single gold nanostars enhance Raman scattering. *Appl*. *Phys*. *Lett*. **94,** 153113 (2009).

203. Das, G. *et al*. Plasmonic nanostars for SERS application. *Microelectron*. *Eng*. **111,** 247–250 (2013).

204. Guven, B., Basaran-Akgul, N., Temur, E., Tamer, U. & Boyaci, I. H. SERS-based sandwich immunoassay using antibody coated magnetic nanoparticles for Escherichia coli enumeration. *Analyst* **136,** 740–8 (2011).

205. Gellner, M., Kömpe, K. & Schlücker, S. Multiplexing with SERS labels using mixed SAMs of Raman reporter molecules. *Anal*. *Bioanal*. *Chem*. **394,** 1839–44 (2009).

206. Etchegoin, P. G. Quo vadis surface-enhanced Raman scattering? *Phys*. *Chem*. *Chem*. *Phys*. **11,** 7348–9 (2009).

207. Zhao, B. *et al*. Gold nanostructures encoded by non-fluorescent small molecules in polyA-mediated nanogaps as universal SERS nanotags for recognizing various bioactive molecules. *Chem*. *Sci*. **5,** 4460–4466 (2014).

208. Braun, G. B. *et al*. Generalized Approach to SERS-Active Nanomaterials via Controlled Nanoparticle Linking, Polymer Encapsulation, and Small-Molecule Infusion. *J*. *Phys*. *Chem*. *C* **113,** 13622–13629 (2009).

209. Barbosa, S. *et al*. Tuning size and sensing properties in colloidal gold nanostars. *Langmuir* **26,** 14943–50 (2010).

210. Hrelescu, C., Sau, T. K., Rogach, A. L., Jäckel, F. & Feldmann, J. Single gold nanostars enhance Raman scattering. *Appl*. *Phys*. *Lett*. **94,** 153113 (2009).

211. Lim, D.-K. *et al*. Highly uniform and reproducible surface-enhanced Raman scattering from DNA-tailorable nanoparticles with 1-nm interior gap. *Nat*. *Nanotechnol*. **6,** 452–60 (2011).

212. Chen, Z. *et al*. Tunable SERS-Tags-Hidden Gold Nanorattles for Theranosis of Cancer Cells with Single Laser Beam. *Sci*. *Rep*. **4,** 6709 (2014).

213. Yang, M. *et al*. SERS-active gold lace nanoshells with built-in hotspots. *Nano Lett*. **10,** 4013–9 (2010).

214. Lu, W. *et al*. Gold nano-popcorn-based targeted diagnosis, nanotherapy treatment, and in situ monitoring of photothermal therapy response of prostate cancer cells using surface-enhanced Raman spectroscopy. *J*. *Am*. *Chem*. *Soc*. **132,** 18103–14 (2010).

215. Lynch, I. *et al*. The nanoparticle-protein complex as a biological entity; a complex fluids and surface science challenge for the 21st century. *Adv*. *Colloid Interface Sci*. **134-135,** 167–74 (2007).

216. Carmeliet, P. & Jain, R. K. Principles and mechanisms of vessel normalization for cancer and other angiogenic diseases. *Nat*. *Rev*. *Drug Discov*. **10,** 417–427 (2011).

217. Jain, R. K. & Stylianopoulos, T. Delivering nanomedicine to solid tumors. *Nat*. *Rev*. *Clin*. *Oncol*. **7,** 653–64 (2010).

218. Balasubramanian, S. K. *et al*. Biodistribution of gold nanoparticles and gene expression changes in the liver and spleen after intravenous administration in rats. *Biomaterials* **31,** 2034–2042 (2010).

Scientific Contributions

Publications

1. Van de Broek B, Devoogdt N, **D'Hollander A**, Gijs H-L, Jans K, Lagae L, et al. Specific cell targeting with nanobody conjugated branched gold nanoparticles for photothermal therapy. ACS Nano. 2011 Jun 28;5(6):4319–28.

2. Van Roosbroeck R, Van Roy W, Stakenborg T, Trekker J, **D'Hollander A**, Dresselaers T, et al. Synthetic Antiferromagnetic Nanoparticles as Potential Contrast Agents in MRI. ACS Nano. 2014 Feb 1; 8 (3): 2267-2278.

3. **D'Hollander A**, Vande Velde G, Jans H, Vanspauwen B, Jose J, Fuchs D, Struys T, Stakenborg T, Lagae L, Himmelreich U. Assessment of the theranostic potential of gold nanostars - a multimodal imaging and photothermal treatment study. Jounral Biomedical Nanontechnology ***(Revisions)***

4. **D'Hollander A**., Mathieu E., Jans H., Vande Velde G., Stakenborg T. Van Dorpe P., Himmelreich U., Lagae. L. Development of nanostars as a biocompatible tumor contrast agent for in vivo SERS imaging. International Journal of nanomedicine 2016 Aug;4(11):3703-14

5. **D'Hollander A***, Van Roosbroeck R*, Trekker J, Stakenborg T, Dresselaer T, Vande Velde G, Struys T, Lambrichts I, Lammertyn J, Himmelreich U, Lagae L. Synthetic Antiferromagnetic Gold Nanoparticles As Bimodal Contrast Agents in MRI and CT – An Experimental In Vitro and In Vivo Study. Advanced Healthcare Materials **(In submission)**

6. **D'Hollander A** , Verstraete C, Massa S, Vermeersch E., Jans H., Vande Velde G., Stakenborg T.,Devoogdt N, Muyldermans S[5,6], Lagae L,Himmelreich U. Limiting the protein corona: A successful strategy for in vivo active targeting of anti-HER2 nanobody-functionalized nanostars.(under preparation)

Participation at international meetings

Specific Biological Targeting Using Branched Gold Nanoparticles for Tumor Targeting Therapy. European Science Foundation Summer School Nanomedicine 2011, Lutherstadt Wittenberg, Germany (poster)

Specific Biological Targeting Using Branched Gold Nanoparticles For Hyperthermia tumor therapy. Imec PhD Meeting 2011, Leuven, Belgium (poster)

Branched gold nanoparticles for a combined photoacoustic imaging and photothermal therapy. Biomedical Optics 2012, Miami, USA (Presentation)

A combined photoacoustic imaging and photothermal therapy using branched gold nanoparticles. World Molecular Imaging 2012, Dublin, Ireland

Nanostars for a dual Computed Tomography/ Photoacoustic Imaging and Photothermal Theray. Imec PhD Days 2012, Leuven, Belgium (Presentation)

Using Gold nanostars for Optical Imaging of Cancer Using Surface Enhanced Raman Spectroscopy. European Molecular Imaging Conference 2013, Turin, Italy (Poster)

Using Gold nanostars for Optical Imaging of Cancer Using Surface Enhanced Raman Spectroscopy. World Molecular Imaging Conference, Savannah, USA (Poster)

Gold nanostars as a specific theranostic agent for multimodal imaging and photothermal treatment of cancer. European Molecular Imaging Conference 2014 , Antwerp, Belgium (Poster: **Poster award**)

In vitro and in vivo study of gold synthetic antiferromagnetic nanoparticles as bimodal contrast agents in MRI and CT. European Molecular Imaging Conference 2014 , Antwerp, Belgium (Poster: **Poster award**)

Gold nanostar as an in vivo diagnostic agent of cancer using SERS imaging. International Conference on Raman Spectroscopy 2014, Ulm, Germany (Presentation)

Gold nanostars as a specific theranostic agent for multimodal imaging and photothermal treatment of HER2 positive cancer. World Molecular Imaging Conference 2014, Seoul, South-Korea (Presentation)

In vitro and *in vivo* study of gold synthetic antiferromagnetic nanoparticles as bimodal contrast agents in MRI and CT. World Molecular Imaging Conference 2014, Seoul, South-Korea (Poster)